# Electrostatic Discharge and Roughness Modelling in Diamond Turning of Contact Lenses

*Prepared by*

FUNDISWA KOPI

20530186

Submitted in fulfilment of the requirements towards:

Master of Engineering: Mechatronics

At the Nelson Mandela Metropolitan University.

April, 2017

*Supervisor:* Prof Khaled Abou-El-Hossein

# DECLARATION

I, Kopi Fundiswa, hereby declare that:

- The work done in this thesis is my own;
- All sources used or referred to have been documented and recognised; and
- The thesis has not been previously submitted in full or partial fulfilment of the requirements for an equivalent or higher qualification at any other educational institution.

Author's signature:                    Date: 03 April 2017

# DEDICATION

To all the young girls that have a dream to pursue, I say follow your dreams, the sky is the limit.

# ACKNOWLEDGMENTS

# ABSTRACT

With the increased application of ultra-high precision machining of polymers and the limited research in single point diamond turning (SPDT) of contact lens polymers, it became imperative to gather understanding on the production of contact lenses using the above-mentioned technology. A limiting factor in SPDT of polymers is wear of the diamond tool, resulting into poor surface finish due to unintended charges generated as a result of the contact/rubbing action between the cutting tool and the cut material.

Central Composite Design (CCD) Face Centred experimental design was developed and applied to the SPDT of ONSI-56 and Polymethly methacrylate (PMMA) contact lens buttons. An electrostatic sensor coupled to a computer monitored the electrostatic discharge generated and a profilometer measured the surface roughness. The Response Surface Method (RSM) was utilised during the development of predictive models for both the surface roughness and the electrostatic discharge generated, to deduce the effects of cutting parameters during machining.

The cutting speed and the feed rate deemed as the influential parameters on the surface roughness and electrostatic discharge, for both materials. The depth of cut induced more charge generation for PMMA. Predictive models were successfully developed and they were aimed at creating a database a guide to the SPDT of contact lens polymers.

# LIST OF ABBREVIATIONS

| | |
|---|---|
| SPDT | Single Point Diamond Turning |
| PMMA | Poly methyl methacrylate |
| MMA | Methyl methacrylate |
| RGP | Rigid Gas Permeable |
| CVD | Chemical Vapour Deposition |
| PCD | Polycrystalline Diamonds |
| CNC | Computer Numeric Control |
| PC | Poly Carbonate |
| ESP | Electrostatic Potential |
| ESD | Electrostatic Discharge |
| NI | National Instruments |
| CCD | Central Composite Design |

# TABLE OF CONTENTS

# LIST OF FIGURES

# LIST OF TABLES

# CHAPTER 1: INTRODUCTION

This chapter will give the background of the study and present the aim and objectives of it.

## 1.1 Background and Significance

Ultra-high precision machining is an extensively used precision manufacturing process that boasts on its production of micrometre (μm) and nanometre (nm) surface roughness's (Hocheng and Hsieh (2004)). It can create complex geometries with fine surface qualities that require no post-polishing (Li et al. (2015)). The highly sophisticated manufacturing technique is used in the optics (Li and Zhang (2016)), electronics (Davies et al. (2003)), aerospace (Ji et al. (2016)) and biomedical industries. Various materials can be machined using ultra-high precision machining; such materials include fibre reinforced, conductive and optical polymers, selected metals and a wide range of ceramics.

Researchers such as Chon and Namba (2010) and Namba et al. (2003) have utilised ultra-high precision machining, using single point diamond turning (SPDT) during their studies. Chon and Namba (2010) used SPDT to machine electroless nickel used for flat x-ray mirrors, platted on an aluminium alloy (A7075) and they were able to obtain a surface roughness of 0.95 nm, on a 360 μm x 270 μm machining area. Namba et al. (2003) obtained a surface roughness of less than 1 nm within a 4 x 4 mm$^2$ area, while machining thienylchakone organic nonlinear crystals. This shows the capability of utilising SPDT.

In the biomedical industry, SPDT has become popular in the production of contact lenses and intraocular lenses. The lenses are used for a variety of visual

impairments, visual correction, cosmetic and therapeutic reasons, and their increased use has created a demand, increasing their manufacturing (Olufayo et al. (2014)). The increase in the demand has created a pressure in the manufacturing technique to increase the volume of production to meet the customer needs. Customer requirements include fitment, comfortability, and minimum susceptibility to bacterial adhesion and infections. Since SPDT requires no post-polishing, provides minimum manufacturing time and it can produce a product suited to customer needs that has created the popularity in utilising it during polymer machining (Hocheng and Hsieh (2004)).

However, even though SPDT is advantageous, it suffers greatly due to the high costs involved in replacing a damaged cutting tool (Gubbels (2006)). One would assume that because a diamond tool is stronger than a polymer, then no failure could result during machining. On the contrary, it has been shown that adhesion, abrasion, contact electrification, chemical wear, micro-fractures, can develop when the diamond tool is cutting a polymer material (Gubbels et al. (2004), Chao et al. (2008), Thornton and Wilks (1980), Mohammadi et al. (2014), Singh et al. (2013), Tanaka et al. (2005)). The cutting tool wear that is common in the manufacturing of contact lenses is triboelectric wear due to electric discharge caused by the removal action between the diamond tool and the polymer (Gubbels (2006)).

When two dissimilar solid surfaces come in contact with each other and are separated (with or without intentional rubbing, friction or rolling) charge transfers from one surface to the other (Liu et al. (2013a), Liu et al. (2013b), Wiles et al. (2003)). When the materials separate, more electrons remain on one surface making it negatively charged, and the other surface positively charged. The surfaces that come into contact and separate become triboelectrically charged by contact electrification.

This phenomenon seems to also be taking place during single point diamond turning of contact lenses polymers and minimum research exists on the triboelectric charging and discharging (Olufayo and Abou-El-Hossein (2013), Olufayo et al. (2014)). Hence, there exists a need to investigate triboelectric charging and discharging and its inference on the surface finish during SPDT of contact lens polymers and how the whole phenomenon; together with the cutting parameters, influence the machining process.

## 1.2 Research Aim and Objectives

Aim:

The aim of this research is for the development and the analysis of an electrostatic discharge and a surface roughness model. The models will assist in studying the influence of cutting parameters on the electrostatic discharge generated and the surface roughness obtained during SPDT of contact lens polymers.

Objectives:

- To use SPDT to machine two different contact lens materials (hydrophobic and hydrophilic based)

- To use an electrostatic sensor to capture the electrostatic discharge acquired during machining.

- To measure the surface roughness obtained using a profilometer.

- To develop an electrostatic discharge model for the hydrophobic and hydrophilic based materials.

- To develop a surface roughness model for both materials.

- To analyse the developed models between the different materials.

- To determine if the developed models could be used to predict the ideal cutting parameters that would generate optical surface quality

## 1.3 Structure of the Thesis

The structure of the research is illustrated in Figure 1. Five chapters shall present the thesis.

Chapter 1 will introduce the background and study significance. It will also address the aim and objectives of the study.

Chapter 2 will critically review literature for polymers in general and in medicine. It will address the fabrication methods for contact lens polymers. It will also look at SPDT, surface roughness and the contact electrification phenomenon.

Chapter 3 will outline the experimental setup and the process followed to conduct the experiments. It will also explain the machine information, the workpieces' characteristics, the cutting tool and the design method utilised.

Chapter 4 will analyse and discuss the results obtained during the experiments conducted. Show the developed models and compare the results between the hydrophobic and hydrophilic-based materials.

Chapter 5 will conclude the study and provide recommendations for future work.
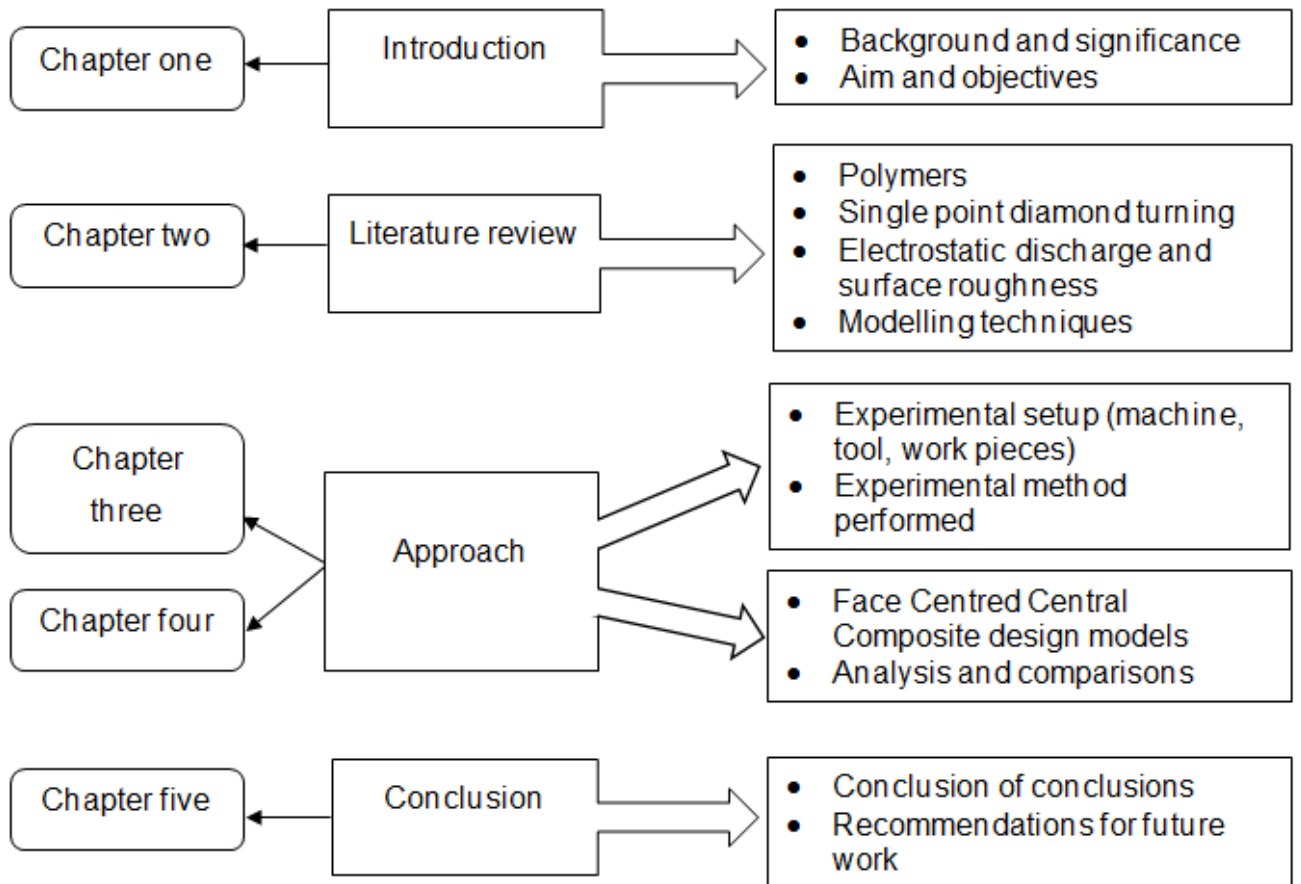
**Figure 1: Thesis overall outline.**

## 1.4 Conclusion

The research structure is outlined, with the aims and objectives clearly defined. Chapter 2 will review contact lens materials, surface roughness, electrostatic discharge measurements and tool wear.

# CHAPTER 2: LITERATURE REVIEW

This section will discuss the literature surrounding polymers in general and in medicine, ultra-high precision machining using a diamond tool, surface roughness and methods of measurement, electrostatic charge and discharge and cutting tool wear.

## 2.1 Polymers

Polymers form part of an important role in human life, such that life without them would seem very difficult. Polymers are all around us in everyday use namely rubber, plastic, in resins and adhesive tapes. Even our bodies are made up of polymers like protein and enzymes (Kailas (2013)), Wikipedia (2016)). The word polymer originated from the Greek words 'polus' which means many, and 'meros' which means parts. Hence, a polymer is a large molecule or macromolecule, composed of many repeated parts.

A polymer can have different chemical structure, physical properties, mechanical behaviour, thermal characteristics and many other properties, classified in different ways. One of the basic properties of a polymer is the identity of its basic monomers (repeat unit). Polymers that contain one type of a monomer namely homo-polymers and those that contain a mixture of monomers known as copolymers. Another property is the configuration of the polymer, which is the molecular structure. Figures 2-7 below, display three different chain arrangements of the polymers, namely, linear, branched and cross-linked polymer chains, with either homo or copolymers (the X, Y demonstrate a type of monomer).

Linear polymers are composed of one long continuous chain without any additional attachments (straight line). They can be a homo-polymer or a copolymer (the same applies to branched and cross-linked polymer chains).

$$— X — X — X —$$
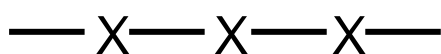
**Figure 2: Linear homo-polymer.**

$$— Y — X — Y —$$
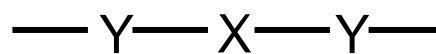
**Figure 3: Linear co-polymer.**

Branched polymers have a chain that consists of one main chain of molecules with small molecular chains branching from it.
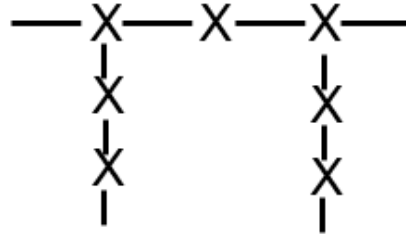


**Figure 4: Branched homo-polymer.**
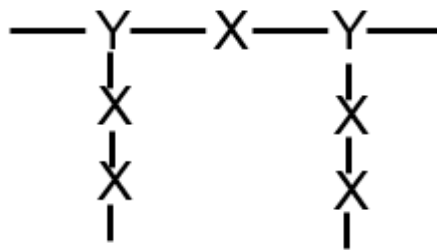


**Figure 5: Branched co-polymer.**

Cross-linked polymers occur due to the primary valence bonds forming between polymer chains.
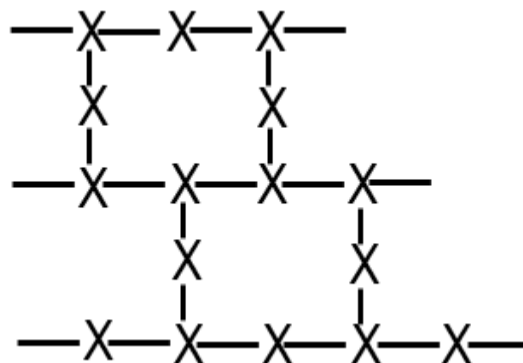


**Figure 6: Cross linked homo-polymer.**

$$
\begin{array}{ccccc}
-\text{X}-&\text{X}-&\text{X}- & & \\
\ \ |& &| & & \\
\ \ \text{X}& &\text{X} & & \\
\ \ |& &| & & \\
-\text{X}-&\text{Y}-&\text{X}-&\text{Y}- & \\
& & &| & \\
& & &\text{X} & \\
& & &| & \\
-\text{X}-&\text{Y}-&\text{X}-&\text{Y}- &
\end{array}
$$
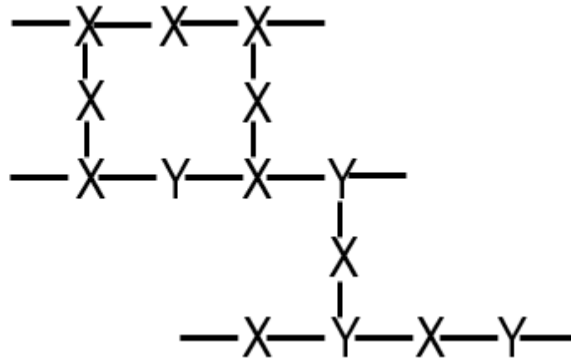
**Figure 7: Cross linked co-polymer.**

The arrangement of the molecules of polymer chains is another property of the polymer. The arrangements include amorphous and crystalline. In the amorphous arrangement, there is no specific order of the molecules because they tangled or randomly arranged. They appear to be clear and some of their applications include plastic wraps, headlight lenses and contact lenses. In the crystalline arrangement, there is a distinct straight like ordered arrangement. The polymer chains are translucent and opaque and example of a crystalline structure would be table salt or gem stone (American Chemistry Council (2015)).

Industrial polymers can be classified into plastics and elastomers. Plastics are either natural or synthetic and are processed by forming or moulding them into shapes (Kailas (2013)). They have a wide range of properties, which are unattainable in other materials. Some of their properties include being light- weight, having a wide range of colours, low thermal and electrical conductivity, good toughness and resistance. Classifying plastics according to their thermal behaviour further leads to thermoplastic and thermosetting polymers.

Thermoplastic polymers are polymers that can be softened repeatedly on the application of thermal energy, with minimum change in properties if treated with certain precaution. The process can be reversed to harden them by cooling. They are linear polymers without any crosslinking in the structure where long molecular chains are bonded to each other by secondary bonds and/or inter-wined (Kailas (2013)), examples include polyolefins and polyethers.

Thermosetting polymers are polymers that require heat to mould them into shape. They form into a permanent shape, and set by chemical reactions, such as extensive cross-linking. They cannot be re-melted or reformed into another shape but decompose upon being heated to high temperatures. They are generally stronger but more brittle than their former counter-part. Examples of them include epoxies, phenolics and amino resins (no name for author, Polymers).

Elastomers also known as rubbers and these polymers undergo large elongations under load, at room temperature, and return to their original shape after releasing the load. They are linear with occasional cross-links. An example of an elastomer would be natural rubber. Figure 8 below shows a summary of the classification of polymers.

| Polymers | | | |
|---|---|---|---|
| Synthetic | | | Natural |
| Thermoplastic | Thermoplastic | Elastomers | Cellulose |
| Linear chains | Cross-linking chains | Linear with additional cross-links | Proteins |
| Polyolefins, polyethers | Epoxies, phenolics, amino acids | Rubber | |
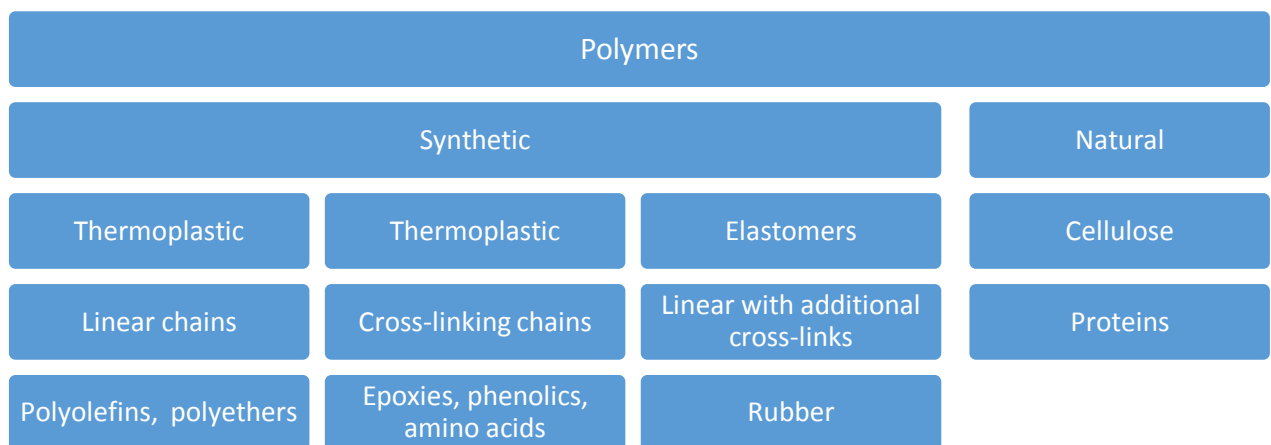
**Figure 8: Classification of polymers.**

## 2.1.1 Polymerisation of polymers

There are two main ways to form polymers, namely, addition polymerization and condensation polymerization. In addition, polymerisation, also known as chain reaction polymerisation, the process involves multi-function monomer units that are attached one at a time in a chain like manner to form liner or 3D macro-molecules. The structure of the macro-molecule is an exact multiple of the original reactant monomer. Addition polymerisation involves initiation, propagation and termination. Figure 9 shows an example of polymerization of ethylene monomer forming polyethylene.
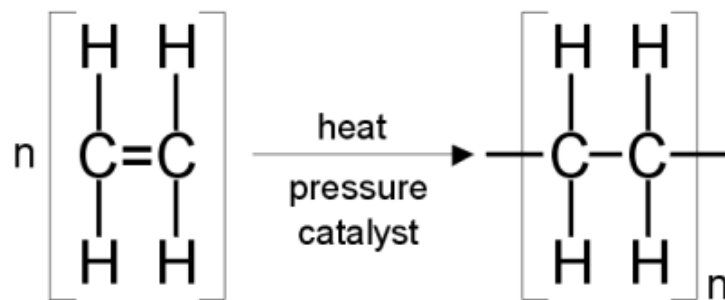
**Figure 9: Ethylene monomer forming Polyethylene.** [UNSW Australia (2013)]
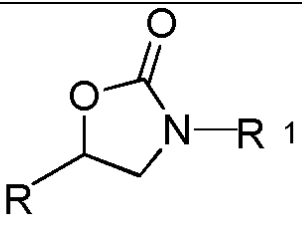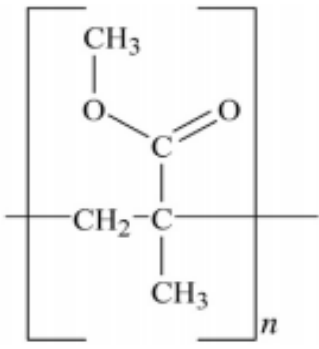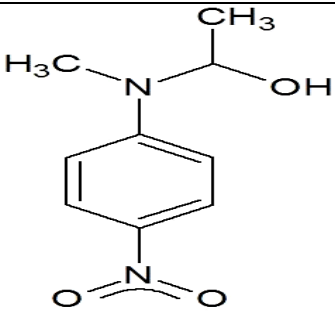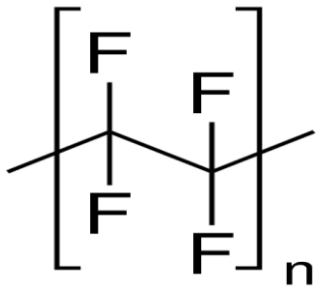
Condensation polymerisation, also known as step growth polymerisation, comprises of more than one monomer species. Usually there is a small molecular weight water by-product which is eliminated (Schmitz (2012)).
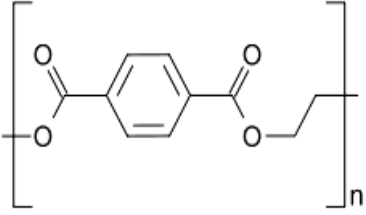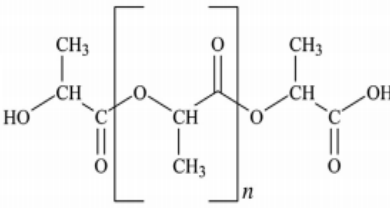
## 2.1.2 Polymers in medicine
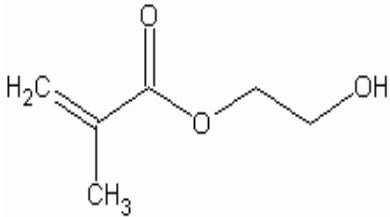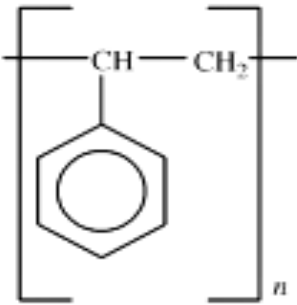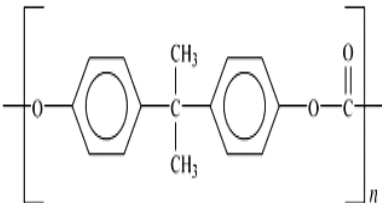
Polymers in biomedical applications date back to ancient history (L. Ambrosio (1998)). Different organic and inorganic materials were used by Romans, Egyptians and Chinese people thousands of years ago to solve difficult and chronic medical problems. That enabled polymers in biomedical application to be the fastest growing area in polymer science. The highly interdisciplinary field connects traditional sciences (chemistry and physics) with modern engineering sciences (chemical, mechanical and biomedical) to solve different human health problems (Heimke (1989)).
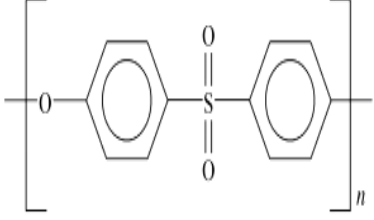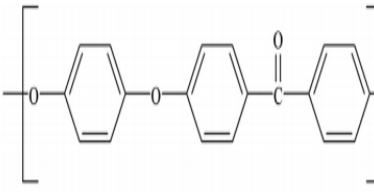
Biomedical use of polymers is extensive; Table 1 shows a list of polymers that are used for medical applications (Parakka et al. (2013), Wintermantel et al. (2013), Clemitson (2015), Sigma-Aldrich (2016), WS Hampshire Inc. (2016), McKeen (2013)).

**Table 1: Biomedical applications of polymers**

| Polymer name(s) | Structure | Properties | Medical Application (s) |
|---|---|---|---|
| Silicones (Si) |  | Thermal conductivity is low<br>Chemical reactivity is low<br>Toxicity is low | Ophthalmology Implants: nose, ear & breasts |
| Polymethyl methacrylate (PMMA)<br><br>Acrylic polymer, also known as Plexiglass®. |  | Optical clear and colourless<br>Extremely hard<br>Weather resistant | Lenses: contact, intraocular<br>Bone cements |
| Polyurethane Elastomers |  | High tear strength<br>Hardness and tensile strength increase when temperature decreases | Artificial hearts, pacemaker coatings, catheters |
| Polytetrafluoro ethylene (PTFE) |  | High strength and toughness<br>Self-lubricating at low temperatures<br>Good flexibility at moderate temperatures | Prostheses: Vascular, ligament, abdominal |

| | | | |
|---|---|---|---|
| Polyethylene (PE)<br><br>Can be made in a number of ways:<br>Ultra-low density polyethylene (ULDPE)<br>Very-low density polyethylene (VLDPE)<br>Linear-low density polyethylene (LLDPE)<br>Low density polyethylene (LDPE)<br>High density polyethylene (HDPE) |  | Corrosion resistance<br>Impact resistance<br>High tensile strength | Acetabular cups & catheters<br>Breather patches<br>Wear bearing surface of hip and knee arthroplasty and joint replacement |
| Poly glycolic acid & Poly (L-lactide) (PGA & PLLA)<br><br>They are required to serve for a |  | Biodegradable and compostable<br>Derived from renewable resources | Biodegradable systems for suture<br>Plates: Orthopaedic & maxillo-facial applications |

| | | | |
|---|---|---|---|
| certain period of time. | | | |
| Hydrogel (Acrylate)

The special acrylic polymer is made from monomers that have hydroxyl (-OH) groups that are attracted to water. |  | Can hold moisture on the surface
Dissolution resistance | Drug release systems
Soft contact lenses |
| Polystyrene

Simplest form of styrene. |  | Transparent or made into colour
Hard with limited flexibility
It is cheap and easy to use | Diagnostic instruments and laboratory disposable ware |
| Polycarbonate

Formed by the reaction of bis-phenol A and carbonic acid. |  | Impact resistant
Tough at low temperatures
Has glass clarity | Medical Apparatus (arterial cannula or high-pressure syringes) |

| Polyethersulfone<br><br>Is an amorphous polymer and a high temperature, engineering thermoplastic. |  | Thermal resistance<br>Excellent hydrolytic and sterilization resistance<br>Optical clarity | Medical equipment with repeated sterilisation and fluid handling fittings |
|---|---|---|---|
| Polyetherether ketone<br><br>Also known as polyarylketones and have spectacular mechanical properties. |  | Chemical and wear resistance<br>Hydrolysis resistance<br>Exceptional thermal properties | Catheters, Reusable medical components and dental syringes |

## 2.2 Contact lenses

The eye is one the sensory parts of the body that helps with visualisation of objects around us. In the eye, light enters through the cornea, which is the transparent layer in the front of the eye. This light then passes the iris and an opening known as a pupil, located directly behind the cornea. This light is refracted then, through aqueous and the iris, until it meets the natural lens. The lens then focuses the light onto the retina, which continues through the vitreous media. An image is then formed on the retinal photoreceptors at the back of the eye (Lace (2013)). The optic nerve carries the information to the brain allowing us to see objects around us. Figure 10 displays an image of the eye.
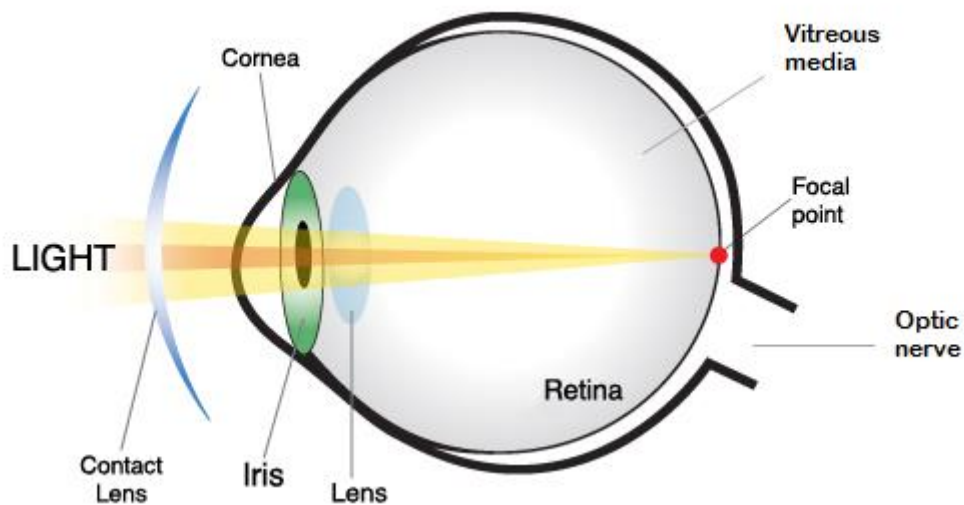
**Figure 10: Schematic of the anatomy of the eye.**

In as much as the natural lens is supposed to provide optical quality imagery to the brain, there can be some visual problems that could inhibit the proper functioning of the lens within the eye. Such eye impairments include farsightedness, near-sightedness, and astigmatism and Figure 11 below displays that.
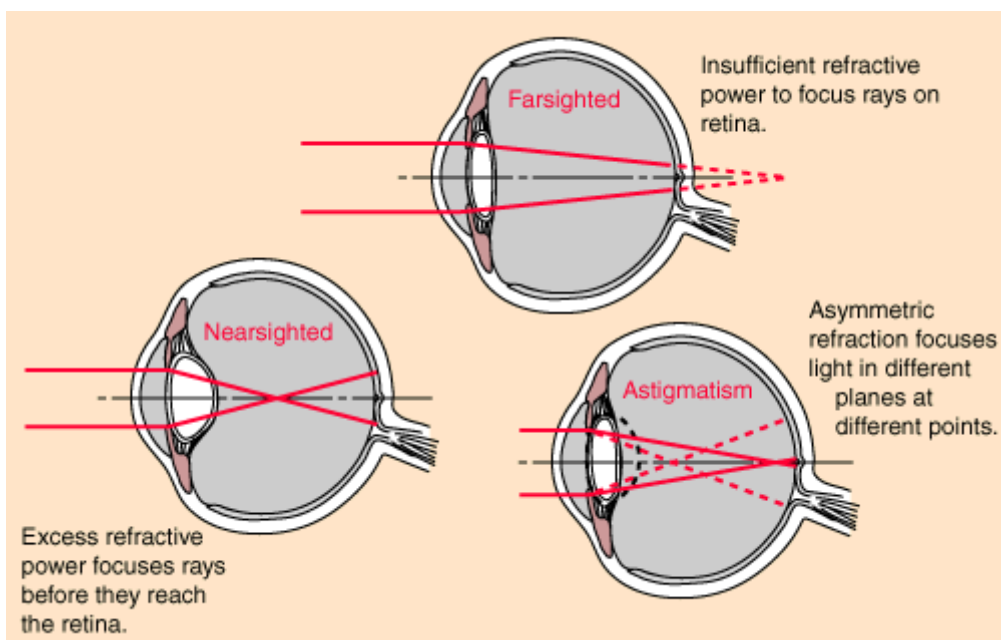


**Figure 11: Common visual impairments.** Nave (2006)

Spectacles, contact lenses or intraocular lenses are usually introduced to provide correction of the vision issues. The contact lens or the spectacles will provide the necessary power corrections to enable better visualisation of images or objects. In Figure 12, an illustration has been given, to show some of the lenses used to correct some common eye defects. It is therefore important to understand the different types of contact lenses and their different manufacturing processes.
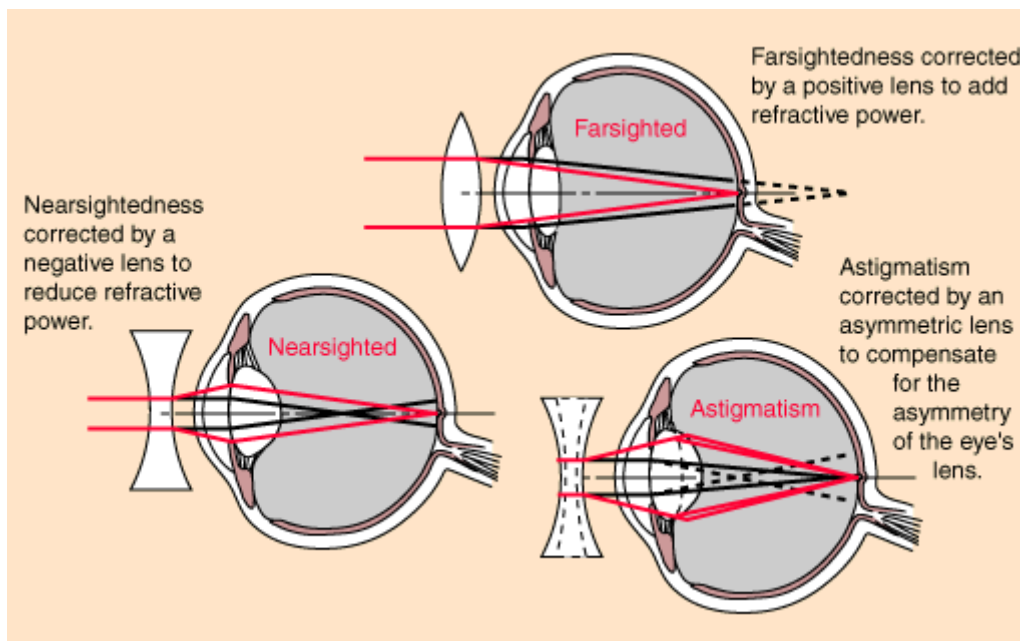


**Figure 12: Corrective lenses for visual problems.**[Nave (2006)]

## 2.2.1 History of Contact Lenses

A contact lens is a thin disk that floats on top of tears on top of the eye, see Figure 8, (Sánchez and Muñoz (2012)). It is one of the modern technological breakthroughs, which has been evolving and undergoing tremendous growth. Contact lenses have a rich history that stems from the early 1500's where Leonardo Da Vinci conceptualised and developed sketches that depicted several forms of contact lenses, (Block (1961), Levene (1967), Lace (2013) ,Goodlaw (2002), Schifrin and Rich (1984), Sánchez and Muñoz (2012)).

Leonardo Da Vinci initially included a demonstration that involved a water filled glass bowl in which a person placed his face and looked through the bottom of the bowl,

amounts of time. The second one utilised a water filled glass hemisphere that was worn over the eye like a contact lens. Theoretically, he was able to identify corneal neutralisation, that is, neutralising the refraction of the natural cornea by means of an artificial surface (Block (1961)). However, due to the impracticality of his theories, they ceased before implementation.

In 1632, Rene Descartes suggested the idea of corneal contact lenses, which entailed a tube, that was filled with water and placed directly against the cornea. The idea was good, but it was discarded as it proved to be impractical because the tube required external support. In 1801, Thomas Young, an English scientist, utilised the Descartes model and used wax to create a rough working model which consisted of a quarter inch long tube with a lens on one end filled with water. He affixed the water filled lenses to his eyes, and he was able to neutralise his own refractive power, correcting it with a pair of lenses (Sánchez and Muñoz (2012),Selinger (1997)).

In 1827, Sir John F. W. Herschel, an English astronomer, suggested that a glass lens could be used as a protector of the eye against infections. He also suggested making a mould of the cornea for the lens to be able to fit perfectly in the eye and that the inside curvature of the glass should be ground to be as close as possible to the irregular surfaced cornea. His contribution to optical theory was vital in the development of making mould shapes of lenses.

Adolph Fick, August Muller and Eugene Kalt took advantage of the ideas in the late 1800's and, working independently, created the first corneoscleral shell contact lenses (Schifrin and Rich (1984), Schifrin and Rich (1984)). These lenses consisted of blown glass, and moulded from animals, cadaver eyes and live humans. The glass lenses were relatively successful and they showed promise in correcting vision and protected the eye from infectious eyelids. They were called scleral contact lenses because the covered the whole eye including the white part. Even though visual correction was attained to a certain degree, the lens had some major drawbacks. They were uncomfortable, thick and heavy. They required months of fittings in order to fit perfectly to the patients and they were painful to take off, (Sánchez and Muñoz (2012)).

Major developments in the industry were seen in the late 1930's, when Theodore Obrig and Enerst Mullen, introduced a plastic scleral lens. The building block

material was polymethyl methacrylate (PMMA), which was easier to wear due to being lighter than glass. That led to the design of the first plastic corneal lens from PMMA in 1948 by Kevin Touhy (Goodlaw (2002)). The lenses covered only the corneal area. They were light, comfort amble and popularly known as hard contact lenses.

Even though PMMA was easy to wear, comfortable, light and clear, it was not a good material for a contact lens. It did not allow enough oxygen to flow into the cornea resulting in discomfort, leading to more research being conducted in search of the suitable material that would be able to allow oxygen to flow to the cornea.

In 1958, Otto Wichlerte, discovered polyhydroxyethyl methacrylate (pHEMA) and created the first soft contact lens. The material developed from soft plastic, which if placed in an aqueous solution, became flexible while retaining its original shape. Many shapes could be moulded or cut from the material. When made into contacts, it could allow enough oxygen to flow into the cornea, an advantage over PMMA (Schifrin and Rich (1984)).

However, discoveries were made that both the hard and soft contact lenses resulted in patients developing various medical conditions that would result in blurry vision and no tolerance for the lenses. That led to more research to be undertaken to find an even better and suitable material that would minimise any compromise caused to the eyes.

Further research was conducted and in 1970, silicone and methacrylate combinations produced rigid gas permeable lenses. In 1978, the FDA approved the first rigid gas permeable lens material made out of cellulose acetate butyrate. The high oxygen transmissible gas permeable lens produced better visualisation and did not fall off due to blinking.

Meanwhile, research was also going on for the development of intraocular contact lenses, which were the first surgically implanted lenses by H. Ridley, a London ophthalmologist, in 1949. The artificial plastic lenses where used to replace the natural lenses damaged due to injury or disease (Siviglia (2010)). The surgeon came up with the idea of utilising Plexiglass® lens implants based on the experience of doctors treating pilots involved in airplane accidents during World War II. When

Plexiglass® debris from shattered airplane canopies were found to be merged in an injured pilot's eye, it was found that the plastic was well tolerated by the body and in many cases it was found better to leave the pieces in place rather than damage the eye further by removing them.

Ridley theorised that Plexiglass® lens could be surgically inserted into the eye to provide permanent vision correction for cataract patients whose opaque natural lens had been removed (Selinger (1997)). The dense natural lens would be emulsified by a method of vibration and it would then be removed through the same narrow incision. A flexible acrylic intraocular lens would then be folded and inserted through the same incision. The lens would then unfold and restore vision to the eye (Selinger (1997), Bhogal (2012).

Since the conception of contact lenses, a multitude of research has gone to ensure safe and effective lenses (both in the interior/ exterior of the eye) for patients with visual impairments. The ideal was to provide lenses that would provide a comfortable and fair solution to patients.

Table 2 below shows a summary on the history of contact lenses from conception to development and ultimate improvements (Lace (2013), Mastertech Diamond Products Company (2016), H. M.Block (1961), Selinger (1997), Goodlaw (2002), Sánchez and Muñoz (2012)).

**Table 2: Historical overview of contact lenses.**

| Year | Individuals/ Organisations | Developmental Contribution |
|------|----------------------------|----------------------------|
| 1508 | Leonardo Da Vinci | Concept of glass contact lens |
| 1632 | René Descartes | Neutralisation of the cornea with a tube filled with water |
| 1801 | Thomas Young | Used Descartes principle to produce optical theory |
| 1827 | John Herschel | Introduced the concept of moulding the eye |
| 1888 | F. A. Muller | Designed and fitted a glass blown lens to protect the eye of a patient |
| 1888 | A. E. Fick | Developed a device called 'contact crystal' |

| | | to correct vision |
|---|---|---|
| 1888 | E. Kalt | Designed and fitted glass corneal lenses; utilised as a pressure treatment for keratocones |
| 1936 | W. Feinbloom | Made lenses with a glass corneal part and opaque plastic resin scleral portion |
| 1936 | Rhom and Hass (USA) | Developed contact lenses with translucent polymethyl methacrylate (PMMA) |
| 1940 | T. Obrig | Produced scleral lenses with transparent plastic; and examined the lenses using ultraviolet fluorescent light |
| 1944 | Obrig Laboratories (N.Y.) | Started manufacture of haptic PMMA contact lenses |
| 1947 | K. Tuohy | Created corneal plastic lenses |
| 1949 | H. Ridley (London) | Surgical implantation of artificial contact lenses (intraocular lens) to replace a damaged natural lens. |
| 1950 | G. Butterfield | Performed modifications by adding peripheral curves to the internal surface in order to match the curvature of the cornea. |
| 1961 | O. Wichtele | Produced hydrogel type contact lenses using poly hydroxyethyl methacrylate (HEMA) |
| 1968 | USA FDA | Active involvement in the regulation of contact lenses |
| 1971 | Bausch & Lomb | First to attain FDA approval to manufacture hydrogel contact lenses for daily wear |
| 1970's | J. DeCarle | Provided extended wear contact lenses with high water content hydrogels |
| 1970's | Rynco Scientific | Produced gas permeable hard contact lenses made of cellulose acetate butyrate (CAB) polymer |
| 1970's | | First marketing of asymmetric 'toric' contact |

| | | lenses used for the correction of astigmatism. |
|---|---|---|
| 1978 | Danker Laboratories | U.S. FDA approval of CAB lenses |
| 1979 | Syntex Opthalmic | U.S. FDA approval of PMMA-silicone copolymer lens |
| 1980's | | Tinted soft contact lenses are available |
| 1980's | | Disposable soft contact lenses that could be worn up to a week are made available |
| 1980's | | Rigid gas permeable (RGP) lenses available for round the clock wear up to a week |

## 2.2.2 Contact lens requirements

There are certain factors that need consideration when designing contact lenses because the lens is continuously in contact with the fluid of the eye. When the contact lens is inside the eye, what separates it from the eye is a tear layer knows as tear film. In the tear film, there is water, proteins, lipids, sodium, calcium, bicarbonate, and enzymes. If the contact lens is a hydrophobic material, it will repel water, which makes up the majority of the tear film. That will disrupt the tear flow, resulting in the deposition of an albumin film on the lens, which then reduces the effectiveness of contact lens. That can then cause infections and/or irritations ((Bergin (2000), Persico (2016), Giraldez and Pimentel (2012)). To avoid that, the hydrophobic material would need to convert into a hydrophilic and such a method includes doping the polymer to change the morphology of the surface. That is wettability of the contact lens material and it is not the only factor responsible for protein deposits on the contact lens.

Contact lens polymers usually consist of monomers and cross-link materials that have a charge on the monomer. The charge distribution on the monomers results in attraction of proteins, due to the proteins also having charge distributions, which attract one another. The protein deposit can create a biofilm on the lens which could result in the lens turning yellow and losing its ocular properties (Christie and Rao

(2013)). Even though the lens must repel the formation of biofilms, it must also be able to allow enough oxygen within the eye, while removing enough carbon dioxide. If the lens does not allow enough oxygen permeability within the eye, it will suffer health problems. The permeability, Dk, is measured in units of Barrers ($10^{-10}$ $cm^3$ $O_2$ (STP) cm/$cm^2$s cmHg), where D is the diffusion coefficient, and k is the solubility coefficient ((Lai and Friends (1997)), Bergin (2000), Efron (2003)).

The contact lens polymer that contacts the eye consist of monomers, which could also, possibly contact the eye. It is empirical to ensure that during the production of the contact lens, any residual monomer or solution does not pose any health risk. Therefore, testing of the monomers for biocompatibility and ensuring that they are highly pure is crucial to prevent any contamination of the eye (Bergin (2000)).

The contact lens needs to be physically acceptable, and one such requirement is that the lens needs to be lightweight. That would allow for ease of placement of the lens in the eye comfortably without causing any ocular strain (Bennett et al. (2015)). In addition to that, the lens also needs to be strong to a certain a degree, to avoid tearing or scratching during handling, while maintaining flexibility for enough comfort. The lens needs to be economically viable by being produced cheaply and efficiently to allow for an affordable price.

### 2.2.3 Optical qualities of contact lenses

Contact lenses were invented to provide visual correction to patients through refractive correction. The optical ability of a contact lens enables them to bend parallel light rays into focus to fulfil the optical correction (Mickles and Benjamin (2015)). The contact lens has refractive power, which is the magnitude that a lens diverges or converges light, and is equivalent to the anterior and posterior surfaces, the refractive index of the material and the centre thickness of the contact lens material.

Prism, which causes image displacement, reduces when wearing contact lenses. That is due to the contact lenses following the eyes while they rotate into different gaze positions. Contact lenses minimise the off-axis aberrations that influence central vision of patients wearing spectacles because they follow line of sight with eye rotation (Mickles and Benjamin (2015)).

## 2.2.4 Types of contact lenses

The types of contact lenses that are common are hard, rigid gas permeable and soft contact lenses. Their main function is usually vision correction; however they can be used for therapeutic and cosmetic reasons (Quinn and Bassett (2007), Bennett et al. (2015)).

### 2.2.4.1 Hard contact lenses

Hard polymethyl methacrylate (PMMA) contact lenses were the first contact lenses to be introduced into the market and they have been available since the early 1950's. They consist of an amorphous three-dimensional polymer matrix which typically consists of a methyl methacrylate (MMA) derivative that is below its glass transition temperature (Schifrin and Rich (1984), Bergin (2000)). The MMA monomer is polymerised using ultra-violet or infrared radiation in the presence of initiators or cross-linkers.

The PMMA polymer is cheap and easy to make, and is naturally stiff, containing a high modulus of elasticity (~ 3300 MPa (25 $^o$C)) (Bangs Laboratories (2015)). The PMMA polymer is classified as hydrophobic and that characteristic aids in the repulsion of proteins (Bergin (2000)). The oxygen permeability is typically 0.5 Dk, making it an impermeable membrane to oxygen and carbon dioxide. The impermeablility restricts the PMMA lenses for extended use, enabling them for use for up to eight hours of daily wear. Leading to more research conducted on the lenses.

### 2.2.4.2 Rigid Gas Permeable (RGP) contact lenses

In the 1970's, it was found that copolymerizing MMA with silicone acrylate, could overcome the impermeability of PMMA. Norman Gaylord, a scientist, copolymerised methacryloxypropyl tris(trimethysiloxy silane), (TRIS), with MMA, which resulted in a polymer that had the strength of MMA but also the oxygen permeability of silicone.

The PMMA-TRIS lens was the first successful RGP lens. It was referred to as RGP lenses because it was hard and possessed the optical properties of PMMA.
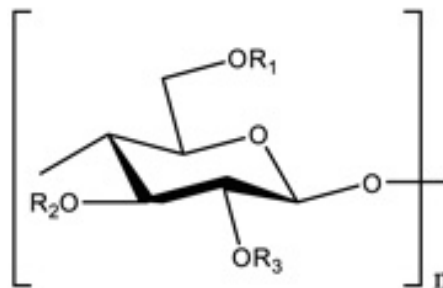


**Figure 13: Rigid Gas Permeable combination.**

The PMMA-TRIS lens had slight problems because TRIS is a hydrophobic and lipophilic, so the material dissolves in lipids. In addition, the RGP lenses did not have the required oxygen permeability for extended wear. That steered the development of extended wear lenses which started with the doping of MMA-TRIS with Fluoromethacrylates (Bergin (2000)). The doping with Fluoromethacrylates increased the free volume fraction giving oxygen and carbon dioxide room to penetrate the lens. That efficiently increased permeability of the polymer, increasing comfort and decreasing any evident strain, leading to the RGP lenses being utilised for extended wear. They presented a healthier alternative due to oxygen availability to the corneal epithelium (Bennett et al. (2015)). Even though they take some time to get used to, they require less care than soft lenses because they are not as fragile. They assist in the correction of astigmatism, provide long term comfort, stability, durability and eye protection.


*2.2.4.3 Soft contact lenses*


Soft contact lenses are different from PMMA lenses because from their basic soft quality comes their ability to absorb water (Schifrin and Rich (1984)). They usually allow oxygen transportation to the cornea and their softness and permeability make them more comfortable which is why many wearers adapt to them almost immediately. Soft contact lenses consist of thermoset polymer hydrogels and their arrangement is a three-dimensional amorphous network with cross-links. These

lenses are soft because the polymer is above the glass transition temperature (Bergin (2000)).

The water content of the lens varies between 30 – 90%, which aids in the flexibility of the lens, but this amount of water can affect several things attributed to visual clarity and lens strength. The increase in the percentage of water in the lens leads to an increase the permeability relatively linearly (Bergin (2000)). That is, the more water in the lens the less clear the images provided by the lens. In addition, the lens is not as strong as a hard lens and that makes them easy to tear, scratch or damage. Trying to overcome these deficiencies by reducing the water content in order to increase visual clarity and durability, sacrifices comfort; and making a thinner lens by reducing the plastic content leads to an increase in fragility.

These are some of the problems associated with soft contact lenses and furthermore, the lenses cannot be easily modified (Schifrin and Rich (1984)). The extensively available ready to wear lenses do not meet the needs of all the patients but are available for most common corrections (near-sightedness & far-sightedness) with the original fit being close enough and the flexibility providing the built-in modification element.

The lenses ability to absorb various amount of water makes them highly hydrophilic which enables the contact lens to achieve permeability, and that allows them for extended wear without damage to the eye. They can be worn up to 15 and even 30 days extended wear (Schifrin and Rich (1984)). Extended lenses offer the benefit of leaving the lens on continuously, instead of inserting and removing the lens daily. That helps patients with severely poor eyesight or people troubled by unsteady hands.

## 2.2.5 Manufacturing of contact lenses

Contact lenses are manufactured by three primary ways, namely, spin casting, cast moulding and lathe cutting.

*2.2.5.1 Spin casting*

Spin casting involves placing a liquid monomer in a mould and then rotating that mould, polymerising the monomer inside. Figure 14 below shows the spin casting spindle and the polymerised contact lens within the rotating mould.
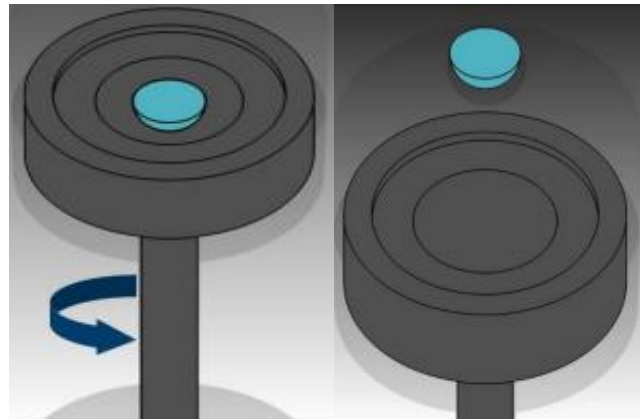


**Figure 14: Spin casting manufacturing method.**

During polymerisation, the mould creates the outer curvature of the contact lens while the centrifugal force shapes the inner curvature (Efron (2003)). The conventional process has the advantage of varying the lens optics by varying the speed of rotation and/or shape of the mould.

*2.2.5.2 Cast moulding*

Cast moulding comprises sandwiching a small amount of monomer between the anterior and posterior moulds to form the lens. Polymerisation involves placing the lens in an oven, subject to fast temperature rise and curing process. During cast moulding, the lens parameters can be varied by changing the shape of the anterior and posterior moulds producing the required lens to suite customer requirements (Bergin (2000)). Figure 15 shows cast moulding process.
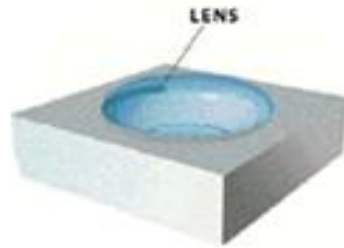
**Figure 15: Cast moulding manufacturing method.**

*2.2.5.3 Lathe cutting*

During lathe cutting, the monomer is bulk polymerised into rods, which are cut into buttons. The buttons are then placed into a computer aided lathe machine to machine them into the contact lens using an industrial diamond cutting tool (Rogers and Roblee). Figure 16 shows the lathe process.
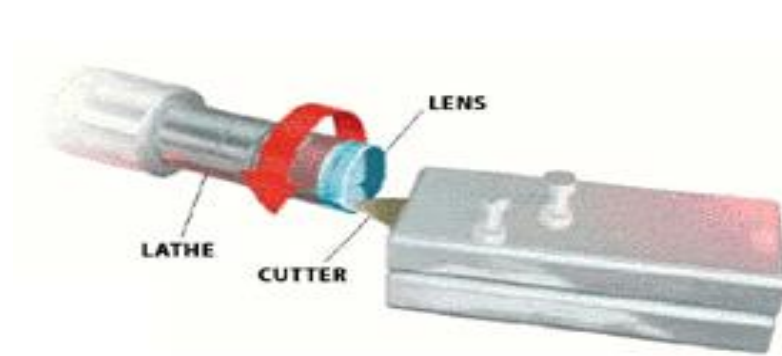


**Figure 16: Lathe cutting method.**

Upon machining the posterior surface, a super fine abrasive paste is applied to remove any inherent imperfections. Once the paste has been applied and cleaned, the lens button is mounted onto a metal arbour using melted wax to enable the shaping of the anterior surface. Upon completing all machining, the lens goes for further paste application and is hydrated with a PH saline solution that will allow the lens to expand and for the desired shape.

## 2.3 Ultra-high precision machining

Ultra-high precision machining utilises a machine that has a cutting tool to shape or cut material, usually called a work piece, secured by a chuck. The movement of the cutting tool is computer controlled providing the cutting toolpath. Figure 17 shows an ultra-high precision machine (Venkatesh and Izman (2007)).



X, Z and C motion
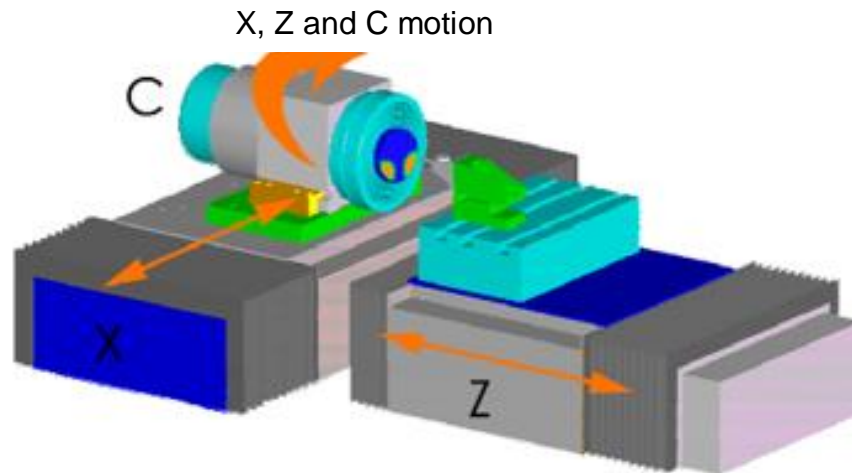
**Figure 17: Ultra-high precision machining machine.**

The method of machining spans over a thousand years evolving from astronomy, to metrology, and to the manufacture of money. It is a method used to obtain the highest dimensional accuracy when conventional machining is unable to produce such (Evans (2012)). Such dimensional accuracy and high precision has certain requirements that need to be satisfied before it can be achieved (Venkatesh and Izman (2007)):

- A highly precise movement needs to be created
- The dispersion of the part's function needs to be reduced
- Fitting needs to be eliminated and automatic assembly needs to be promoted
- The initial and running costs need to be reduced
- The machines' life span needs to be extended
- Interchangeability of components needs to be improved to enable replacement
- Scrap and reworks need to be reduced by improved quality control through higher accuracy
- Independent functionality needs to be promoted

43

Satisfying the requirements holistically promotes the production of good quality products during machining.


## 2.3.1 History of ultra-precision machining method


The demand for the commercial use of ultra-high precision machining dates from the early 1960s, with the manufacture of computer components, nuclear energy and defence systems, which comprised of surface finishes in the nanometre range and form accuracies in the micron or sub-micron range (Venkatesh and Izman (2007)). That led to the categorisation of precision engineering into micro-technology, in which the physical scale of the product was in micrometres (mm); and the nano-technology, in which the dimensions and tolerances were in the nanometer (nm). Illustrated in Figure 18, are the historical developments of precision machining based on the Taniguchi chart, (Taniguchi was the pioneer that coined the term Nano-technology in 1974).
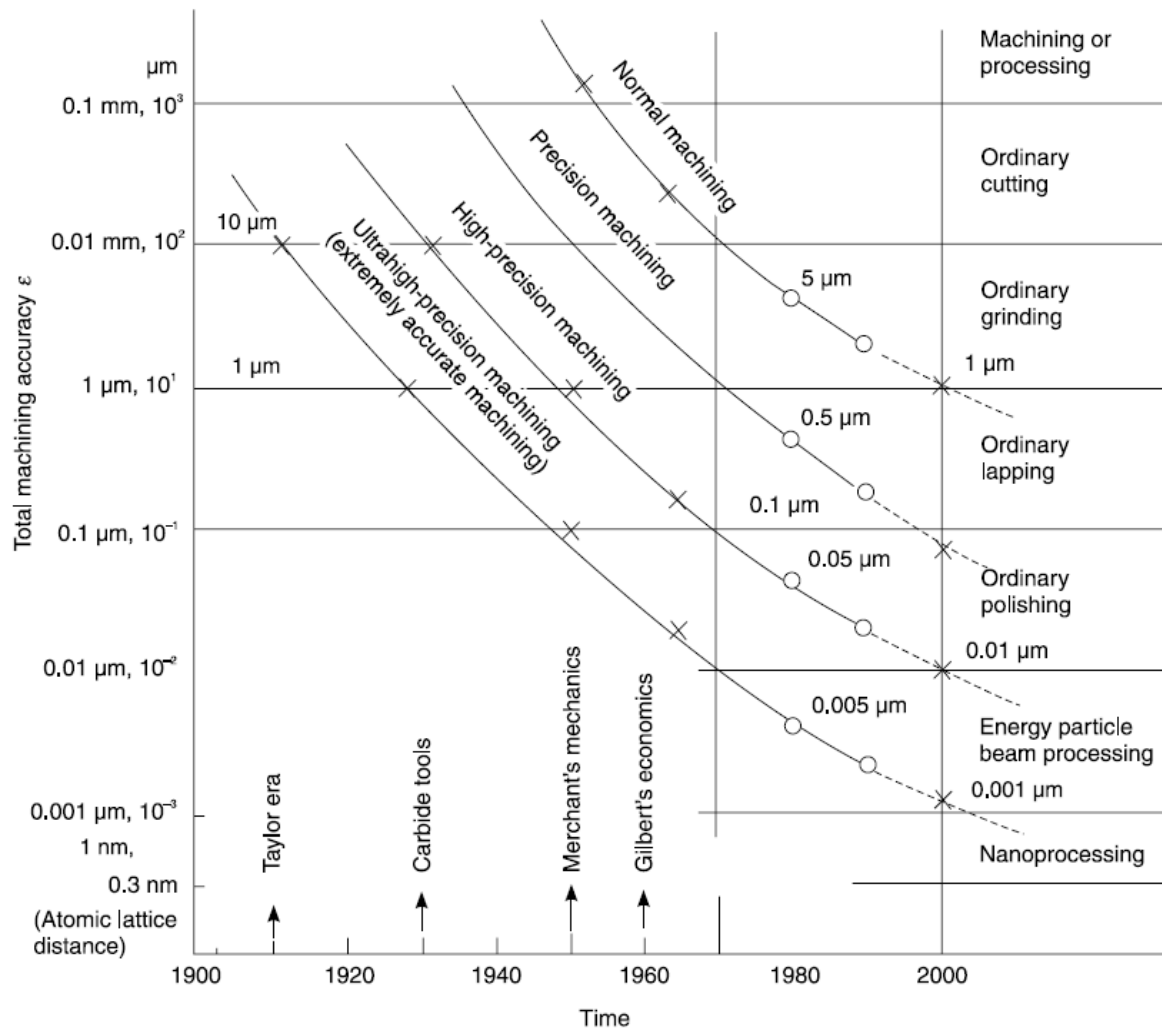
**Figure 18: Developments of ultra-high precision machining based on the Taniguchi method.**

The chart indicates the rapid growth in the field of machining, with nanotechnology leading to the development of new materials and products. The technology has become a driving force for ultra-high precision engineering techniques for the production of smaller, faster and cheaper products.

Ultra-high precision and nanotechnology processes include (Venkatesh and Izman (2007)):

- Single point diamond turning or cubic boron nitride machining
- Abrasive processes such as grinding or horning
- Free abrasive (erosion) processes such as lapping and polishing
- Chemical (corrosion) processes such as precise etch machining
- Energy beam processes such as removal, deformation and accretion

Although the technology has originated as diamond machining from the 1950's to 1970's, with the original use for metal optics at macroscopic dimensions, its uses are extensive. They include machining compact discs, video players, televisions, cameras, binoculars and contact lenses, to name a few (Riemer (2011), Evans (2012)). Since the 1980s, ultra-precision has evolved leading to the mass production of aspheric optical lenses, optical Fresnel lenses, optical diffractive gratings and ophthalmic lenses (Venkatesh and Izman (2007)). Figure 19 displays some of the optical elements produced with ultra-high precision turning (Felipe Zaragozi Optica (2016), Corp. (2016 ), Laser Components (2016)).
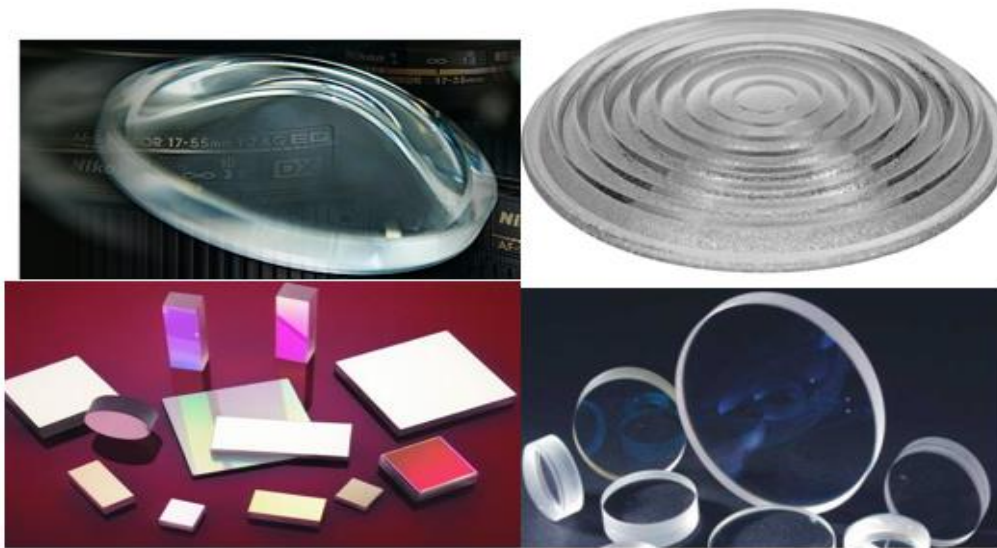


**Figure 19: Optical lenses produced by ultra-precision machining.**
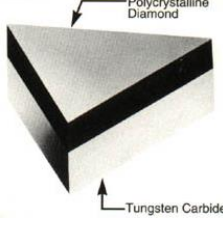
## 2.3.2 Diamond as a machining tool

Diamond is one of the hardest and most wear resistant materials in the world and it can be either single crystalline or polycrystalline in nature. Chemical vapour deposition (CVD) or high temperature and pressure synthesis (HPHT) are two of the most commonly employed methods on each class of the diamond to synthesize it (Venkatesh and Izman (2007)). Polycrystalline diamonds are usually synthesized using high temperatures and pressures, to form the diamond tool generally abbreviated as 'PCD'. Diamond particles of the order of 1 – 30 microns, are sintered together in the presence of a cobalt catalyst to produce an inter-grown mass of

diamond grains. The cobalt renders PCD electro-discharge machinable and implants a significant degree of toughening in order to provide a more robust blank. The PCD, is sintered directly to a tungsten carbide back to create ease of fabrication.

The polycrystalline form of diamond made by CVD is synthesised from a hot carbon-rich gas at atmospheric pressure and comprises of diamond grains without a cobalt binder (Engdahl (2006)). The diamond coatings grow atom by atom onto the surface of the cutting tool producing a diamond film over its surface. The coatings are between 4 – 50 microns in thickness, depending on the tool diameter and the tool application. Table 3 below shows different types of diamonds tools with their inherent properties (Mastertech Diamond Products Company (2016), Oakland Diamond Tools LLC (2016)).

**Table 3: Properties of the different diamond tools**

| Property | Single Crystalline Diamond | Poly-Crystalline Diamond | Chemical Vapour Diamond |
|---|---|---|---|
| |  |  |  |
| Micro-hardness (HV) | ~8000 - 10400 | ~8000 | ~ 7000 - 9000 |
| Thermal Conductivity (w/cm-C) @ room temperature | ~1000 - 2000 | ~500 | ~500 - 1500 |
| Fracture Toughness (MPa/m$^2$) | 3.4 | 9.0 | 5.5 |
| Density (x1000 Kg/m$^3$) | 3.52 | 4.10 | 3.52 |
| Advantages | Produces mirror finish surfaces | Cheap to buy Used for turning, | Extreme abrasion resistance |

|  | Does not contain any grain structure | milling, shaping and boring applications<br>Widely used in wear applications other than cutting tools, namely; guide pads on high precision reamers | Has high thermal conductivity<br>Can operate at extremely high speeds |
|---|---|---|---|
| Disadvantages | Can undergo adhesion, abrasion and even tribo-chemical wear during machining | Can fail catastrophically if it exceeds 730$^{o}$C during machining | All diamond tools cannot machine alloys whose main element is iron, nickel or cobalt |

Natural diamond is utilised to make single crystal diamond tools that are used in ultra-high precision machining to produce ultra-smooth surface finishes. The natural diamond is classified according to the amount of impurity atoms, such as nitrogen and boron clusters, as type I or type II. Type I diamond tools contain a high amount of nitrogen and type II contain a less amount. Both these groups are then broken further down to subclasses a and b. Type Ia diamonds usually contain clusters of nitrogen and type Ib will contain single substitutional nitrogen atoms (Oomen and Eisses (1992)).

Type IIa diamonds usually contain very little nitrogen, making them almost pure. Type IIb diamonds also contain little nitrogen but have a significant amount of boron. The type II diamonds are very rare and they are quite expensive. They usually come in aquamarine or deep blue colour presentation. They have semiconductor properties and are good conductors of heat. Table 4 below displays a classification of the diamond tools (Oomen and Eisses (1992)).

**Table 4: Diamond tools classification according to amount of Nitrogen and Boron**

| | DIAMOND TOOLS CLASSIFICATION | | | |
|---|---|---|---|---|
| | TYPE I | | TYPE II | |
| | TYPE Ia | TYPE Ib | TYPE IIa | TYPE IIb |
| Nitrogen (ppm) Boron (ppm) | ~200 – 2400 None Clustered groups of N | ~40 None Single substitutional N | ~8 – 40 None Very pure Semiconductor principles | ~5 – 40 ~0.5 >N but substantial amount of B Heat conductor |

## 2.3.3 Single point diamond turning (SPDT)

The first record of single natural diamond turning dates to 1779, where, Ramsden used diamond to cut a hardened steel screw for diving engines. Later on in the 1900's, the Carl Zeiss Company utilised single point diamond turning (SPDT) to produce aspheric surfaces. Unfortunately, the surface quality was too poor to be used in camera lenses (Evans (2012), Davies et al. (2003)). The surface finish was enhanced for use in aesthetic applications and then later, for optical functionality. In 1929, Bausch manufactured surfaces with excellent accuracy at that time reporting mirror-like surface finishes (Evans (2012)).

Polaroid Corp, in the United States of America (USA), and Phillips, in Holland, contributed to the emergence of fabrication of optics using single point diamond turning for the manufacturing of Schmidt correctors for infrared optical systems, during the World War II. Their efforts where followed by Rank Taylor Hobson, when he used a polar coordinate aspheric generation machine to produce quality camera lenses in the 1950's (Davies et al. (2003)).

During the early 1960's, precision machining was an important factor in the production of nuclei weapons. Engineers at Oak Ridge's Y-12 plant applied SPDT to study process effects during research efforts for machine performance using polished single crystal diamond microtome knives as their original tools (Evans

(2012), Luttrell (2010)). The Ultra-Precision Positioner and Shaper (UPPS), which emerged from the collaborative efforts between Du Pont and the Union Carbide Y – 12 plant, used both conventional tools and diamond knives.

The 1970's and 1980's saw the development of standard commercial machines, leading to commercial applications. Such applications included the production of hard disk substrates, photocopier drums, laser scanning mirrors and high reflective road signs (Kobayashi and Hirakawa (1984), Rhorer and Evans (2010)). The increase in consumer electronics and their dependency on optics fuelled a massive growth in use of aspherics and unconventional geometries attainable with diamond turning. Polygon mirrors, contact lenses, infra-red lasers made from germanium and moulds for compact disc lenses where also being manufactured. The relatively new technology proved to achieve higher form and shape accuracies as compared to the traditional polishing and grinding methods.

Other advantages of diamond turning over more traditional optical fabrication methods include (Rhorer and Evans (2010)):

- SPDT provided excellent optical surfaces with uniform edges
- Was able to machine difficult ductile materials
- Created aspheric shapes that would be difficult to lap
- Fabricated some of the most difficult optical shapes, such as axicons and x-ray telescopes
- Reduced alignment errors because it is a single process

Advancements continued in SPDT machines to increase productivity, accuracy and cost efficiency and they include:

- Thermal and mechanical stability with good damping properties obtained from epoxy granite or natural granite bases.
- Linear axes furnished with hydrostatic oil bearings to provide wear free and smooth motions at the highest geometrical accuracies.
- High-resolution linear scales that provide nanometric axis positioning and enhanced geometric accuracy, replacing laser interferometers.
- Linear motors that provide high feed rates and dynamic stiffness.

- High load capacity and stiffness aerostatic spindles that ensure high-speed operations.

- High speed Computer Numeric Control (CNC) processes for superior data control.

- Cutting-edge drive and feedback devices to improve workpiece accuracy.

- Multi-axis machines, fast tool servo and slow slide servo turning for freeform processes.

- Dedicated software for freeform operations and real time metrology.

Even though SPDT has advanced greatly and has notable advantages than conventional machining, it has a limitation of being unable to machine ferrous materials (Casstevens (1983)). The damage on the tool is usually due to a transformation of the surface layer of diamond carbon to graphite, with iron the chemical agent responsible for the transformation. However, it can machine nonferrous materials, infra-red materials and plastics relatively well and produce surface roughness of superior quality.

## 2.4 Surface Roughness

Generally, a surface is the layer that separates objects or substances from each other and roughness, lay and waviness are components of the surface texture. Roughness includes any imperfections on the surface. Lay denotes the principal direction of the surface texture and waviness represents the longer wavelength deviations of a surface from its nominal shape. Figure 20 shows the surface roughness properties (Novin (2015)).
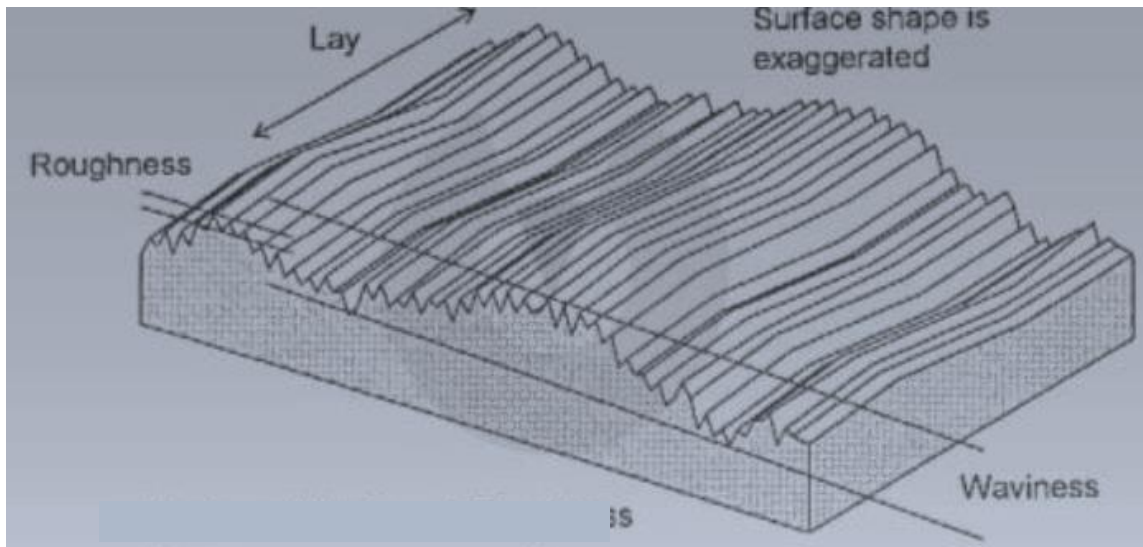
**Figure 20: Surface roughness properties.**

Surface roughness plays an important characteristic in determining how the real object interacts with the environment. The nature of the contact between two surfaces is vital in understanding the nature of the friction between the two surfaces. Surfaces that are rough have higher friction coefficient and usually wear fast (Kadirgama et al. (2009), Poon and Bhushan (1995)). With the increasing requirement for high quality surfaces of nanometric range, roughness is often a good predictor of the performance, since irregularities in the surface may form cracks, corrosion or debris deposits (Zhanga et al. (2015)). Fortunately, ultra-precision machining is an efficient and low cost method for generating smooth surfaces that require no post polishing.

The methods for measuring surface roughness include a stylus profiler, a non-contact optical profiler, an atomic force microscope and a scanning tunnelling microscope (Poon and Bhushan (1995)). The stylus profiler is loaded on the surface and electrical impulses translated onto the surface are released. The stylus moves at a constant velocity to obtain the average height variation. On a non-contact optical profiler, the principle of two-beam optical interferometry is used. An electronic-phase measurement technique is used with linear, solid – state, detector array to provide make available profile data (Wyant et al. (1986)). An atomic force microscope utilises a sharp tip located at the end of a lever maintained in contact with the surface under very small loads. In a scanning tunnelling microscope, a metal tip is maintained

within a small distance and a voltage is applied between two electrodes of the metal tip and surface.

A tunnelling current will flow between the two electrodes and it will change according to the height variation providing the surface topography (Poon and Bhushan (1995)).

The stylus profiler and non-contact optical profiler are used for microscopic measurements; and the atomic force and scanning tunnelling microscope, are used for ultramicroscopic measurements (Poon and Bhushan (1995)).A measure of the surface roughness that is commonly used is the average roughness ($R_a$) which denotes the area between the roughness profile and the mean line. It can also be described as the integral of the absolute value of the roughness profile over the evaluated length (Novin (2015)). Figure 21 shows the graphical representation of the surface roughness and the mathematical expression, shown in Equation 1.
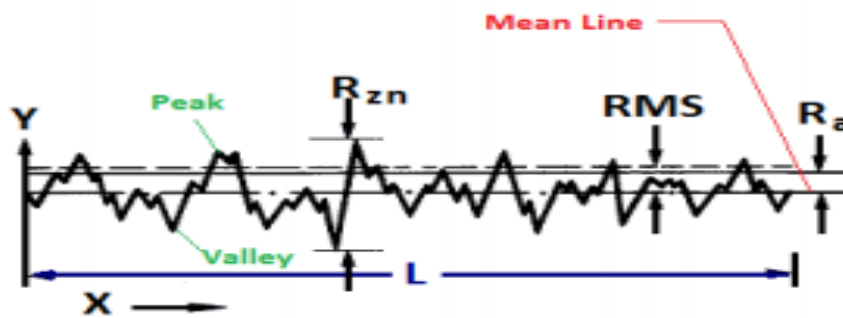


**Figure 21: Average surface roughness.**

$$R_a = \frac{1}{L}\int_0^L |f(x)| dx \qquad (1)$$

Where $R_a$ represents the surface roughness, also known as the arithmetic mean; L represents the sampling length and f(x) is the roughness curve.

Table 5 shows other measured surface roughness parameters (Giraldez and Pimentel (2012)):

**Table 5: Surface roughness parameters.**

| Parameter | Name |
|-----------|------|
| $R_q$ | Root mean square (RMS) roughness |
| $R_t$ | Maximum height of profile |
| $R_v$ | Maximum profile valley depth |

| $R_p$ | Maximum profile peak height |
|---|---|
| $R_{pm}$ | Average maximum height of the profile |
| $R_z$ | Average maximum height of profile |
| $R_{max}$ | Maximum roughness depth |
| $R_c$ | Mean height of profile irregularities |
| $R_y$ | Maximum height of the profile |

## 2.4.1 Factors affecting surface roughness

Manufacturing processes have the capability of machining products with nanometric accuracy; however, the products can still have unwanted defects translated onto the surface due to the machining process being affected by static and dynamic factors (Zhanga et al. (2015)). These factors range from machine vibrations, cutting parameters, tool geometry, environmental conditions, materials properties, chip formation and tool wear. The defects that could develop have the potential of affecting the functionality of the material, so it becomes important to analyse which factors affect the surface roughness.

Chon et al. (2008) explored the fabrication of a Wolter type I mirror by using SPDT to machine electroless nickel. The cutting parameters studied were restricted to rotational speed and feed rate in an effort to prevent machine vibrations. Cutting mist oil was also applied and the results showed an improved surface roughness which could be attributed to applying those boundaries.

Jagtap and Pawade (2014) studied the effects of cutting parameters on the surface quality during SPDT of polymethyl methacrylate (PMMA). Their results revealed that the cutting speed was dominant on the flatness of the surface. Goel et al. (2011) confirmed that the rotational speed and cutting feed where prominent factors that affected surface roughness, waviness and profile accuracy during SPDT of PMMA. However, both their results showed that the application of cutting fluid during machining reduced the optical transmission of PMMA, leading to a conclusion that cutting fluid was not required during precision machining of PMMA.

Jagtap et al. (2012) observed that the feed rate had an influence on the surface roughness during the machining of nylon and polypropylene. The roughness was directly proportional to the feed rate, so when the feed rate was high, the roughness was also high, a condition to avoid because that implied that the surface finish was poor. The results also showed that minimum surface roughness was achieved with minimum depth of cut for both specimens.

Chong et al. (2012) analysed the effects of varying the depth of cut during SPDT of two Lanthanum based metallic round glass bars (N102 & N103). Both materials showed a significant influence by the depth of cut because the surface roughness was improved in the range between 1 µm to 5 µm. Beyond 5 µm, both materials did not show any improved surface roughness instead the results were steady. The study also showed that material properties influenced the surface roughness.

Chao et al. (2008) altered the material properties of hardness Stavarx stainless steel and used SPDT to machine the surface. The iron (Fe) atoms were bonded to nitrogen atom to form $Fe(x)N$ phases. The expectation was that the diamond tool would get blunt faster leading to a poor surface finish. However, the modification of the material characteristics showed a superior surface finish as opposed to what was expected. That showed that altering the work piece properties affected the surface roughness and machining tool.

Yang et al. (2012) analysed aluminium (Al 6061), silicon (Si), germanium (Ge) and KDP crystals, trying to relate the surface roughness to material anisotropy, impurities, inclusions and micro-structures, rake angle, tool cutting edge waviness and the degree of wear on the tool. The results showed that the ductile materials needed a tool with no rake angle to produce an optically acceptable surface finish; and for a brittle material, a cutting tool with negative rake angle provided a good surface finish.

Han et al. (2007) utilised SPDT to manufacture diffractive optical surfaces. They concluded that the diamond tool tip, tip radius and tool feed had significant effects on the fabrication quality and performance of diffractive optical elements machined using SPDT.

The swelling factor is another property that affects surface generation during SPDT. Zhao et al. (2011) used copper, aluminium alloy and eletroless nickel phosphorus to understand the relationship between cutting parameters, the swelling factor and surface roughness. Their results indicated that the swelling factor was affected by the spindle speed and material properties. A softer and more ductile material led to a stronger material recovery, a lower swelling proportion, a lower tool mark height and a smoother machined surface.

## 2.5 Tool wear

Cutting tools are relatively expensive, so selection of optimal cutting conditions must balance the trade-off between productivity and tool life, and thus studying the cutting conditions is important to decipher the behaviour on wear (Venkatesh and Izman (2007)). Tool wear is a phenomenon that is prominent during SPDT because some materials can cause fast tool wear or catastrophic failure, bringing into question the accuracy of the machined product (Thornton and Wilks (1980)). That suggests that some materials can be diamond machined, and other cannot.

Casstevens (1983) suggested that for steel, the damage on the tool was usually due to a transformation of the surface layer of diamond carbon to graphite, with iron the chemical agent responsible for the transformation. Thornton and Wilks (1980), observed that chemical wear during SPDT of mild steel. Yingfei et al. (2010) also validated that the chemical wear did take place on the single crystal diamond (SCD) while examining the patterns between it and the polycrystalline diamond (PCD) tool, while machining silicon carbide (Sic) particle-reinforced 2009 aluminium matrix composite under wet cutting conditions. The SCD exhibited micro-wear, chipping, cleavage, abrasive and chemical wear. The PCD tool displayed abrasive wear on the rake face and adhesive wear on the flank face. The results showed that the different diamond tools responded differently to the same set of cutting conditions suggesting that the tool properties affected the process (Yingfei et al. (2010)).

Chao et al. (2008) modified the chemical structure of hardened Stavarx stainless by injecting nitrogen into it. The results revealed that diamond tool wear was improved due to the modification of the surface microstructure.Tanaka et al. (2005) utilised

SPDT to machine copper powder using five different monocrystalline diamond tools subjected to high temperature in the air. The results showed that the strength of the diamond tool in contact with the copper at high temperatures decreased due to a thermo-chemical erosion at the atomic scale at the crack tip, together with a catalytic reaction of copper and ambient oxygen. Therefore, cutting under a reduced oxygen atmosphere, which would suppress the strength of the diamond tool, proved effective in supressing cutting edge chipping in SPDT of copper.

Gubbels et al. (2004) analysed the wear mechanism significant, during SPDT of poly carbonate (PC) and PMMA. The study showed that triboelectric wear was active during dry cutting of both materials. However, it was not the dominant wear, tribo-chemical tool wear was the most significant. The study stated that that was due to the observed chain scissions, which resulted in highly reactive radicals. The radicals were regarded as the main active particles that initiated chemical transformation. That was contrary to the claim that Paul and Evans made, that no chemical wear takes place during SPDT of plastics since they do not have unpaired d-shell electrons (Zhang et al. (2016).

The measurement of tool wear is vital during machining operations since the severity of the tool wear has a consequence on the replacement time, product quality and cost implications. Various methods exist for tool wear measurement and monitoring ranging from imagery, sound and decision making techniques. The optical microscope is the most direct and simplest method for tool wear monitoring. It measures tool wear land through optical amplification. The latest version or development is the differential interference contrast microscope used to observe diamond tool wear by providing 3D-like images, which make it easier to measure the tool wear land. Another tool used is the atomic force microscope (AFM), it is utilised during measurement of the diamond tool cutting edge, and is regarded an efficient technique that is able to map the tool tip by capturing wear. Zong et al. (2010) used the AFM during their study for advanced measurements for tool waviness in order to obtain the nose radii accurately.

A scanning electron microscope (SEM) is also another apparatus that is used to measure tool wear. It provides high-resolution imaging up to the order on 1nm and it can determine the chemical compositions produced after diamond tool wear takes

place. Zong et al. (2010) utilised the SEM to inspect the cutting edge radius to determine the extent of damage on the diamond tool.

Other methods include the electron beam-induced deposition (EBID) and acoustic emission and noise measurement methods. During EBID, a hydrocarbon contamination stripe, deposited onto the diamond tool, and is then measured by SEM with a known angle. The stripe profile is then be calculated and the cutting tool edge profile obtained. In acoustic emission and noise measurement, a correlation between the diamond tool wear rate and the sound emitted during cutting is established and it is used to determine the extent of the wear rate (Rmili et al. (2006).

## 2.5.1 Triboelectric wear

The contact on solid surfaces can produce a variety of material and energy outputs resulting in the transformation of energy, which is an input by rolling, rubbing or sliding, into other forms of output energy. The energy input also provides the driving force for a number of physical and chemical changes on the surface which can result in damage and/or transformation (Molina (2000)). During SPDT of polymers, the charge accumulates at the cut surface and results in an electric field, which can create a discharge between the workpiece and the diamond tool, which could cause tool wear. Gubbels (2006) reported the wear mechanism as tribo-electric wear.

Gubbels (2006) described two mechanisms of tribo-electric wear. The first was the consequence of electric discharge from tribo-electric charging which lead to the transfer of electrons. The electrons would be trapped and accumulate in the material locally generating an electric field. The electric field would increase until the material breakdown strength was attained. That breakdown would lead to the formation of fractal geometries resembling Litctenberg figures on the material surface, as shown in Figure 22 below ((Ficker et al. (2005)).

The second mechanism involved the detachment of carbon atoms by impacting electrons or ions. These electrons or ions accelerated due to the presence of an electric field. This acceleration would then lead to an increase on the kinetic energy and once it reached a critical value, the particles would be able to impair the diamond surface. The high electrostatic field strength would even generate a luminescence (Gubbels et al. (2004)).
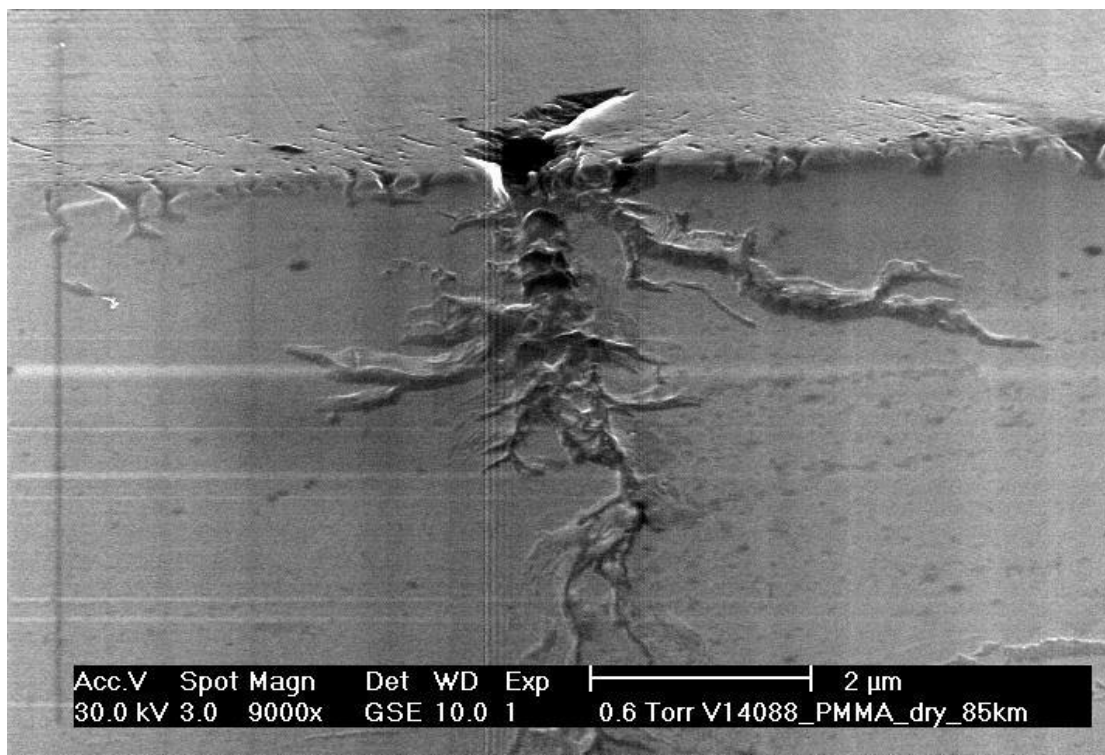


**Figure 22: Lichtenberg figure.**

Olufayo et al. (2014) during their study on the effects of machining parameters (cutting speed, feed, and depth of cut) during SPDT of contact lens polymers; found that low feed and high speed resulted in charging effects. They based that on the prolonged contact at low feed and the high frequency, which resulted in the electrostatic potential. Contrary to what was found by Kadernani that the cutting speed, feed rate and depth of cut had no significant impact on the electrostatic behaviour of the polymer, even though measurements for electrostatic potential where measured, they were due to an external influence (Kadernani (2014). The

researchers studied materials with different characteristics and that could be the influence on their results.

### 2.5.1.1 Tribo-electric charging and discharging

Electrostatic charging is utilised and deemed crucial in many applications. Such applications include electrophotography (e.g. photocopying and laser printing), electrostatic coaters, the movement of small particles (e.g. sand or fragments) in dust storms and dust clouds, and the movement of air, water droplets and ice particles in storms and the generation of lightning. Electrostatic charging can also cause attraction or repulsion of materials, creating manufacturing difficulties. It can also cause explosion risks in operating theatres due to static electric sparks which ignite mixtures of gaseous anaesthetics and oxygen (Wiles et al. (2003), Soh et al. (2012), Friedle and Thomas (2010),Myshkin et al. (2005)).

The phenomena of charge build up between two dissimilar materials due to contact or friction charging is known as tribo-electric charging or contact electrification. The mechanical processes that produce the charging of materials include sliding, rolling, rubbing, impact, vibration of the surface contact, and separation of solid – solid, solid – liquid, and liquid – liquid surfaces (Mazumdera et al. (2006)).

Zhang and Shao (2013b), Liu et al. (2013b), Follows et al. (1991) and Liu et al. (2013a) deduced that when two dissimilar materials come in contact and separate, electrons move from one surface to another, leaving one material positive and the other, negative. However, Burgo et al. (2012),Thomas et al. (2008), McCarty and Whitesides (2008) introduced an alternative that suggested that the charge was due to the transfer of mobile ions on the surface, even though it was found that it was not possible to account for contact electrification of pyroelectric insulators due to the transfer of the surface layer of mobile ions (Robins et al. (1980)). McCarty and Whitesides (2008) even proved that in the ionic transfer mechanism, the materials in contact ought to be ionic materials. Figure 21 below depicts the transfer mechanisms.
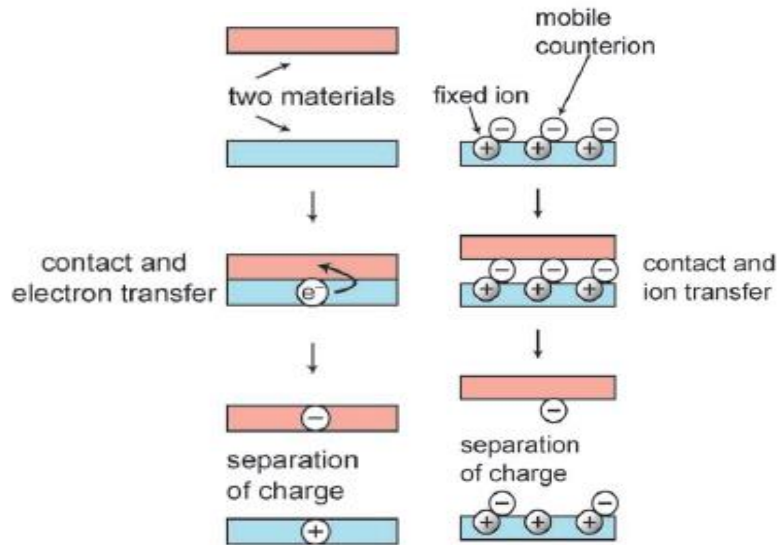
**Figure 23: Electron transfer and ion transfer mechanisms.**

The polarity and charge accumulation of the material depend on various factors which include humidity, temperature, area of contact surface and the type of material if it is polar or nonpolar (polar materials charge positively and nonpolar materials charge negatively (McCarty and Whitesides (2008)). The material will be listed in the form of a table, which is called the triboelectric series. The highest materials are usually positively charged and the lowest materials are negatively charged. Appendix A gives an example of a triboelectric series table (Lee (2009)).

Baytekin et al. (2011) found that water was not necessary for contact electrification to occur, however, it did stabilise the surface charges. Gubbels found that humidity influenced the surface charge. The surface charge was found to be inversely proportional to the relative humidity and at a 70 % relative humidity, there was no surface charge measurement recorded (Gubbels (2006)). Follows et al. (1991) proved that tribo-electric charging for nylon was a property of the material itself and that charge transfer was unaffected by dyestuffs but was affected by contaminants such as silicones. Sakaguchia et al. (2014) identified the chemical structures of the donors and acceptors by calculating the highest occupied molecular orbital (HOMO) and the lowest unoccupied molecular orbital (LUMO) energy levels during tribo-electric charging of polymers. They identified the donors as mechano anions (HOMO) and mechano radicals (HOMO), and the acceptors as mechano cations (LUMO) and mechano radicals (LUMO). They deduced that the polymer with a large

number of paths of electron acceptance becomes negative in charge, with the direction depending on the difference between the HOMO and LUMO energy levels.

Zhang and Shao (2013a) analysed the effects of contact cycle, load, and nominal area on tribo-electric charging between a polymer and steel. They found that tribo-electric charge was dependent on the contact stress and that dependency was from the structural deformation of the polymer chains. The charge decreased linearly with the increase of contact stress and increased with the real contact area. An increase in the contact load and nominal area led to an increase in the real contact area. However, the results showed that the charge decreased with the increase in the load.

## 2.6 Conclusion

With the concise understanding of several conditions necessary during SPDT of polymers used during contact lens making, it is necessary to design carefully experimental conditions by selecting the right machining parameter combinations. Chapter 3 will discuss the experimental method.

# CHAPTER 3: EXPERIMENTAL DESIGN

This section will detail the setup, which includes the machine, work piece materials, design of experiment method chosen and the parameters monitored during SPDT of contact lens polymers.

## 3.1 Machine, Cutting tool and Workpieces

The experiment was performed on the Precitech Nanoform ultragrind 250 machine, which has a four axis ultra-high precision lathe, shown in Figure 24 below. The lathe utilises the UPx CNC machine control and leads the industry with programming resolution of 0.01 nm. The machine consists of hydrostatic oil bearings sideways, which contain optimised stiffness and damping characteristics, and high-speed air bearing spindles. The ultra-high precision machine, designed for diamond turning deterministic freeform milling and grinding for complex applications, which comprise of glass grinding for plane and aspheric lenses, mould inserts for lenses and glass pressing.

**Figure 24: Precitech Nanoform ultra-grind 250 at the Precision Engineering Laboratory, Nelson Mandela Metropolitan University.**

A mono crystalline diamond was utilised with the specifications shown in Table 6.

**Table 6: Diamond tool specifications.**

| Parameter | Value |
|---|---|
| Tool | Natural diamond |
| Rake Angle | $0^o$ |
| Nose radius | 0.5 mm |
| Height | 3.4 mm |

Commercially available contact lens buttons produced by The Lagado Corporation were machined:

- ONSI™-56 and
- Polymethyl methacrylate (PMMA)

The ONSI™-56 (onsifocon A) button is a rigid silicone - hydrogel material that is used for manufacturing spherical, aspheric, toric and bifocal contact lenses. The

material is made of fluorosilicone acrylate copolymer with additional hydrophilic and crosslinking monomers. It has high oxygen transmission which enables it to maximise eye comfort as compared to other lenses and it provides a superior hydrophilic finish, Table 7 gives the material properties ((Lagado Corporation, 2014), The Lagado Corporation (2004)).

**Table 7: Material properties of ONSI-56.**

| Parameter | Value | |
|---|---|---|
| Dk | 56 | |
| Classification | Onsifocon A | |
| Refractive index | 1.452 | |
| Wetting angle | $7.2^o$ | |
| Hardness (Shore) | D/85 | |

PMMA is a hard contact lens that is highly crosslinked for stability, solvent resistance and ease of machining. It is made from ultra-pure methyl methacrylate monomer which can be machined and customised to individual needs (The Lagado Corporation (2014)). It requires minimum cleaning, soaking and wetting solutions and can last for up to 7 years. It is utilised for the manufacturing of intraocular lenses used in the treatment of cataracts; Table 8 gives the material properties.

**Table 8: Material properties of PMMA.**

| Parameter | Value | |
|---|---|---|
| Dk | < 0.02 | |
| Classification | Polymethyl methacrylate | |
| Refractive index | 1.495 | |
| Wetting angle | $25^o$ | |
| Hardness (Shore) | | |

## 3.2 Electrostatic Sensing

The electrostatic potentials (ESPs) on the material were captured with an SMC IZD10 electrostatic sensor and monitor configuration. The IZD10 has a measuring range of +/- 20kV. Figure 25 displays the electrostatic monitor and the electrostatic sensor; and Table 9 below displays the specifications for the system.
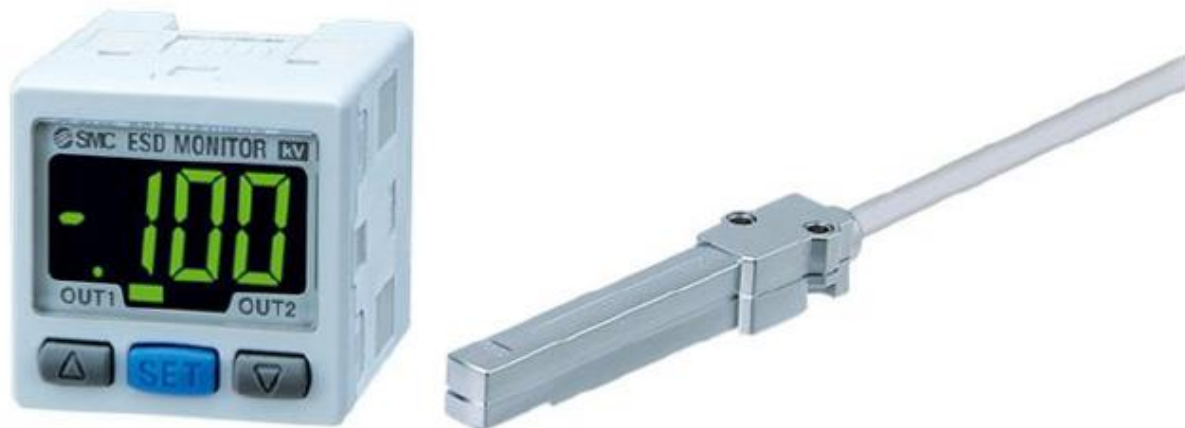


**Figure 25: IZE 11 Electrostatic monitor (left) and IZD 10 Electrostatic sensor (right).**

**Table 9: Electrical properties of the monitor and sensor.**

| Parameter | Value |
|---|---|
| Connected sensor | Sensor for ±20 kV |
| Set measured distance | 25 – 75 mm |
| Power supply voltage | 24 VDC ±10 % (inverse protection) |
| Current consumption | 50 mA or less |
| Sensor input | 1 – 5 VDC |
| Voltage output | 1 – 5 V |
| Current output | 4 – 20 mA |

The output measurement varies according to the installation distance as shown in the Figure 26 below.
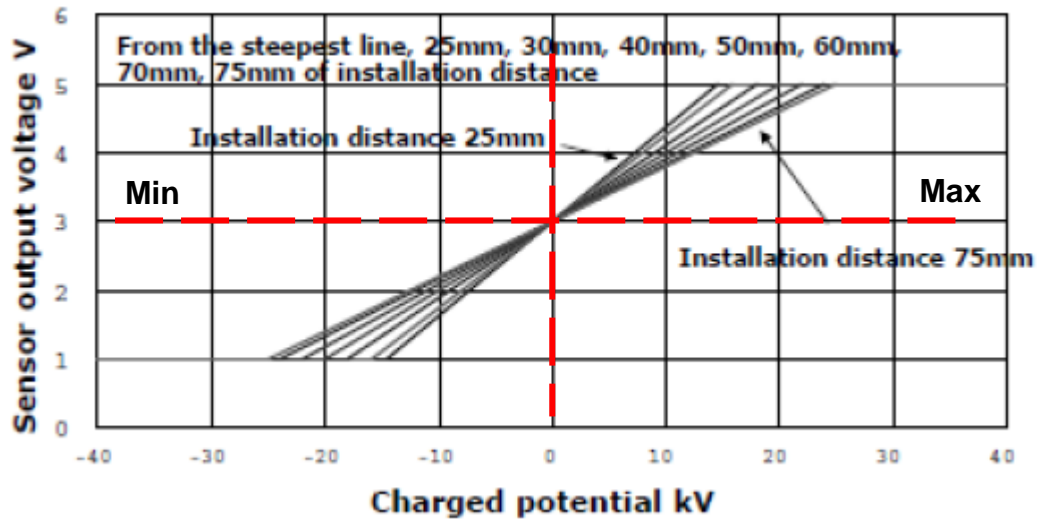
**Figure 26: Relationship between electrostatic potential and the sensor output voltage.**

Figure 26 indicates a centreline that cuts at the y – intercept that is 3V, meaning that the sensor output values start from 3V and either go up or down depending on the sensed potential. There is a linear and positive relationship between the charged potential and the sensor output voltage. This means that for a unit change in the charged potential going towards the maximum values, there will be a change in the sensor output voltage in the same direction. Similarly, if the change in the charged potential is more negative, there will be a decrease in the sensor output voltage. A positive relationship simply means that the variables move together.

The linear relationship can be represented by means of a straight line equation to mathematically correlate the charged potential to the sensor output. Figure 27 below shows how the charged potential observed on the surface of the material varies with the sensor output measurement.
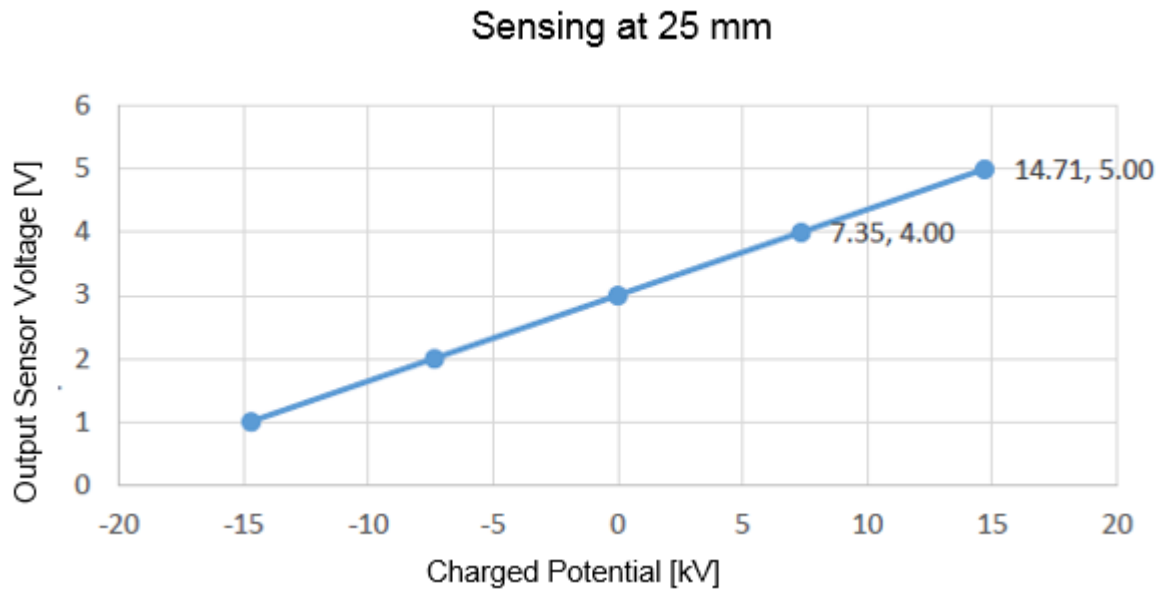
**Figure 27: Sensing range calibration.**

The gradient of the line can be calculated from:

$$m = \frac{x_2 - x_1}{y_2 - y_1} \tag{2}$$

$$= \frac{5 - 1}{14.71 - 7.35}$$

$$= \frac{1}{7.36}$$

$$= 0.136$$

Then the linear equation becomes:

$$y_o = 0.136 y_a + 3 \tag{3}$$

Where $y_o$ represents the electrostatic sensor output, and $y_a$ represents the actual charged potential.

From the installation distances indicated on the graph, 25 mm was chosen because it provided a more accurate representation of the charged potential on the material surface considering the diameter of the lens button is only 12.7 mm.

## 3.3 Signal Acquisition

The experimental process flow diagram displays a rough representation of the different elements involved during the acquisition of the electrostatic discharge; shown in Figure 28 below.
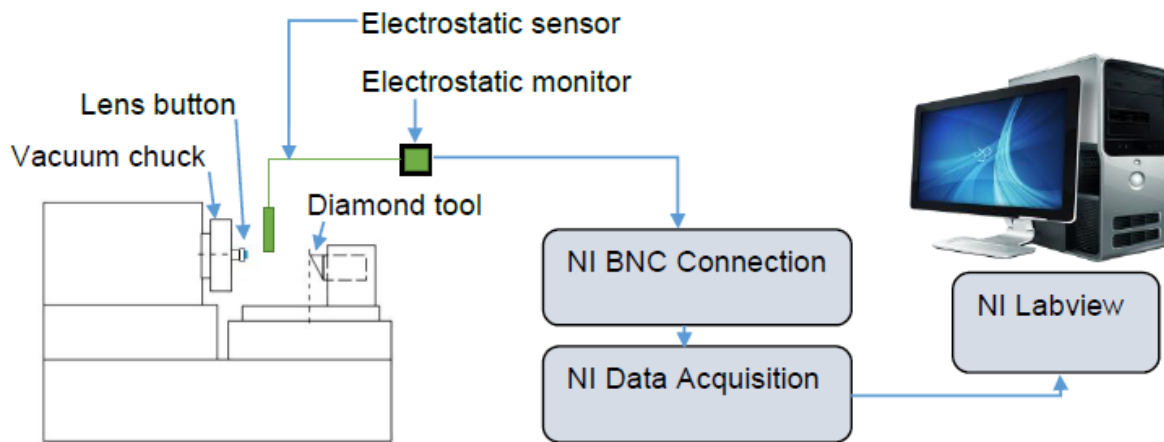


**Figure 28: Process flow diagram.**

The experimental process flow diagram comprises of the contact lens button secured in the vacuum chuck of the machine. The electrostatic sensor, which is connected to the electrostatic monitor, provides the output scaled using Equation 3 with a range of 0 – 5 V operating voltage. This output signal from the monitor goes to the National Instrument (NI) MyDAQ (USB data acquisition card) that goes to the computer operating NI LabVIEW software package. NI LabVIEW allows for the manipulation of the incoming live signal and graphically displays the discharge generated by the materials.

NI LabVIEW data acquisition program

The NI LabVIEW data acquisition program uses Equation 3 which is manipulated as:

$$y_a = 7.35y_o - 22.059 \tag{4}$$

Where $y_a$ is the actual charged potentials and $y_o$ is the sensor output voltage. Equation (4) scaled the sensor output voltage to provide the actual discharge measurements.
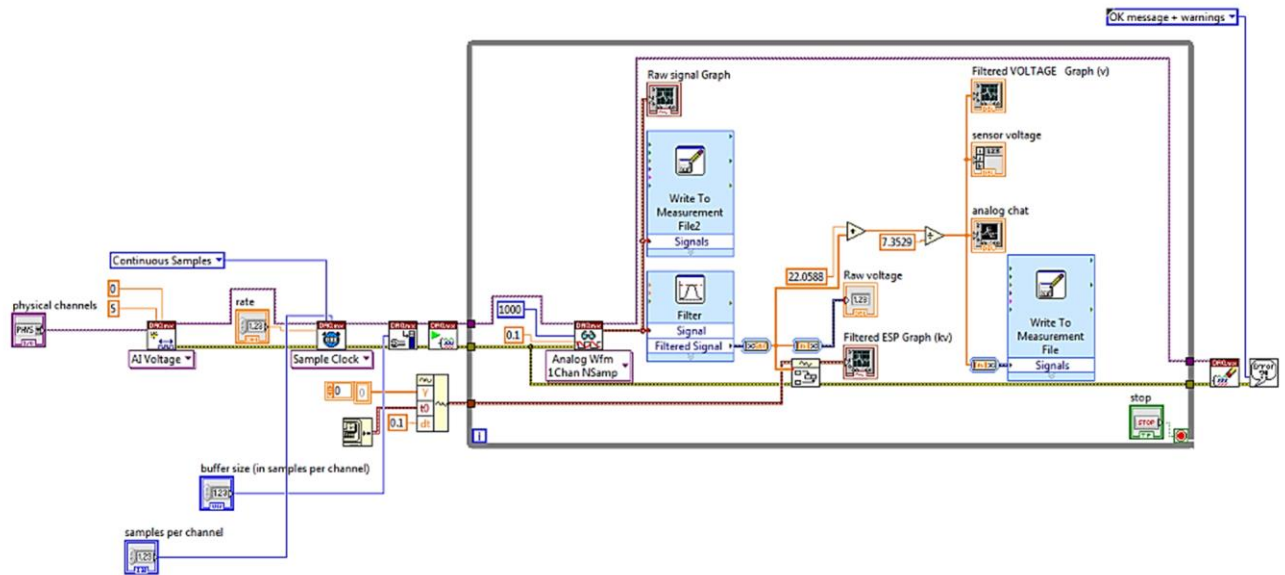


**Figure 29: NI LabVIEW block diagram.**

Figure 29 shows the LabVIEW block diagram used. In the program, the output from the electrostatic sensor was acquired continuously at 1000 samples at a rate of 100 000 within a buffer of 100 000 000. The voltage was scaled with using Equation 4, and it was plotted on the graph. The front panel shown in Figure 30 displayed the raw signal and the filtered signal of the electrostatic discharge, the converted and filtered sensor voltage and the analogue chart.
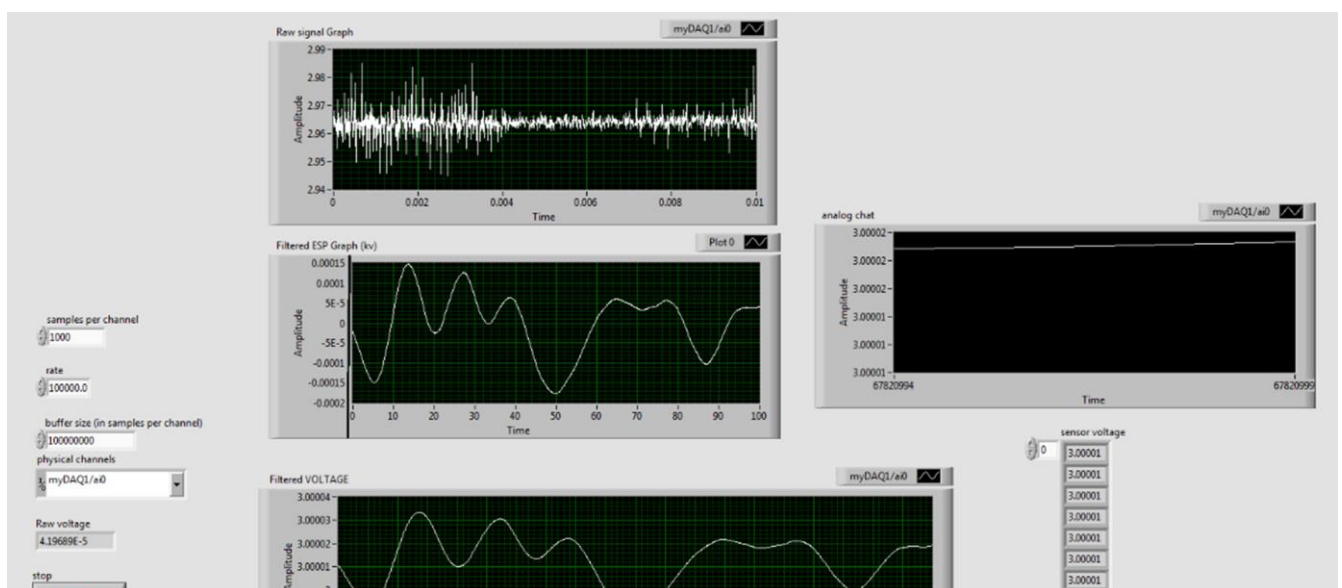


**Figure 30: NI LabVIEW front panel.**

70

## 3.4 Machining parameters

The machining parameters chosen were speed, feed, and depth of cut. Figure 31 displays a diagram that shows the operating direction for the machining parameters and Table 10 shows the parameter values.
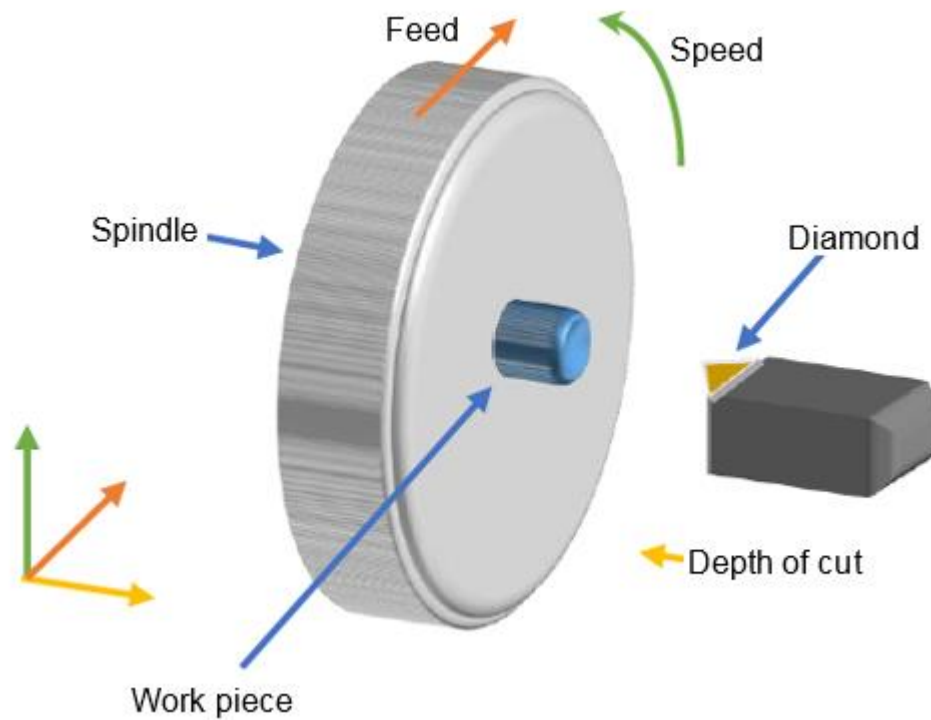


**Figure 31: Parameters used during machining.**

**Table 10: Machining parameters used in the experimental analysis.**

| Parameter | Low | High |
|---|---|---|
| Speed | 200 rpm | 4000 rpm |
| Feed | 2 mm/min | 12 mm/min |
| Depth of cut | 10 µm | 40 µm |
| Humidity | 50 – 60 % (uncontrolled) | |

## 3.5 Surface Measurements

The surface roughness measurements were carried out using the Taylor Hobson PGI Dimension XL Surface Profilometer as shown in Figure 32.



**Figure 32: Taylor Hobson PGI Dimension XL surface profilometer at the Precision Engineering Laboratory, Nelson Mandela Metropolitan University.**

The Taylor Hobson PGI Dimension XL has 300 mm diameter capability, an automated 3D measurement system. It has a fast stylus trace speed of 100 mm/s with an automated centre and level. It boasts with class leading accuracy and repeatability as it can enhance roughness measurements up to 0.2 nm resolution ((Ametek Ultra Precision Technologies).

## 3.6 Design of Experiments (DOE)

Surface finish and dimensional accuracy during SPDT are affected by various factors, such factors include material properties of the sample, the condition of the diamond tool, the cutting parameters, and the environmental conditions (Xu et al. (2012)). Optimising the experimental design provides increased performance of the machining system and cost effectiveness.

Experimental design methods, statistical methods and mathematical models have increasingly become popular for analysis and process optimisation. Statistical design of experiments refers to the procedure that involves planning experiments, such that appropriate data is statistically estimated to provide objective conclusions.

Factorial design, Response Surface Method (RSM), Taguchi method, and Artificial Neural Network (ANN) are commonly used instead of traditional one factor at a time experimental approach which is time consuming and unreliable (Goel et al. (2016), Borad and Shrikrishna (2015), Montgomery (2013)).

The RSM technique seeks to establish the relationship between independent variables and one or more responses. It was developed around the 1950s by Box and Wilson for the use in the Chemistry field, based on the pioneering works of R. A. Fisher (1931) who developed factorial designs for agricultural purposes(Box and Wilson (1992),Box and Hunter (1957)). With the successful initial implementation of the method in the agricultural and chemical fields, the method saw wide spread application in production engineering processes such as milling, turning, grinding, press work and many more.

The RSM provides a quantifiable relationship between the independent variables and the process response. The general representation of the relationship is with a first – degree polynomial, with the assumption that y will represent the process response, and x will represent the input factor. The equation can be written as follows:

$$y = \beta_0 + \sum_{i=1}^{n} \beta_i x_i + \epsilon \qquad (5)$$

Where i represents the number of independent variables, $\beta_0$ represents the y – intercept when x = 0, $\beta_1$ represents the slope, and $\epsilon$, the random error (Box and Wilson (1992)). If two independent variables, $x_1$ and $x_2$, are used to model a relationship with the response, the equation becomes:

$$y = \beta_0 + \beta_1 x_1 + \beta_2 x_2 + \epsilon \qquad (6)$$

The first order model is usually enough in predicting responses, however, it is mainly applicable to a linear relationship. Relationships with curvature require a more comprehensive second degree model, represented by Equation 7:

$$y = \beta_0 + \sum_{j=1}^{n} \beta_j x_j + \sum\sum_{i<j} \beta_{ij} x_i x_j + \sum_{j=1}^{n} \beta_{jj} x_j^2 + \epsilon \qquad (7)$$

Expanding Equation 7, in terms of variables $x_1$ and $x_2$, results in:

$$y = \beta_0 + \beta_1 x_1 + \beta_2 x_2 + \beta_{12} x_1 x_2 + \beta_{11} x_1^2 + \beta_{22} x_2^2 + \epsilon \qquad (8)$$

An optimisation model needs to satisfy certain assumptions which include Montgomery (2013):

- The mean of the probability distribution of the residuals needs to be 0 for each of the independent variables of x
- The variance of the probability distribution of the residuals has to be constant for all settings of the independent variable x
- The residuals associated with any two different observations need to be independent
- The probability of the residuals associated with any two different observations need to be independent

## 3.6.1 Central Composite Design (CCD)

Central Composite Design (CCD) is one of the popular RSM and DOE techniques employed during process analysis and optimisation. It consists of a factional or complete factorial design, an axial portion consisting of 2k points such that two points are chosen on the axis of each control variable at a distance of α from the design center. Centre points chosen at the origin of the coordinate system depend on the number of factors and levels selected for the design. This method provides relatively high quality predictions over the entire design space and it can be used to analyse machining parameters that will provide a precise surface finish.

Thus, the total number of design points in a CCD are:

$$N = 2^k + 2(k) + n_c \qquad (9)$$

Where N is the total number of experimental runs required, k is the number of control factors and nc is the number of center points.

Various studies have been conducted by implementing different statistical methods to optimise surface roughness. Goel et al. (2016) studied the effects of varying the tool nose radius, tool over hang, feed rate, cutting speed and depth of cut on the surface roughness, during the precision machining of polymethyl methacrylate (PMMA), using the Taguchi method. It was also used by Özel and Karpat (2005) during the machining of AISI 1030 Steel bar, to find otpimal cutting conditions. Jagtap et al. (2012) used the Taguchi design L9 orthogonal array to invest the variability of the surface roughness due to the variation in the cutting speed, feed rate, depth of cut and insert clearance angle.

Choudhury and El-Baradie (1997) applied RSM and $2^3$ factorial designs, to estimate the surface roughness during turning of high strength steel. Dabnun et al. (2005) explained the development of a response surface model during the turning of Macor, using RSM and $2^3$. Raveendran and Marimuthu (2016) utilised RSM to optimise machining parameters during the machining of glass fiber reinforced plastics.

This study will utilise CCD Face Centered because of the benefits it provides, such as covering the entire design space. The relationship for the surface roughness, as well as the ESPs in relation to the cutting speed, feed rate and depth of cut will be analysed using this method. The design is shown in Figure 33 showing the three types of points used in the design.
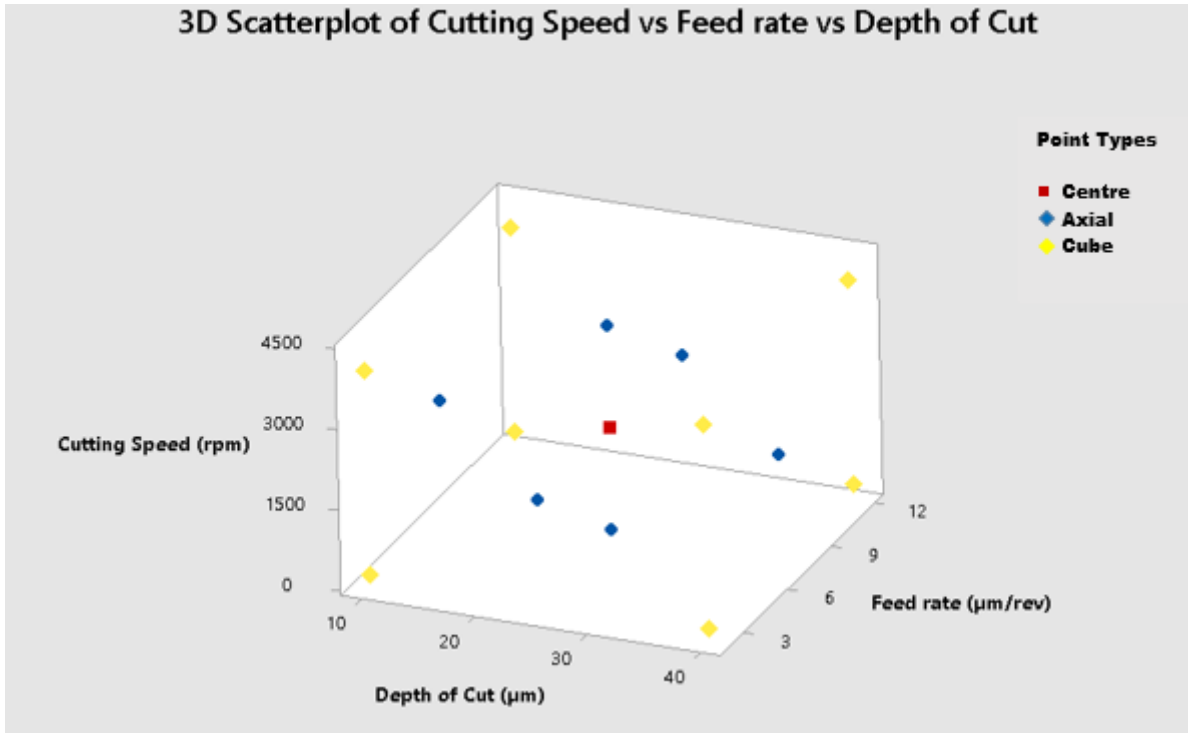
**Figure 33: Scatter diagram of the cutting parameter points.**

## 3.6.2 Application of DOE using Minitab statistical software

Minitab is the statistical software that was used to design the experimental data used in this study. A CCD design was implemented with two – level factorial design for three control variables. The RSM is analysed to obtain the model with the significant terms and analysis of variance (ANOVA) is perfomed to check the goodness of the model.

The significance of the ANOVA and all subsequent results is evaluated through the analysis of the probability or p – value. The ANOVA evaluates the variation between the groups and compares it to the variation within the groups of two or more groups of data.

 The ANOVA model can be represented by:

$$y_{ij} = \mu_i + \epsilon_{ij} \text{ for i = 1,2, …, a and j = 1,2, …, n} \tag{10}$$

Where y represents the individual observations, $\mu_i$ is the mean of the ith factor, $\epsilon_{ij}$ is the unexplained variation and i and j, the group and individual observations respectively. In general, $x_{ij}$ is said to represent its group mean plus error.

The variance between groups is the ratio of the sum squared:

$$SS_{between} = \sum_{j=1}^{p} n_j (x_j - \bar{x})^2 \tag{11}$$

And the degrees of freedom: n – 1.

The variance measures the overall variability between the groups and it is given by:

$$\sigma^2 = \frac{SS_{between}}{(n-1)} = \frac{\sum_{j=1}^{p} n_j (x_j - \bar{x})^2}{(n-1)} \tag{12}$$

There variance within the groups will be calculated similarly as:

$$SS_{within} = \sum_{j=1}^{p} \sum_{i=1}^{n_j} (x_{ij} - \bar{x})^2 \tag{13}$$

Giving:

$$\sigma^2 = \frac{SS_{within}}{(n-1)} = \frac{\sum_{j=1}^{p} n_j (x_j - \bar{x})^2}{(n-1)} \tag{14}$$

The F – ratio, which represents the relationship between the actual variations of the group averages and the expected variations of the group averages can be represented as:

$$F = \frac{Variation\ between\ groups}{Variation\ within\ groups} = \frac{SS_{between}}{SS_{within}} \tag{15}$$

And substituting into equation 15:

$$F = \frac{\sum_{j=1}^{p} n_j (x_j - \bar{x})^2}{\sum_{j=1}^{p} \sum_{i=1}^{n_j} (x_{ij} - \bar{x})^2} \tag{16}$$

A large F-value indicates a non-deterministic effect on the model by the control parameters, (which in this case are the cutting speed, feed rate and depth of cut), and is represented by the p-value which indicates the significance of their effect. The p-value is inversely proportional to the f-ratio and $p < 0.05$ shows a significant effect of the independent variables on the model.

The ANOVA indicates the significance of the model. A lack – of – fit test indicates by how much of the experimental data is attributed to pure error. It also checks if there are any contributions that have not been accounted for during the creation of the model. The lack – of – fit test is also analysed using a p – value, and its significance is indicated by a p – value < 0.05, and insignificance by p – value > 0.05. The ideal scenario for a model to fit the data at the polynomial order, is to have a lack – of – fit that has a p – value > 0.05. That indicates that there exists no evidence that the model does not adequately fit the data.

The statistical plot also ensures that the model is validated and the contour and surface plots are generated to further interpret the relationships between the control variables and the process response. A preferred model would be a model of the lowest order because it is simpler and clearer to explain.

## 3.7 The experimental Process

## 3.7.1 Initial setup

The experiments were carried out using the Precistech Nanoform ultragrind 250 precision machine under dry cutting conditions. Before the experiments were conducted, the diamond tool setup was performed, as shown in Figure 34. The work spindle was balanced at 2000 rpm clockwise direction, thereby achieving a spindle run out error of 3.454 µm high and 3.450 µm low and 0.028 µm P – V.  The balancing was done using the Precitech's DIFFSYS software interphase, to ensure the proper positioning of the vacuum chuck, to prevent any inherent vibrations that could cause affect the measured results.
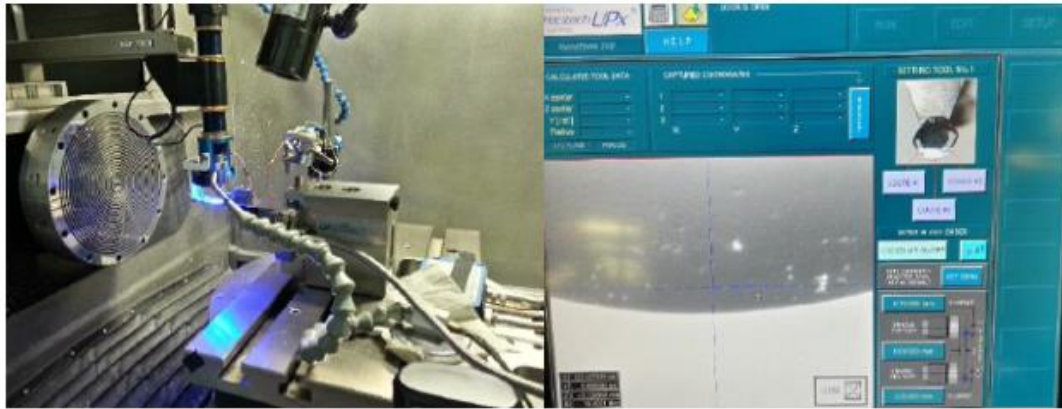
**Figure 34: Initial tool balancing.**

Once tool centering and spindle balancing was completed, the polymer buttons were blocked onto copper arbours to be mounted onto the vacuum chuck, Figure 35. The blocking process involved a wax strip that was heated into molten state. The copper arbour was warmed to allow the wax to hold, and then it was dipped into the molten wax. The lens button was then, placed onto the wax on the copper arbour, where both were placed onto the blocking machine to centre the lens button onto the arbour.



**Figure 35: Contact lens button blocking.**

## 3.7.2 Sensor Calibration

Figure 36 below displays the mounted contact lens button safely secured on the vacuum chuck, as well the electrostatic sensor 25 mm away from the contact surfaces. The electrostatic sensor received voltage from the electrostatic monitor, which was powered by an external power supply (24V). The output from the electrostatic monitor was an input to the NI myDAQ. Once the signal passed through analogue input channel 0, the data was interpreted by NI LabVIEW software package and graphically displayed. The actual configuration is shown in Figure 37 below. The initial sensor calibration steps are shown in Appendix B and the oscilloscope was used as a means to validate the authenticity of the output voltage which ranged from 0- 5 V and had a centre point of 3V (SMC Corporation).
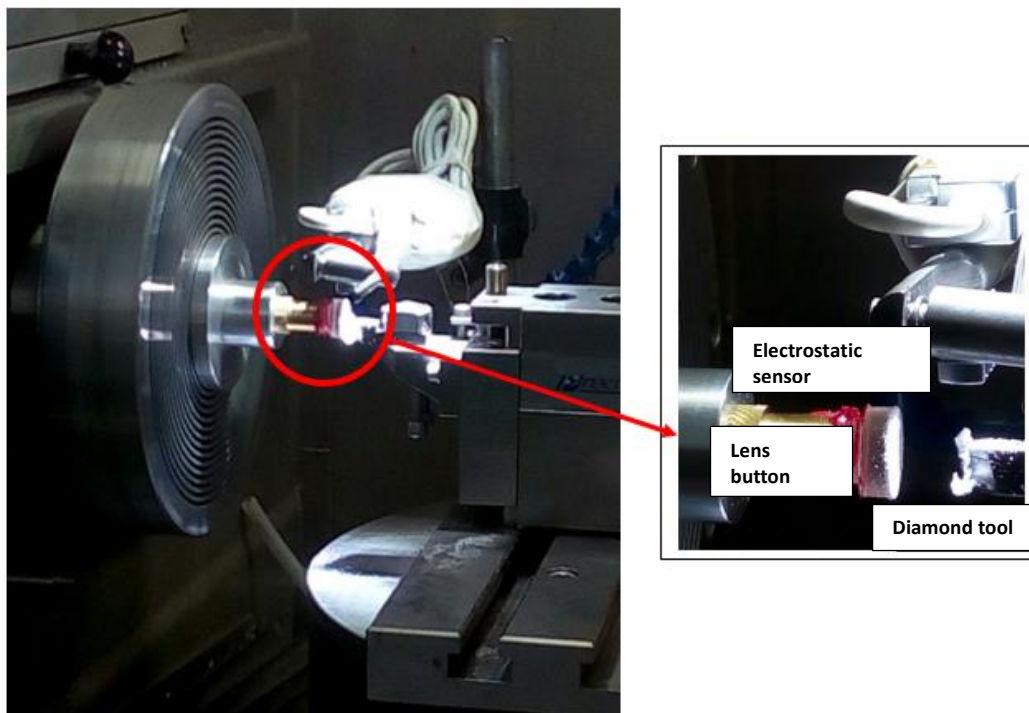


**Figure 36: Experimental setup for the machining process.**
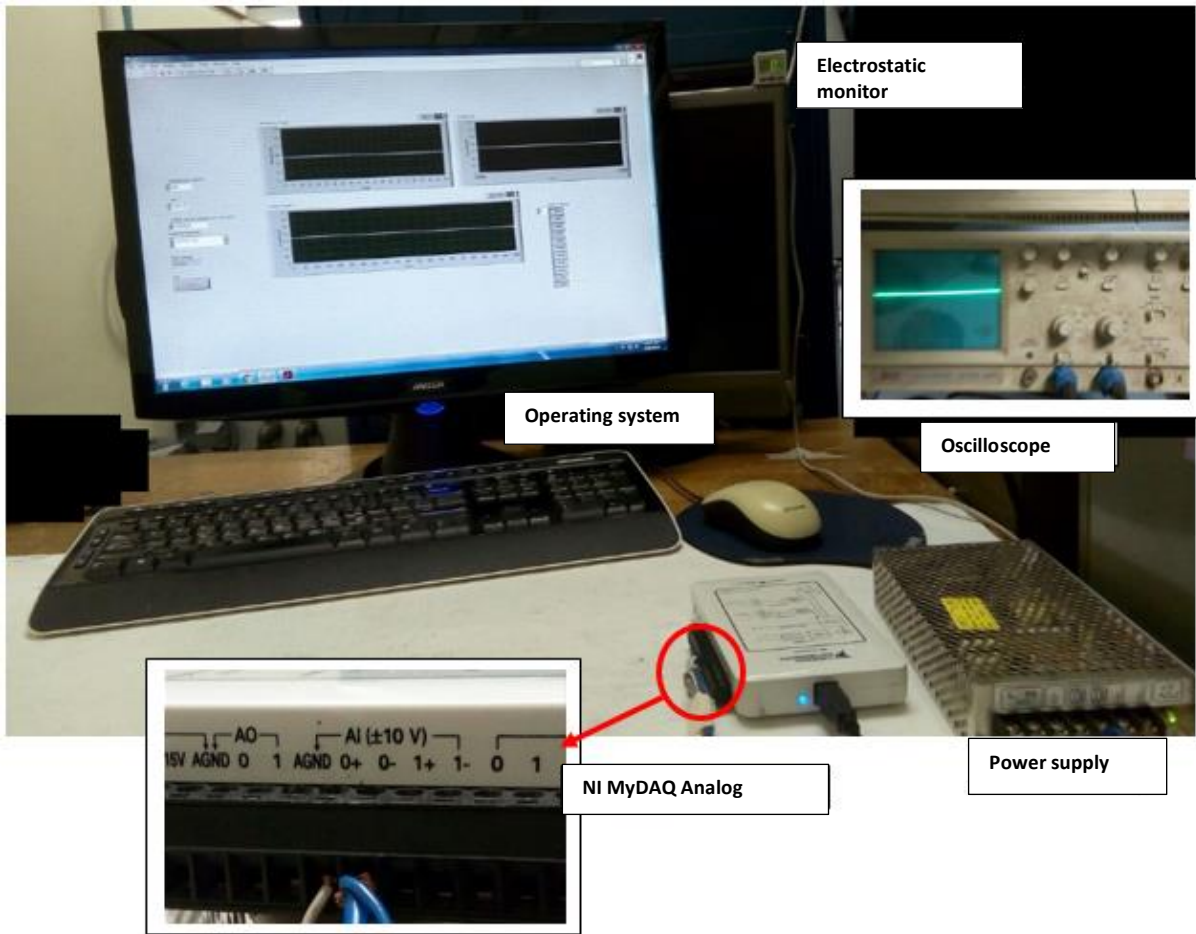
**Figure 37: Data acquisition system configuration.**

## 3.8 Experimental procedure

Once the initial setup was completed, the experiments commenced in the following order:

- The copper arbour holding the lens button was mounted onto the machine vacuum chuck
- A program was loaded using the computer aided interface with the updated parameter values for cutting speed, feed and depth of cut
- The LabVIEW program was initialised with continuous sample measurements of 1000 at a rate of 100 kHz to capture the ESP data
- For every observation completed, the contact lens button was removed from the spindle and transferred to the surface profilometer (Figure 38)
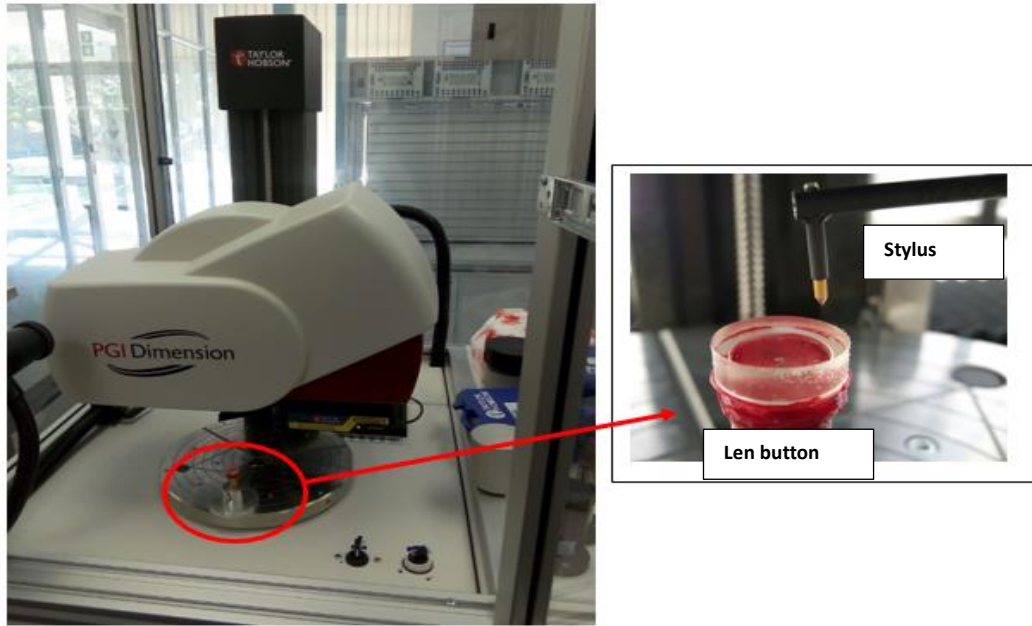
**Figure 38: Surface roughness measurements with the stylus profiler.**

## 3.8 Conclusion

The CCD Face centered design was utilised in creating 3X3 experimental domain, involving the entire design space for the selection of cutting parameters. Surface measurements were performed using the profilometer, and the LabVIEW program captured the sensor voltage readings. Chapter 4 will discuss the results and analysis.

# CHAPTER 4: RESULTS AND DISCUSSION

The first section of this chapter will detail the development of a regression model for surface roughness for ONSI – 56 and PMMA contact lens polymers. The second section will detail the application of the regression analysis for predicting electrostatic discharge (ESD) during diamond turning of the above polymers. The last section will compare the obtained results for ONSI – 56 and PMMA materials for both the surface roughness and the ESD. The analysis of this chapter was made possible with Minitab and Statistica statistical software's, and LabVIEW data acquisition software.

## 4.1: Surface Roughness Experiments

This section will detail the development of regression models for surface roughness during the single point diamond turning of ONSI – 56 and PMMA respectively.

### 4.1.1: Surface Roughness Measurements for ONSI – 56 contact lens button

The first set of experiments was done using ONSI – 56 contact lens button, with a 12.7 mm diameter. The experiments were performed three times for repeatability, and each time a measurement was taken with the Taylor Hobson PGI profilometer. The average surface roughness of the three measurements was used. Table 11 displays the average surface roughness measurements recorded.

**Table 11: Surface roughness measurements for ONSI-56.**

| Run Order | Cutting Speed (rpm) | Feed rate (mm/min) | Depth of Cut (µm) | Surface Roughness (nm) |
|-----------|--------------------|--------------------|-------------------|------------------------|
| 1 | 200 | 12 | 10 | 687.7 |
| 2 | 2100 | 7 | 25 | 6.0 |
| 3 | 4000 | 2 | 10 | 7.3 |
| 4 | 200 | 2 | 40 | 28.4 |
| 5 | 4000 | 12 | 40 | 11.9 |
| 6 | 2100 | 7 | 25 | 15.0 |
| 7 | 200 | 7 | 25 | 380.2 |
| 8 | 2100 | 7 | 25 | 16.0 |
| 9 | 2100 | 2 | 25 | 17.6 |
| 10 | 2100 | 7 | 10 | 21.0 |
| 11 | 2100 | 7 | 25 | 23.9 |
| 12 | 4000 | 7 | 25 | 17.1 |
| 13 | 2100 | 12 | 25 | 21.0 |
| 14 | 2100 | 7 | 40 | 20.2 |
| 15 | 4000 | 12 | 10 | 23.8 |
| 16 | 4000 | 2 | 40 | 12.4 |
| 17 | 2100 | 7 | 25 | 18.4 |
| 18 | 200 | 2 | 10 | 27.8 |
| 19 | 200 | 12 | 40 | 711.6 |
| 20 | 2100 | 7 | 25 | 23.7 |

The measured surface roughness varied between 6.0 – 711.6 nm over a range of 705.6 nm showing the variability of the measurements for the different machining parameters. Figure 39 displays the scatter plot of the surface roughness values.
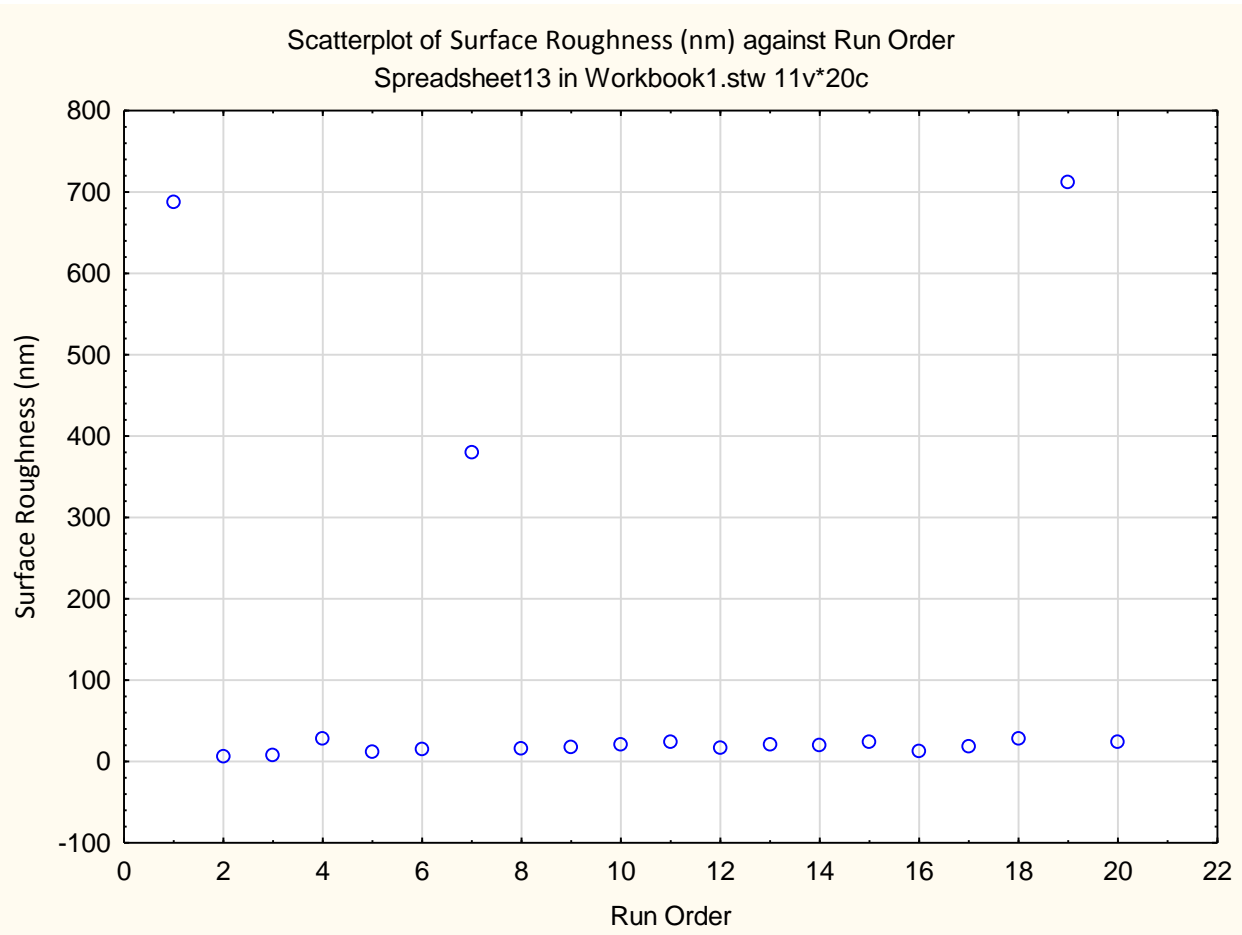
**Figure 39: Scatter diagram of the surface observations.**

For the purpose of simplifying and showing the different range of experimental observations, the surface roughness values were grouped into good, moderate and bad, according to the size of the measured surface roughness. Table 12 shows the groups of surface roughness.

**Table 12: Groups of surface roughness measurements.**

| Run Order | Range | Category |
|---|---|---|
| 2, 3, 5, 6, 8, 9, 12, 16, 17 | 0 nm – 19.9 nm | Good |
| 4, 10, 11, 13, 14, 15, 18, 20 | 20 nm – 39.9 nm | Moderate |
| 1, 7, 19 | 40 nm – 204.9 nm | Bad |

The majority of good and moderate surface roughness observations were obtained with a cutting speed between 2100 – 4000 rpm and a feed rate between 2 – 7

mm/min and a depth of cut between 10 – 40 μm. That suggested that the cutting speed and feed rate had an influence on the surface roughness, but it was not conclusive how the depth of cut affected the values because it was over its entire range. The bad surface roughness values were obtained with a speed of 200 rpm and a feed rate between 7 – 12 mm/min, leading to the assumption that a low cutting speed lead to poor surface quality. The surface roughness profile obtained from the Taylor Hobson PGI profilometer with a good surface roughness of 6.0 nm obtained from observation 2, is displayed in Figure 40 below.
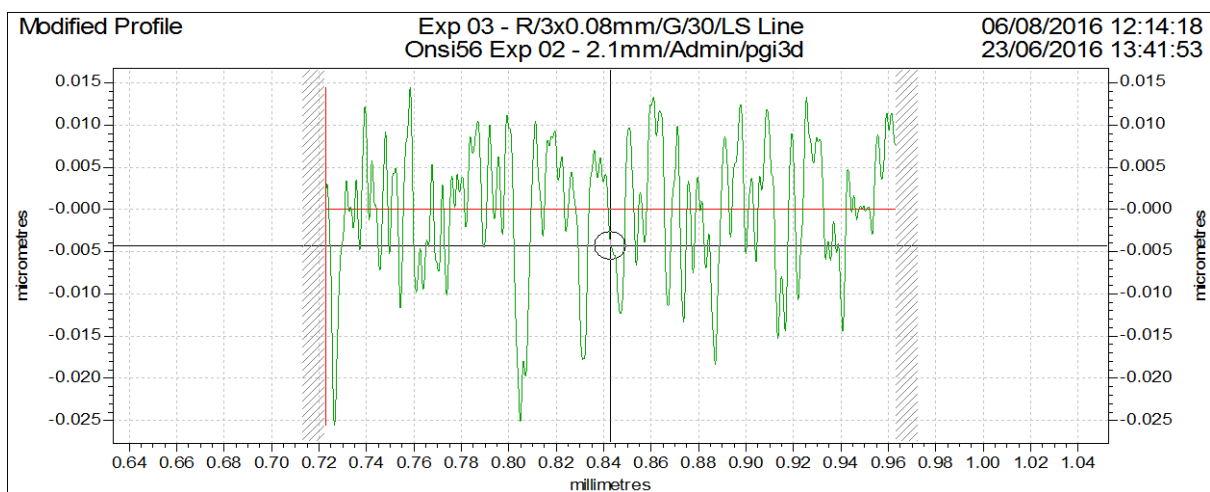


**Figure 40: Surface profile of experimental observation 2.**

The surface roughness was obtained with a cutting speed of 2100 rpm, a feed rate of 7 mm/min and a depth of cut of 25 μm. The surface profile in Figure 40 shows that the tool marks did not translate onto the workpiece during cutting, hence the good surface finish.

Contrary to that, Figure 41 shows a profile of a poor surface finish, obtained from experiment 19, with a recorded value of 711.6 nm. The surface roughness was obtained with a cutting speed of 200 rpm, a feed rate of 12 mm/min and a depth of cut of 40 μm. The tool marks translated onto the workpiece surface producing the poor surface finish.
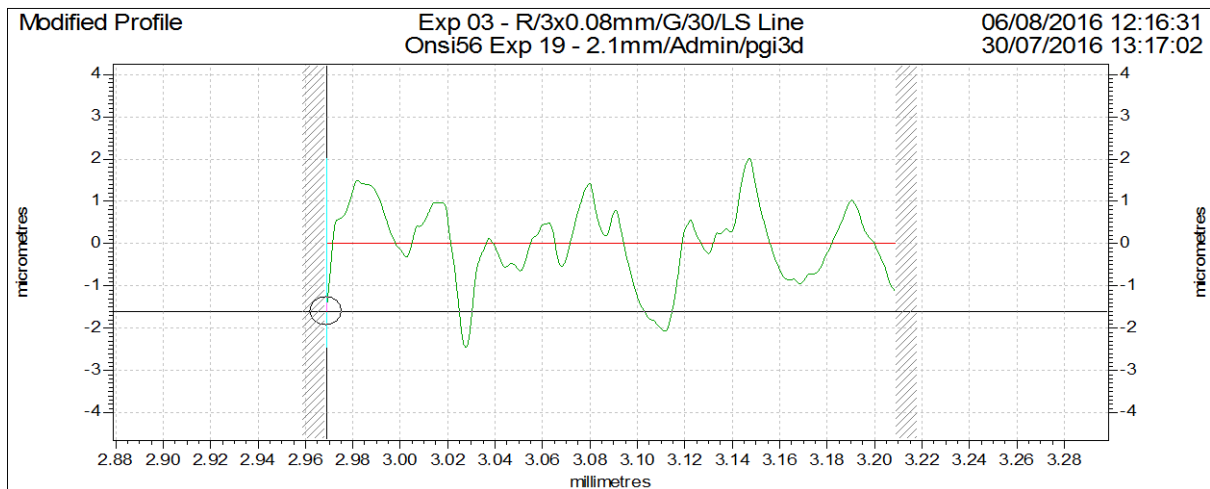
**Figure 41: Surface profile of experimental observation 19.**

The two surface profiles clearly show that the cutting parameters were affecting the surface roughness. The good surface roughness had the mid-point cutting speed, feed rate and depth of cut. From Table 11, experiment 3 also had a good surface roughness of 7.3 nm, obtained with the maximum cutting speed, and a minimum feed rate and depth of cut. Experimental observation 19, the worst surface roughness, utilized the minimum cutting speed, and the maximum feed and depth. Leading to the assumption that the cutting speed and feed were the parameters with the greatest influence. That assumption supports the findings of Jagtap and Olufayo, who both found that the feed rate and speed directly affected the surface roughness during their studies (Jagtap et al. (2012), Olufayo and Abou-El-Hossein (2013)). However, further analysis carried out will approve or disapprove that assumption.

## 4.1.1.1 Response Surface Modelling for ONSI – 56

Response Surface Methodology (RSM) is a collection of mathematical and statistical techniques that seek to establish a relationship between the independent variables and one or more responses during the analysis of engineering problems(Box and Hunter (1957)). During an RSM application, a sequence of planned experiments is carried out, a statistical software is used to generate the model, the model is analysed and optimized in the design space. The independent variables that affect the variability of the model assist in building a polynomial model for predicting the response.

The model needs to satisfy the following assumptions:

- The response needs to be normally distributed
- The residuals of the observations need to be independent of each other
- The mean of the probability distribution of the residuals needs to be zero for each setting of the independent observations
- The variability of the residuals needs to be similar

After showing that there exists a relationship between the independent variables and the dependent response, the theoretical model, also called the probabilistic model is:

$$SR_{ONSI-56} = \beta_0 + \beta_1 s + \beta_2 s^2 + \beta_3 f + \beta_4 f^2 + \beta_5 d + \beta_6 d^2 + \beta_7 sf + \beta_8 sd + \beta_9 fd + \varepsilon \tag{15}$$

Where:

$SR_{ONSI-56}$ denotes the surface roughness of ONSI – 56, measured in nano-meters

s denotes the cutting speed, in revolutions per minute (rpm)

f denotes the feed rate, in millimetres per minute (mm/min)

d denotes the depth of cut, in micrometres (μm)

$s^2$, $f^2$, $d^2$ denote the non-linear component of the cutting parameters

sf, sd, fd denote the interaction effects of the cutting parameters on the surface roughness

$\beta_0$ denotes the expected value of the surface roughness when s = f = d = 0

$\beta_1$, $\beta_3$, $\beta_5$ denote the contribution of the cutting parameters on the surface roughness to be estimated

$\beta_2$, $\beta_4$, $\beta_6$ denote the contribution of the non-linear component of the cutting parameters to be estimated

$\beta_7$, $\beta_8$, $\beta_9$ denote the contribution of the interaction effect component on the surface roughness to be estimated

$\epsilon$ denotes the error in the system

## 4.1.1.2: Normality Test

Table 13 provides the Analysis of Variance (ANOVA) summary table, which is utilised to check if the data is normally distributed and to validate the existence of the relationship between all variables.

**Table 13: ANOVA summary table.**

| Source | Degrees of freedom (DF) | Sum of Squares (SS) | Adjusted Mean Squares (MS) | F – value | P – value |
|---|---|---|---|---|---|
| Model | 9 | 865754 | 96195 | 20.97 | 0.000 |
| Lack of fit | 5 | 45644 | 9129 | 207.20 | 0.000 |
| Pure error | 5 | 220 | 44 | | |
| Total | 19 | 911618 | | | |

To check the normality of the data the global F – test has to be done under the assumptions:

$H_o$: $\beta_1 = 0$      $H_1$: $\beta_1 \neq 0$, where $H_o$ is the null hypothesis and $H_1$ is the alternative hypothesis.

The decision rule for the global F – test is to reject $H_o$ if the p – value < 0.05 or fail to reject $H_o$ if the p – value ≥ 0.05. What that means is that a p – value that is less than 0.05 indicates that the data is normally distributed.

The ANOVA table indicated that the model p – value is 0.00 < 0.05, which makes it significant for prediction purposes. However, the lack of fit also has a p – value of 0.00 < 0.05, making it highly significant; a condition opposite to what is required from a model. Ideally, the lack of fit needs to have a p – value > 0.05 to make the model adequate for prediction purposes, a p – value ≥ 0.05 implies that further tests are required for the model. Table 14 below provides the un-coded estimated regression coefficients for the empirical or prediction model. The method of least squares was used to obtain the model parameters.

**Table 14: Regression model terms.**

| Term | Coefficient | Contribution | F – value | P – value | T – value |
|------|-------------|--------------|-----------|-----------|-----------|
| Constant | -31.1991 | | | | |
| s | -0.1718 | 35.91 % | 67.78 | 0.000 | -8.233 |
| f | 65.5894 | 21.44 % | 40.48 | 0.000 | 6.362 |
| d | 0.8052 | 0.0034 % | 0.01 | 0.939 | 0.079 |
| s*s | 4.8726E-5 | 17.19 % | 18.55 | 0.002 | 4.307 |
| f*f | -0.1380 | 0.0067 % | 0.01 | 0.934 | -0.084 |
| d*d | -0.0096 | 0.0015 % | 0.00 | 0.959 | -0.053 |
| s*f | -0.0175 | 25.43 % | 48.00 | 0.000 | -6.928 |
| s*d | -1.3728E-04 | 0.014 % | 0.03 | 0.873 | -0.163 |
| f*d | 0.0105 | 5.78E-04 % | 0.00 | 0.974 | 0.033 |

The coefficients displayed in Table 14, represent the empirical model as follows:

$$\widehat{SR_{ONSI-56}} = -31.1991 - 0.1718s + 65.5894f + 0.8052 + 4.8726e^{-5}s^2 - 0.1380f^2 -$$
$$0.0096d^2 - 0.0175sf - 1.372e^{-4}sd + 0.0105fd \qquad (16)$$

Performing the global, F – Test on the un-coded machining coefficients to determine which are significant for the model, shows that the speed and feed are highly significant, with their p – values < 0.05. Supporting the assumption stated in the previous section that the cutting speed and feed rate have the greatest effect on the surface roughness. The depth of cut has a p -value = 0.939 > 0.05, meaning that when it varies it does not affect the surface roughness much and including it in the model would have no significant effect. The non-linear squared speed term has a p – value = 0.002 < 0.05, making it significant. The non-linear squared feed and depth of cut terms are not significant since their p – values are greater than 0.05. The interaction term between the speed and feed is significant with a p – value = 0.00, and the interaction term between the speed and depth of cut and feed and depth of cut are not significant. Emphasis is on un-coded coefficients, as they represent the raw values used in the model and therefore provided a more accurate representation of the model.

If the surface roughness is the total 100 % of all the different terms, then cutting speed contributes more than 35 % towards the model, which is the greatest contribution of all the terms. That means 35 % of the variation in the surface roughness is attributed to the variation in the cutting speed. The T – values, indicate if there is a positive or negative influence on the response. A negative relationship between an independent variable and the dependent response means that for every increase in the independent variable, there will be a decrease in the dependent response. A positive relationship means when the independent variable increases, the dependent response also increases. The T – value indicates that the cutting speed and the interaction term between the speed and feed have a negative relationship with the surface roughness. The feed rate and the non-linear squared speed term have a positive relationship with the surface roughness.

## 4.1.1.3 Assumptions testing

Figure 42 below shows the residual plots with all terms included in the model (both significant and insignificant).
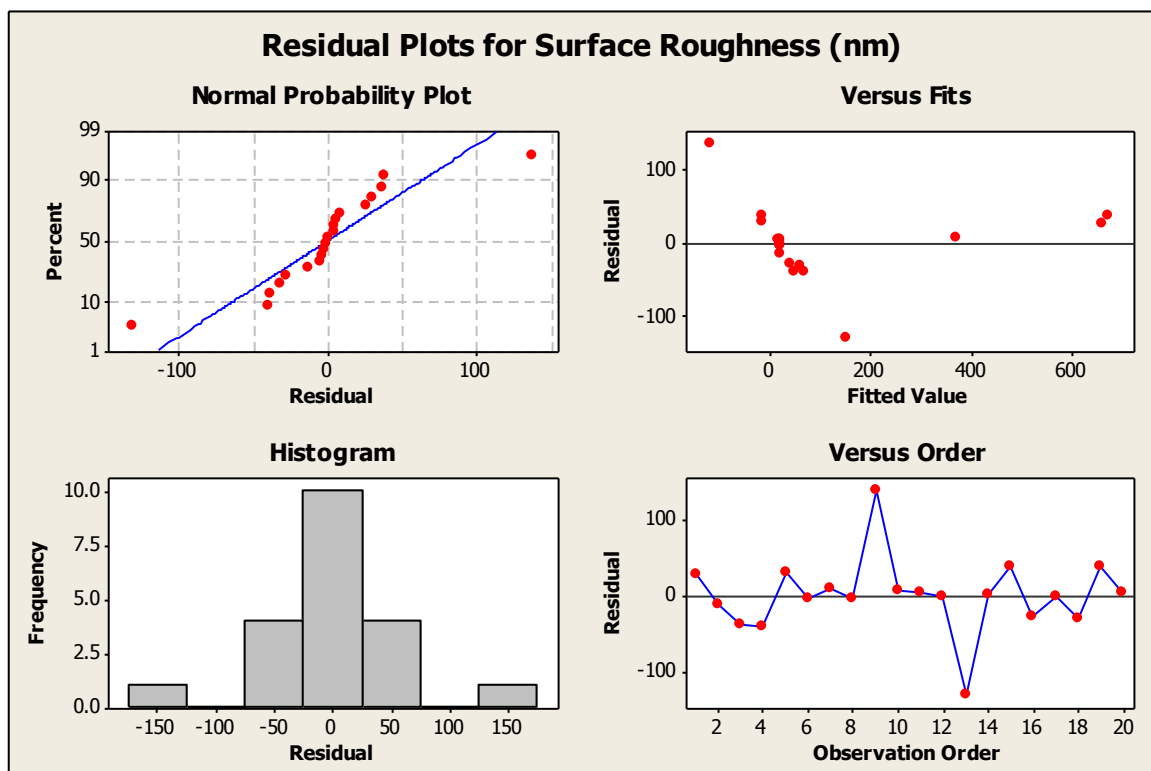


**Figure 42: Surface roughness residual plots for ONSI-56.**

91

The residual plots for the surface roughness assist in checking the goodness of fit of the model. The normal probability plot shows that the data is normally distributed, however some data points are over or under the least squares line. Two extreme points above and below the least squares line appear as outliers or unusual observations. These points are stretching the probability plot because it wants to cover all the data points. The standard procedure of dealing with the outliers would be to remove them and perform the analysis without the data points, for the purpose of this experiment the data points will not be removed because removing them might give misleading results. Although the penalty of keeping the outliers will be to have skewed results, for the purpose of this study unusual observations will not be removed. The versus fits and versus order do not follow a set pattern, however the versus order does have extreme residuals represented by the sharp peaks at the top and bottom. The histogram of observations shows the normality of the data and validates that there are unusual points in the data indicated by the gaps on the left and right hand side.

Table 15 indicates the model summary of regression. The table shows the standard error of regression (S) at 67.72 nm, which represents the average distance that the observed values fall from the least squares line. The standard error of regression assumes the units of the surface roughness of nm.

**Table 15: Regression model summary.**

| S | $R^2$ | Adjusted $R^2$ | Predicted $R^2$ |
|---|---|---|---|
| 67.72 nm | 94.97 % | 90.44 % | 60.80 % |

The error of regression is high indicating that there is a big distance between the surface roughness data points and the least squares line. The $R^2$, which gives an indication of how well the model predicts the response is high, more than 94 %. The adjusted $R^2$ which takes into account the sample size and the number of β coefficients in the model is 90.44 %, showing that the variability of the surface roughness is attributed to the cutting parameters. The predicted $R^2$ which is used to determine how well the model would predict the surface roughness for new observations is 60.80 %. It is above 50 %, however, because the model contains

insignificant terms, optimising and analysing it required to improve the predictive power of the model.

## 4.1.1.4 Optimised Surface Roughness Model

Table 16 provides the ANOVA summary table only for the un-coded significant terms in the model and will be used to check the normal distribution of the data.

**Table 16: Revised ANOVA summary for ONSI-56.**

| Source | Degrees of freedom (DF) | Sum of Squares (SS) | Adjusted Mean Squares (MS) | F – value | P – value |
|--------|-------------------------|---------------------|----------------------------|-----------|-----------|
| Model | 4 | 865528 | 216382 | 70.42 | 0.000 |
| Lack of fit | 4 | 45484 | 3073 | 205.76 | 0.000 |
| Pure error | 11 | 608 | 55 | | |
| Total | 19 | 911619 | | | |

Table 16 above shows that the model and the lack of fit are both significant, ideally the lack of fit needs to be insignificant, however the model will be completely validated before any assumptions are made. Table 17 shows the un-coded significant model coefficients.

**Table 17: Revised model coefficients for ONSI-56.**

| Term | Coefficient | Contribution | F – value | P – value | T – value |
|------|-------------|--------------|-----------|-----------|-----------|
| Constant | -23.5031 | | | | |
| s | -0.1713 | 35.91 % | 70.42 | 0.000 | -10.059 |
| f | 63.9199 | 21.45 % | 101.18 | 0.000 | 7.773 |
| s*s | 4.7795E-05 | 17.20 % | 48.44 | 0.000 | 6.960 |
| s*f | -0.01746 | 25.44 % | 71.65 | 0.000 | -8.464 |

The global F – test shows that all the terms are significant and their p – values < 0.00. When any of the coefficients change, there is a change in the surface

roughness whether it is an increase or a decrease depending on the sign of the coefficient and the T – value. The revised prediction model can be represented as follows:

$$\widehat{SR_{ONSI-56}} = -23.5031 - 0.1713s + 63.9199f + 4.7795e^{-5}s^2 - 0.01746sf \qquad (17)$$

## 4.1.1.5 Assumptions testing for the optimised model

Figure 43 shows the residual plots for only the significant terms in the model.
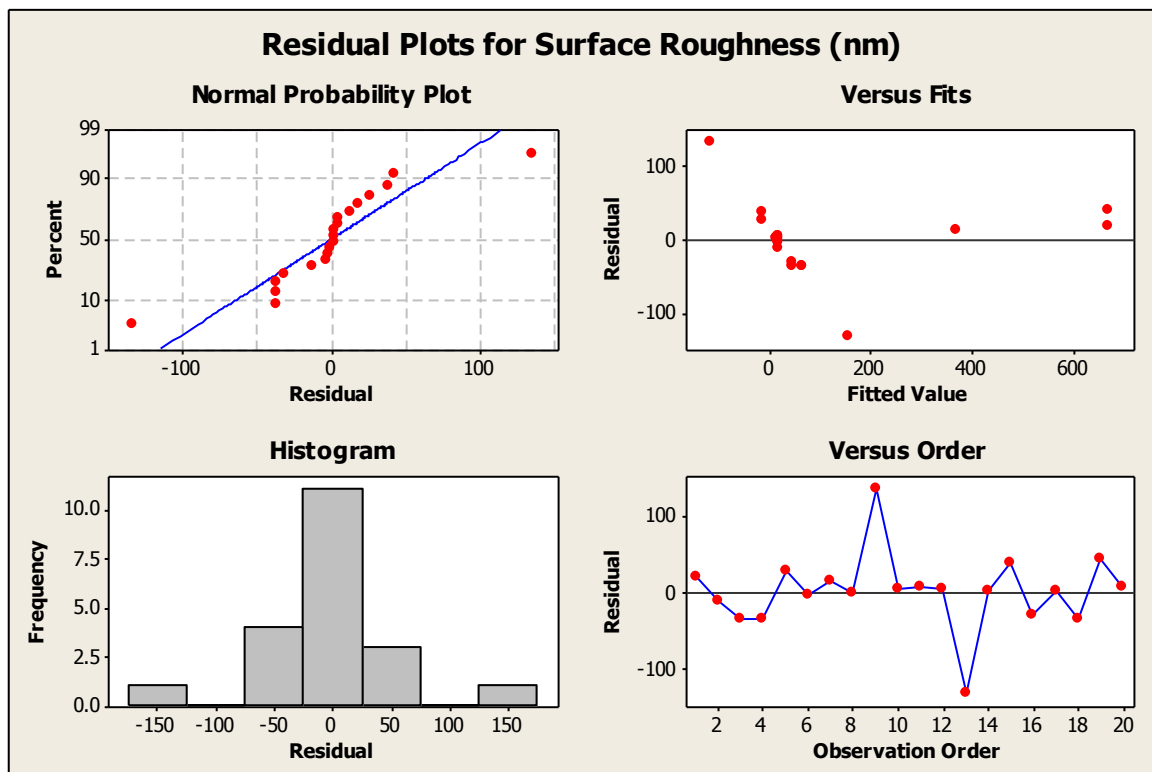


**Figure 43: Surface roughness residual plots for ONSI-56 optimised model.**

The normal probability plot clearly shows the data being pulled away from the least squares line, and being pulled towards the extreme points. There are three data points that are almost parallel with the y – axis, indicating that a single x – value represents three different y – values. One of the requirements is for the data points to have residuals independent from each other. The versus fits and versus order plots do not follow set pattern except for the indication of the extreme points. The histogram appears skewed towards the right and shows the gaps that indicate unusual data points.

## 4.1.1.6 Further Investigations on Main effects on the surface roughness

Figure 44 below displays the main effects plot showing the effect of the speed and feed on the surface roughness. The main effects plot for a model assists in examining the differences between the level means for one or more parameters affecting the response. When the main effects plot has a horizontal line parallel to the x – axes, that indicates that there is no main effect on the response, meaning the response is the same across all level factors. Alternatively, a steep slope indicates a great main effect which affect the response.
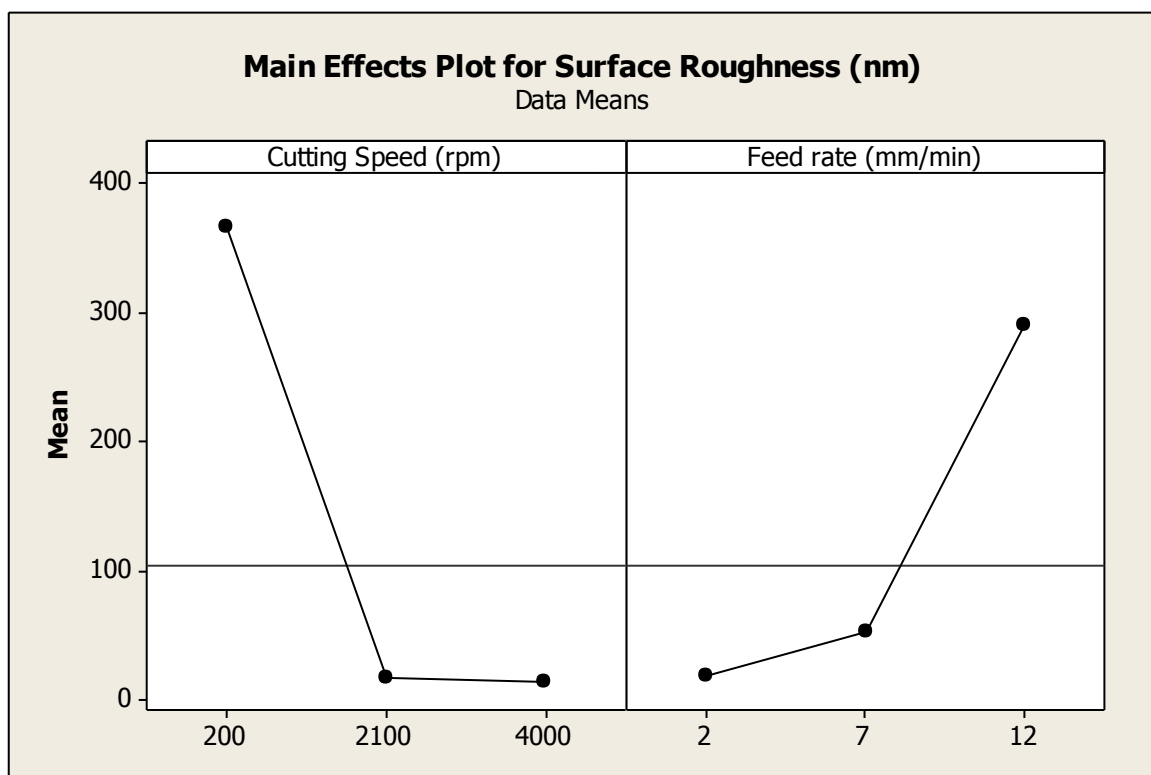


**Figure 44: Surface roughness main effects plot for ONSi-56 optimised model.**

The cutting speed has a steep slope from 200 – 2100 rpm indicating that there is a high correlation between any changes in the speed and the surface roughness. Increasing the speed from 2100 – 4000 rpm does not influence the surface roughness much as the line is almost parallel to the x – axis. The negative effect of the speed on the surface roughness clearly shows on how the means drop when the speed increases.

The slope of the feed rate from 2 – 7 mm/min is not too high as compared to the steep slope between 7 – 12 mm/min, however the change in the increase in the feed rate and the change in the increase in the surface roughness is evident indicating a high positive correlation between the feed rate and the surface roughness.

## 4.1.1.7 Interaction effects on the surface roughness

Figure 45 below indicates the interaction effects on the surface roughness. Keeping the cutting speed constant at 200 rpm and varying the feed rate from 2 – 12 mm/min gives a steep slope that indicates that the surface roughness rises sharply and is not optical quality. Keeping the cutting speed constant at 2100 or 4000 rpm and varying the feed rate does not influence the surface roughness much; the plots over lap and are horizontal to the x – axis. A cutting speed of 2000/4000 rpm and a feed rate of 2 or 12 mm/min, will give a surface roughness that is almost the same.
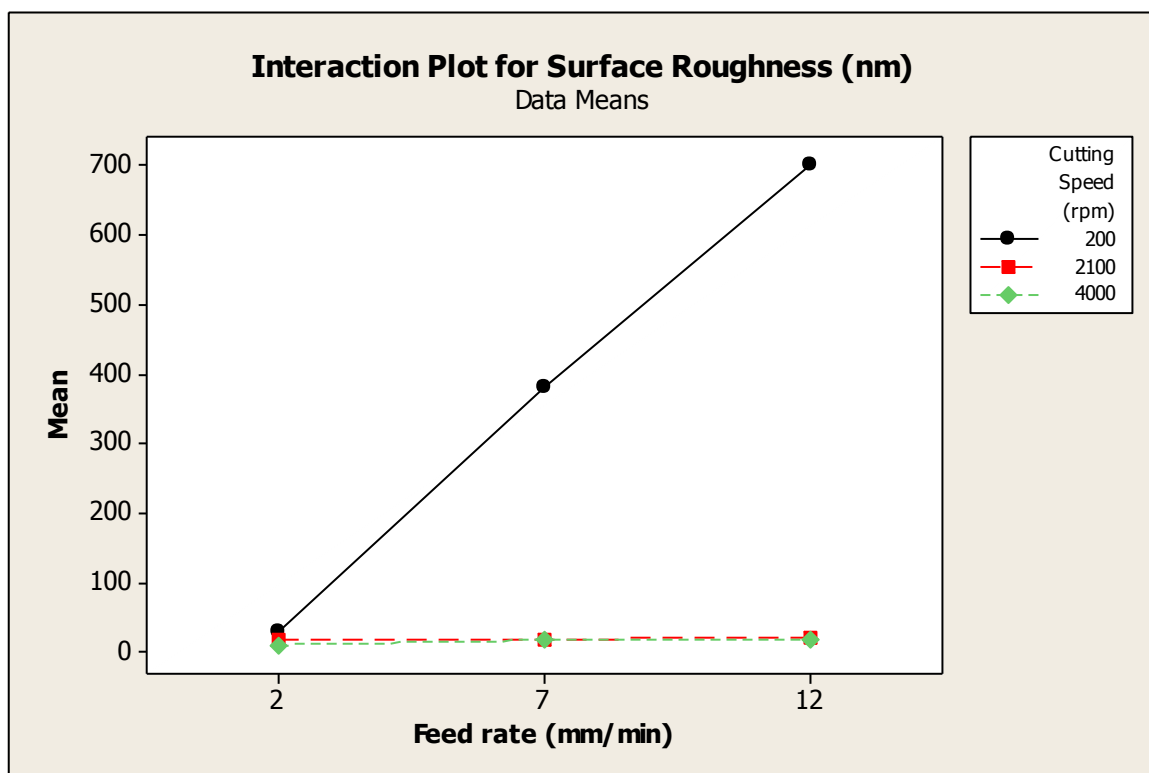


**Figure 45: Surface roughness interaction plot for ONSI-56 optimised model.**

## 4.1.1.8 Contour and Surface plots

Figure 46 shows the contour plot for the surface roughness against the feed and speed.
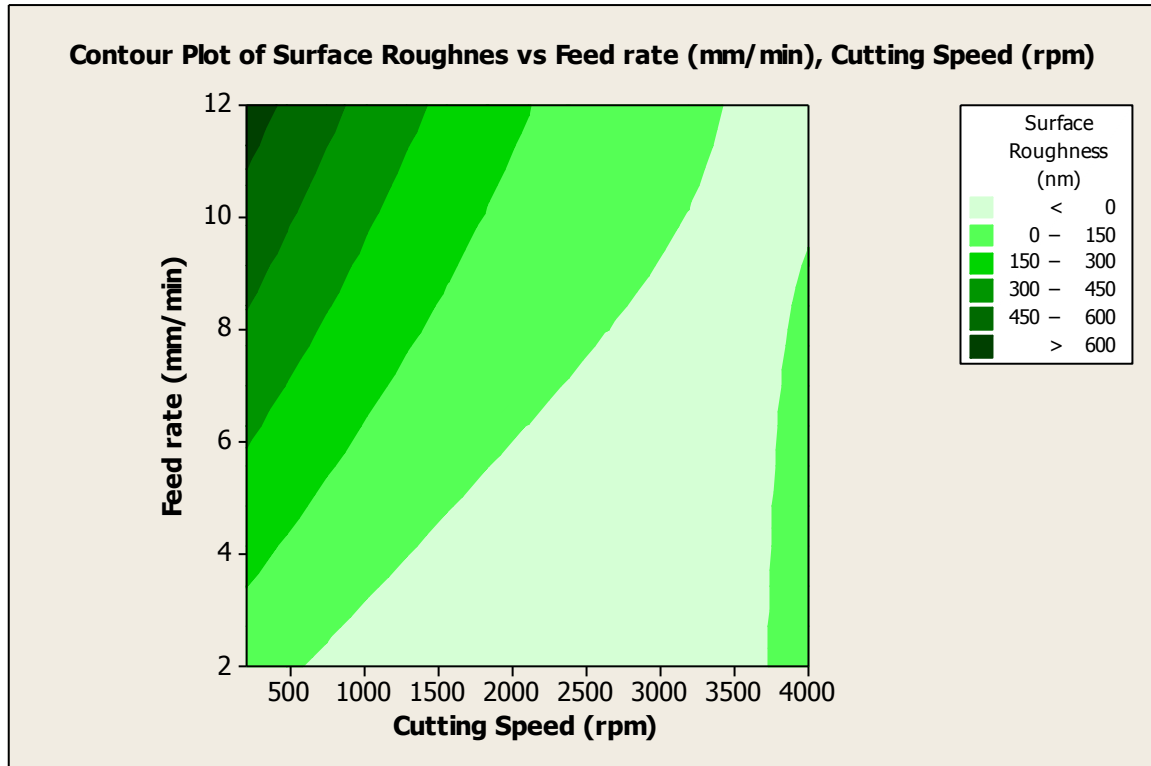


**Figure 46: Contour plot for ONSI-56 optimised model.**

The contour plot shows an optimal region just above 500 to about 3700 rpm cutting speed (light green region). Keeping the cutting speed constant at 3500 rpm and varying the feed rate between 2 – 12 mm/min, still produces an optimal surface roughness because it falls within the light green region. That validates the interaction effects plot that showed no effect on different level of the feed rate for a cutting speed between 2100 – 4000 rpm.

Figure 47 shows the surface plot for the surface roughness against the speed and feed.
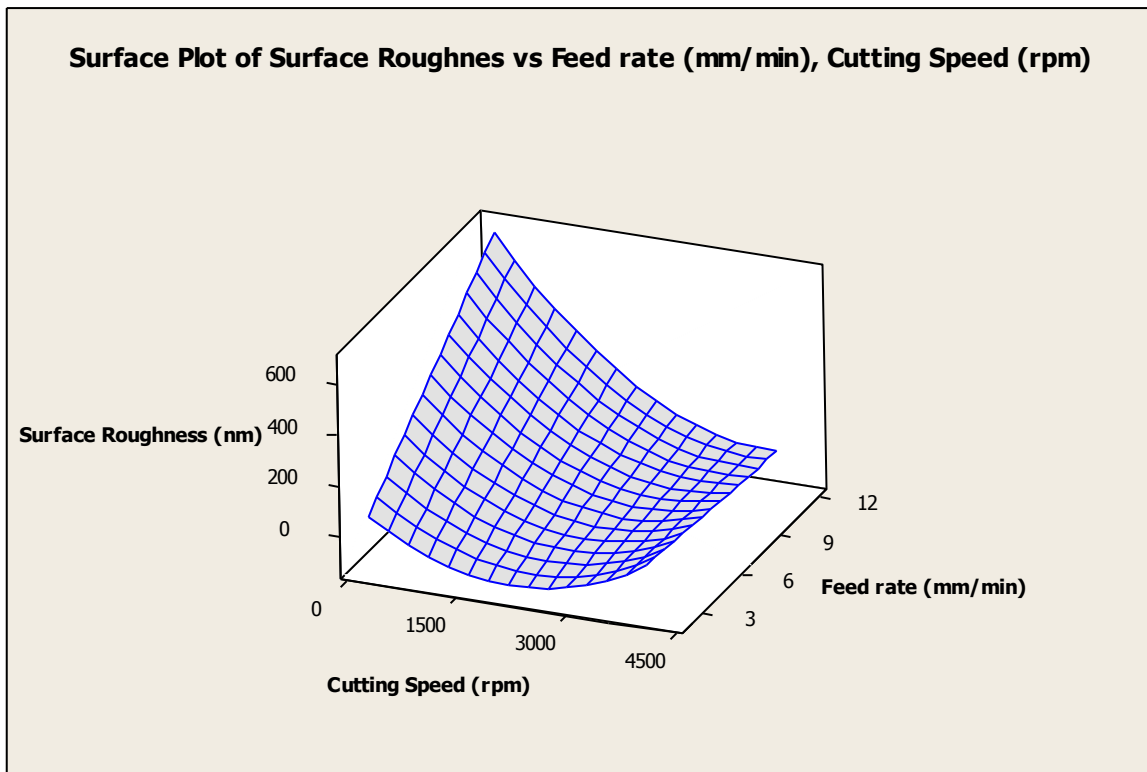
**Figure 47: Surface plot for ONSI-56 optimised model.**

A sharp peak on the surface roughness is shown due to low cutting speed and a high cutting feed. Following the peak down shows the surface roughness reducing (becoming better) as the cutting speed increases, as observed from the contour plot.

## 4.1.1.9 Model summary

Table 18 displays the model summary of regression with the error of regression 55.43, which slightly decreased but is still substantially high.

**Table 18: Revised regression model summary.**

| S | $R^2$ | Adjusted $R^2$ | Predicted $R^2$ |
|---|---|---|---|
| 55.43 | 94.94 % | 93.60 % | 90.59 % |

The $R^2$ = 94.94 % which has increased and is high enough to predict for new observations for the model. Taking into account the sample size and the number of $\beta$ coefficients in the model, the adjusted $R^2$ shows that more than 93 % of the variation in the surface roughness can be attributed to the variation in the cutting speed and the feed rate. The predicted $R^2$ = 90.59 % which is not higher than $R^2$ shows that the

model does not over fit and can predict for new observations not included in the calculations.

Even though the model is highly significant and can predict for observations not included during its calculation, it has a constant β value that is negative, indicating that outliers exist and are influencing the response. The outliers are extreme points, which are included to show the true response. It also failed the normality test by having an x – value that had three different y – values deviating away from the assumption of independency of observations. The model has a considerably high error of regression, more than 50 nm from the least squares line, indicating that there is a considerable gap between the actual observations and the predicted observations. The brittle nature of the material and the low cutting speed used during the experiment could have affected the results. The cutting speed minimum needs to be increased in order to improve the surface roughness and thus the one used is not suitable for the experiment.

Table 19 displays the original surface roughness and the predicted surface roughness.

**Table 19: Predicted surface roughness measurements.**

| Run Order | Cutting Speed (rpm) | Feed rate (mm/min) | Depth of Cut (µm) | Surface Roughness (nm) | Predicted Surface Roughness (nm) |
|---|---|---|---|---|---|
| 1 | 200 | 12 | 10 | 687.7 | 669.3 |
| 2 | 2100 | 7 | 25 | 6.0 | 18.3 |
| 3 | 4000 | 2 | 10 | 7.3 | 44.2 |
| 4 | 200 | 2 | 40 | 28.4 | 65.0 |
| 5 | 4000 | 12 | 40 | 11.9 | -15.1 |
| 6 | 2100 | 7 | 25 | 15.0 | 18.3 |
| 7 | 200 | 7 | 25 | 380.2 | 367.1 |
| 8 | 2100 | 7 | 25 | 16.0 | 18.3 |
| 9 | 2100 | 2 | 25 | 17.6 | -117.9 |
| 10 | 2100 | 7 | 10 | 21.0 | 18.3 |

| 11 | 2100 | 7 | 25 | 23.9 | 18.3 |
| 12 | 4000 | 7 | 25 | 17.1 | 14.5 |
| 13 | 2100 | 12 | 25 | 21.0 | 154.5 |
| 14 | 2100 | 7 | 40 | 20.2 | 18.3 |
| 15 | 4000 | 12 | 10 | 23.8 | -15.1 |
| 16 | 4000 | 2 | 40 | 12.4 | 44.1 |
| 17 | 2100 | 7 | 25 | 18.4 | 18.3 |
| 18 | 200 | 2 | 10 | 27.8 | 65.0 |
| 19 | 200 | 12 | 40 | 711.6 | 669.3 |
| 20 | 2100 | 7 | 25 | 23.7 | 18.3 |

## 4.1.2 Surface Roughness Measurements for PMMA contact lens button.

The second set of experiments was carried out using PMMA, a hydrophobic contact lens button with 12.7 mm diameter. The experiments were performed three times and each time a surface roughness measurement was taken using the Taylor Hobson PGI profilometer. That was done for repeatability and the average surface roughness was computed and utilised.

Table 20 below shows the machining parameters together with the surface roughness measurements.

**Table 20: Surface roughness measurements for PMMA.**

| Run Order | Cutting Speed (rpm) | Feed rate (mm/min) | Depth of Cut (μm) | Surface Roughness (nm) |
|---|---|---|---|---|
| 1 | 200 | 12 | 10 | 141.3 |
| 2 | 2100 | 7 | 25 | 24.9 |
| 3 | 4000 | 2 | 10 | 4.8 |
| 4 | 200 | 2 | 40 | 57.3 |
| 5 | 4000 | 12 | 40 | 10.4 |
| 6 | 2100 | 7 | 25 | 27.1 |

| 7 | 200 | 7 | 25 | 80.6 |
| 8 | 2100 | 7 | 25 | 23.2 |
| 9 | 2100 | 2 | 25 | 27.9 |
| 10 | 2100 | 7 | 10 | 21.1 |
| 11 | 2100 | 7 | 25 | 26.1 |
| 12 | 4000 | 7 | 25 | 8.8 |
| 13 | 2100 | 12 | 25 | 31.4 |
| 14 | 2100 | 7 | 40 | 26.4 |
| 15 | 4000 | 12 | 10 | 9.6 |
| 16 | 4000 | 2 | 40 | 6.7 |
| 17 | 2100 | 7 | 25 | 24.0 |
| 18 | 200 | 2 | 10 | 51.8 |
| 19 | 200 | 12 | 40 | 203.2 |
| 20 | 2100 | 7 | 25 | 22.9 |

The measured surface roughness varied from a minimum value of 4.8 nm to a maximum value of 203.2 nm over a range of 198.4 nm. That was an indication of the diversity in the experimental observations, over the various machining parameter combinations. Figure 48 displays a scatterplot of the experimental combinations.
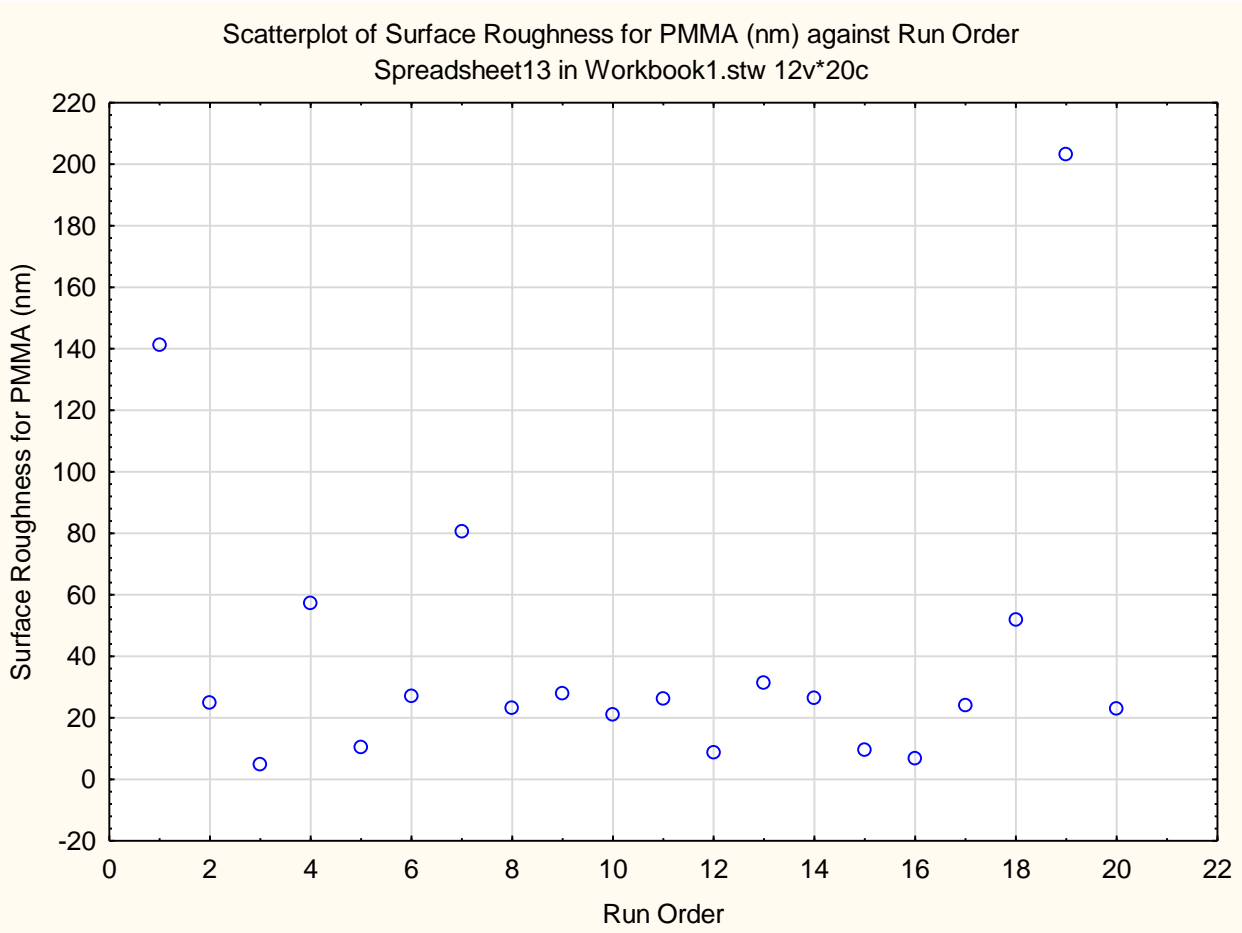
**Figure 48: Scatter plot of surface roughness observations for PMMA.**

The surface roughness values were grouped into good, moderate and bad, according to the size of the measured surface roughness, to be able to simplify the information. Table 21 shows the different groups of surface roughness measurements.

**Table 21: Surface roughness groups.**

| Run Order | Range | Category |
|---|---|---|
| 3, 5, 12, 15, 16 | 0 nm – 19.9 nm | Good |
| 2, 6, 8, 9, 10, 11, 13, 14, 17, 20 | 20 nm – 39.9 nm | Moderate |
| 1, 4, 7, 18, 19 | 40 nm – 204.9 nm | Run Order |

The majority of good and moderate surface roughness observations was obtained with a cutting speed between 2100 – 4000 rpm and a feed rate between 2 – 7 mm/min and a depth of cut over the entire cutting range. The bad surface roughness

was obtained with a speed of 200 rpm and a feed rate between 7 – 12 mm/min, leading to the assumption that a low cutting speed and high feed rate lead to poor surface finish. The surface roughness profile obtained from the Taylor Hobson PGI profilometer with a good surface roughness of 4.8 nm obtained from observation 3 is shown in Figure 49 below.
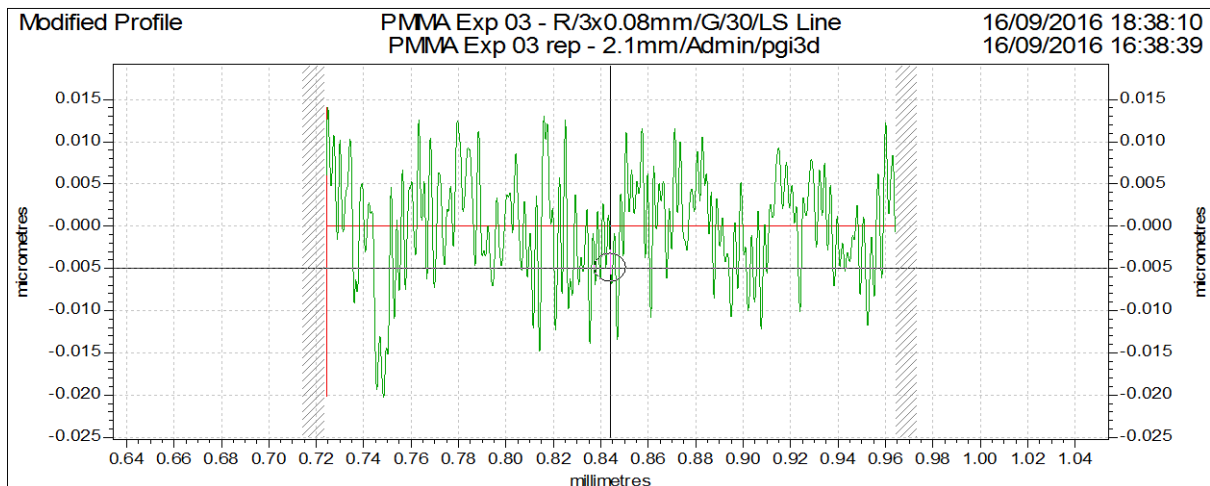


**Figure 49: Surface profile for experimental observation 3.**

The surface roughness was obtained with a cutting speed of 4000 rpm, a feed rate of 2 mm/min and a depth of cut of 10 $\mu$m. The profile showed that no tool marks translated onto the workpiece surface since optical finish was obtained. On the contrary, Figure 50 shows a surface profile of a bad surface roughness obtained from experiment 1 with 141.3 nm, obtained with a cutting speed of 200 rpm, a feed rate of 12 mm/min and a depth of cut of 10 $\mu$m.
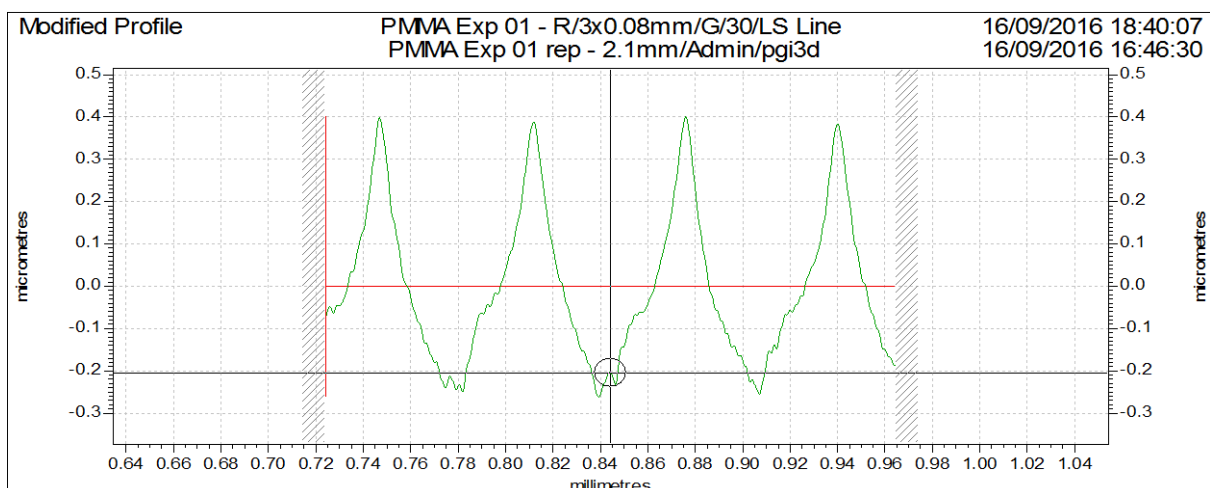


**Figure 50: Surface profile for experimental observation 1.**

The profile showed that tool marks translated onto the workpiece surface leading to bad quality. The good surface profile had a combination of high cutting speed and low feed rate, and the bad surface profile had a low cutting speed and high feed rate and the depth of cut was held constant. Both surface profiles lead to the assumption that cutting speed and feed rate greatly influenced surface roughness, but it was not easily conclusive how the depth of cut affected the surface roughness because on both experiments it was 10 μm. The assumption that cutting speed and feed rate affect the surface roughness supports the findings of Jagtap and Goel et al. when they concluded that cutting speed and feed rate influenced the surface roughness, during diamond turning of PMMA (Jagtap and Pawade (2014), Goel et al. (2016)).

## 4.1.2.1: Response Surface Modelling for PMMA

Having shown that there exists a relationship between the cutting parameters and the surface roughness; the probabilistic model can be represented as follows:

$$SR_{PMMA} = \beta_0 + \beta_1 s + \beta_2 s^2 + \beta_3 f + \beta_4 f^2 + \beta_5 d + \beta_6 d^2 + \beta_7 sf + \beta_8 sd + \beta_9 fd + \varepsilon \qquad (18)$$

Where:

$SR_{PMMA}$ denotes the surface roughness of PMMA, measured in nano-meters

s denotes the cutting speed, in revolutions per minute (rpm)

f denotes the feed rate, in millimetres per minute (mm/min)

d denotes the depth of cut, in micrometres (μm)

$s^2$, $f^2$, $d^2$ denote the non-linear component of the cutting parameters

sf, sd, fd denote the interaction effects of the cutting parameters on the surface roughness

$\beta_0$ denotes the expected value of the surface roughness when s = f = d = 0

$\beta_1$, $\beta_3$, $\beta_5$ denote the contribution of the cutting parameters on the surface roughness to be estimated

$\beta_2$, $\beta_4$, $\beta_6$ denote the contribution of the non-linear component of the cutting parameters to be estimated

$\beta_7$, $\beta_8$, $\beta_9$ denote the contribution of the interaction effect component on the surface roughness to be estimated

$\epsilon$ denotes the error in the system

### 4.1.2.2: Normality Test

Table 22 provides the Analysis of Variance (ANOVA) summary table, which will be used to check if the data is normally distributed and to validate the existence of a relationship between the dependent independent variables.

Table 22: ANOVA summary for PMMA.

| Source | Degrees of freedom (DF) | Sum of Squares (SS) | Adjusted Mean Squares (MS) | F – value | P – value |
|---|---|---|---|---|---|
| Model | 9 | 43921.1 | 4880.12 | 20.95 | 0.000 |
| Lack of fit | 5 | 2316.1 | 463.22 | 168.57 | 0.000 |
| Pure error | 5 | 13.7 | 2.75 | | |
| Total | 19 | 46250.9 | | | |

To check the normality of the data the global F – test needs to be performed under the assumption that:

$H_o$: $\beta_1 = 0$     $H_1$: $\beta_1 \neq 0$, where $H_o$ is the null hypothesis and $H_1$ is the alternative hypothesis.

The decision rule for the global F – test is to reject $H_o$ if the p – value < 0.05 or fail to reject $H_o$ if the p – value ≥ 0.05. What that means is that a p – value that is less than 0.05 indicates that the data is normally distributed.

The ANOVA table indicates that the model p – value is 0.00 < 0.05, which makes it significant for prediction purposes. The lack of fit also has a p – value of 0.00 < 0.05. Ideally, the lack of fit needs to have a p – value > 0.05 to make the model adequate for prediction purposes, therefore further tests needs to be performed.

Table 23 below provides the estimated regression un-coded coefficients for the empirical or prediction model. Model parameters are obtained using the method of least squares.

**Table 23: Regression model coefficients for PMMA.**

| Term | Coefficient | Contribution | F – value | P – value | T – value |
|------|-------------|--------------|-----------|-----------|-----------|
| Constant | 45.0 | | | | |
| s | -0.0264 | 55.54 % | 4.37 | 0.063 | -2.090 |
| f | 3.68 | 13.94 % | 0.42 | 0.531 | 0.649 |
| d | -0.281 | 1.28 % | 0.02 | 0.899 | -0.130 |
| s*s | 0.00001 | 11.64 % | 7.02 | 0.024 | 2.650 |
| f*f | 0.374 | 0.82 % | 1.03 | 0.334 | 1.015 |
| d*d | 0.0146 | 0.07 % | 0.13 | 0.728 | 0.358 |
| s*f | -0.003 | 14.65 % | 27.62 | 0.000 | -5.256 |
| s*d | -0.0003 | 1.19 % | 2.25 | 0.165 | -1.499 |
| f*d | 0.0922 | 0.87 % | 1.64 | 0.229 | 1.281 |

From the coefficients on the above table, the empirical model can be represented as follows:

$$\widehat{SR_{PMMA}} = 45 - 0.0264s + 3.68f - 0.281d + 0.00001s^2 + 0.374f^2 + 0.0146d^2 - 0.003sf - 0.0003sd + 0.0922fd \tag{19}$$

The global F – test needs to be performed on the coefficients to assist in removing insignificant terms. Table 23 displays that all the cutting parameters (s, f, d) have p – values > 0.05, making all terms insignificant for predicting the surface roughness. However, the squared non-linear speed term and the interaction term between the speed and feed are significant with p – values < 0.05. That means even though the speed and feed seem to be insignificant in the model, when the terms are reduced for optimisation they will need to be included in the optimisation because the interaction and squared term cannot exist without including the main factors in the optimisation model. The depth of cut is definitely insignificant in the model, its squared term and the interaction terms show no significance.

The negative sign on the T – value of the coefficient indicates that when the parameter increases the surface roughness decreases, and a positive sign indicates that when the coefficient increases the surface roughness also increases. The speed and squared non-linear term have a positive influence on the surface roughness. The feed and interaction term between the speed and feed have a positive relationship. The cutting speed contributes more than 50 % towards the variation in the surface roughness, followed by the interaction term between the speed and feed, the feed rate and then the squared speed term.

## 4.1.2.3 Assumptions testing

Figure 51 below shows the residual plots with all terms included in the model (both significant and nonsignificant).
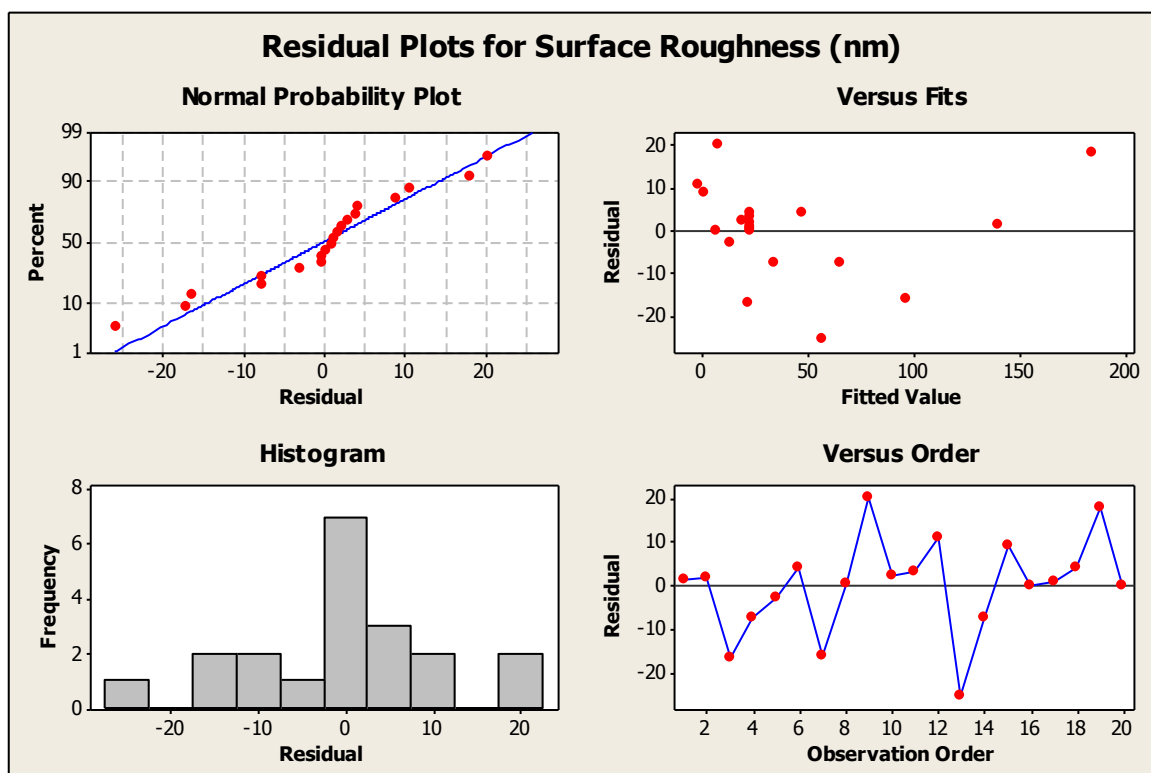


**Figure 51: Surface roughness residual plots for PMMA.**

The residual plots for the surface roughness assist in checking the goodness of fit of the model. The normal probability plot shows normality of the data. The data is slightly skewed or stretched towards the extreme observation points, leading to some data being under-estimated and some over-estimated. Under-estimated data

is data below the least squares line and data that is over-estimated is data above the least squares line. The versus fits and versus order do not follow set patterns even though the versus order has a sharp negative residual on the 13th observation, also indicating that the data contains outliers. The histogram of observations shows skewness towards the right. Outliers are indicated by the gaps in the histogram. An ideal situation would be to remove the outliers before continuing with optimisation of the model, however, removing the observations will not reflect the true nature of the performed experiment, which may lead to misrepresentation of the effects. For the purpose of this study no unusual observations will be removed.

Table 24 indicates the model summary of regression.

**Table 24: Regression model summary for PMMA.**

| S | $R^2$ | Adjusted $R^2$ | Predicted $R^2$ |
|---|---|---|---|
| 15.26 nm | 94.96 % | 90.43 % | 47.63 % |

The table shows the standard error of regression (S) at 15.26, which represents the average distance that the observed values fall from the least squares line, and it is not too high. The $R^2$ = 94.96 %, is reasonably high and indicates that the model could be able to predict the response. The adjusted $R^2$ takes into account the size of the sample and the number of β coefficients in the model. The $R^2$ = 90.43 %, that indicates that 90.43 % of the variation in the surface roughness can be attributed to the machining parameters. The predicted $R^2$ is used to determine how well the model would predict the surface roughness for new responses and in this model it is 47.63 %. Even though the $R^2$ and adjusted $R^2$ are above 90 %, a predicted $R^2$ that is below 50% infers that this model does not have great predictive capability and needs further analysis to improve it. That could also be due to the inclusion of insignificant terms in the model.

## 4.1.2.3 Optimised Surface Roughness Model

Table 25 provides the ANOVA summary table only for the significant terms in the model and will be used to check the normal distribution of the data.

**Table 25: Revised ANOVA summary for PMMA.**

| Source | Degrees of freedom (DF) | Sum of Squares (SS) | Adjusted Mean Squares (MS) | F – value | P – value |
|--------|-------------------------|---------------------|---------------------------|-----------|-----------|
| Model | 4 | 41961 | 10490.1 | 37.32 | 0.000 |
| Lack of fit | 4 | 2221 | 555.1 | 3.06 | 0.064 |
| Pure error | 11 | 1996 | 181.5 | | |
| Total | 19 | 46177 | | | |

Table 25 above shows that the model is significant with a p – value of 0.00. The lack of fit has a p – value of 0.064, making it insignificant, the required situation. As compared to the initial model, an evident improvement is the insignificant lack of fit. Reducing the model to the significant coefficients has improved it. Table 26 below shows the un-coded model coefficients for the optimised model.

**Table 26: Revised regression model coefficients for PMMA.**

| Term | Coefficient | Contribution | F – value | P – value | T – value |
|------|-------------|--------------|-----------|-----------|-----------|
| Constant | 38.05 | | | | |
| s | -0.0411 | 57.08 % | 16.43 | 0.001 | -4.053 |
| f | 11.43 | 15.12 % | 45.99 | 0.000 | 6.782 |
| s*s | 0.00001 | 11.85 % | 17.68 | 0.001 | 4.205 |
| s*f | -0.003 | 15.95 % | 23.81 | 0.000 | -4.880 |

The global F – test shows that all the terms are significant and their p – values < 0.00. When any of the coefficients change (except the constant), there is a change in the surface roughness whether it is an increase or a decrease depending on the sign of the coefficient or of the T – value. The constant term represents $\beta_0$ coefficient, which represents the surface roughness should s = f = d = 0. The revised prediction model can be represented as follows:

$$\widehat{SR_{PMMA}} = 38.05 - 0.0411s + 11.43f + 0.00001s^2 - 0.003sf \qquad (20)$$

## 4.1.2.4 Assumptions testing for the optimised model

Figure 52 shows the residual plots for only the significant terms in the model.
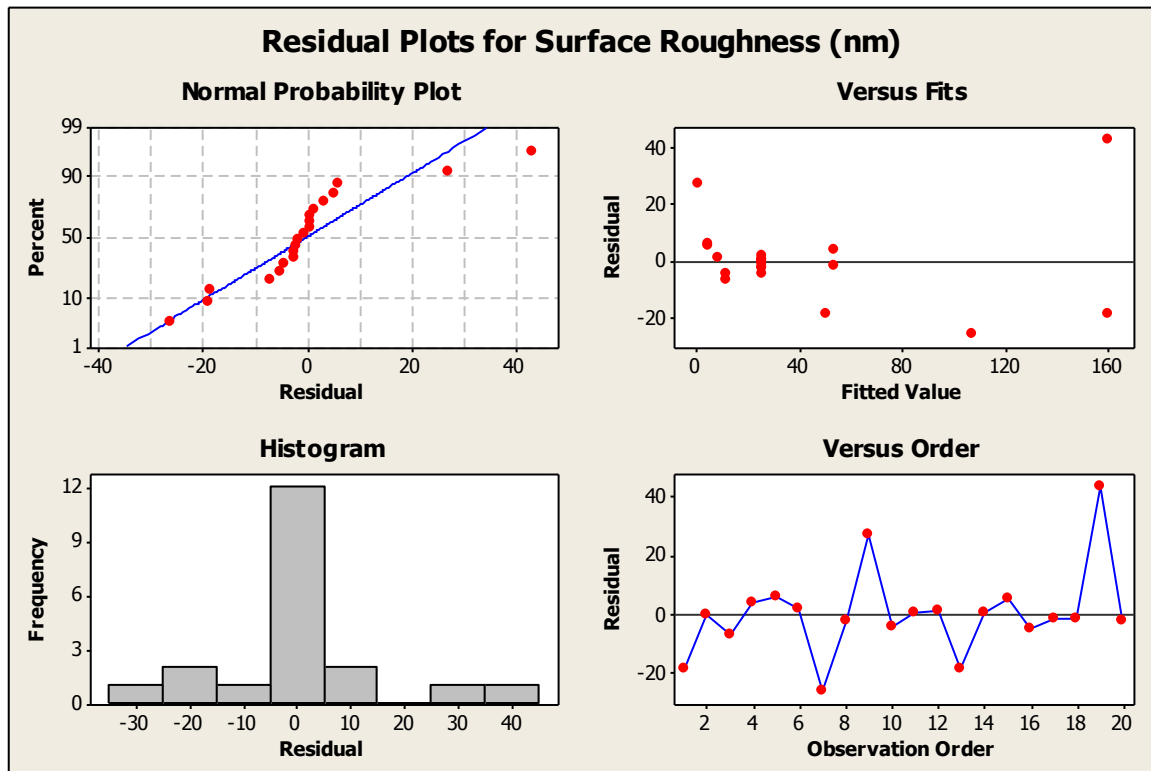


**Figure 52: Surface roughness residual plots for PMMA optimised model.**

With less terms in the model the normal probability plot clearly shows that the least squares line is being pulled towards the unusual observations. That is a normal behaviour for data points that contains extreme data points, it does not necessarily mean that the data is not normally distributed. The distribution is a true representation of the experiments which shows some values being over or under estimated and some falling on the least squares line. The versus fits and versus order does not follow a set pattern, even though sharp points indicate the presence of unusual data. The sharp points of the residuals occur in observations 7, 13 for negative residuals and 9, 19 for positive residuals. The histogram shows a normal distribution and a gap that validates the extreme points existing in the data.

## 4.1.2.5 Further Investigations on Main effects on the surface roughness

Figure 53 below displays the main effects plot showing the effect of the speed and feed on the surface roughness.
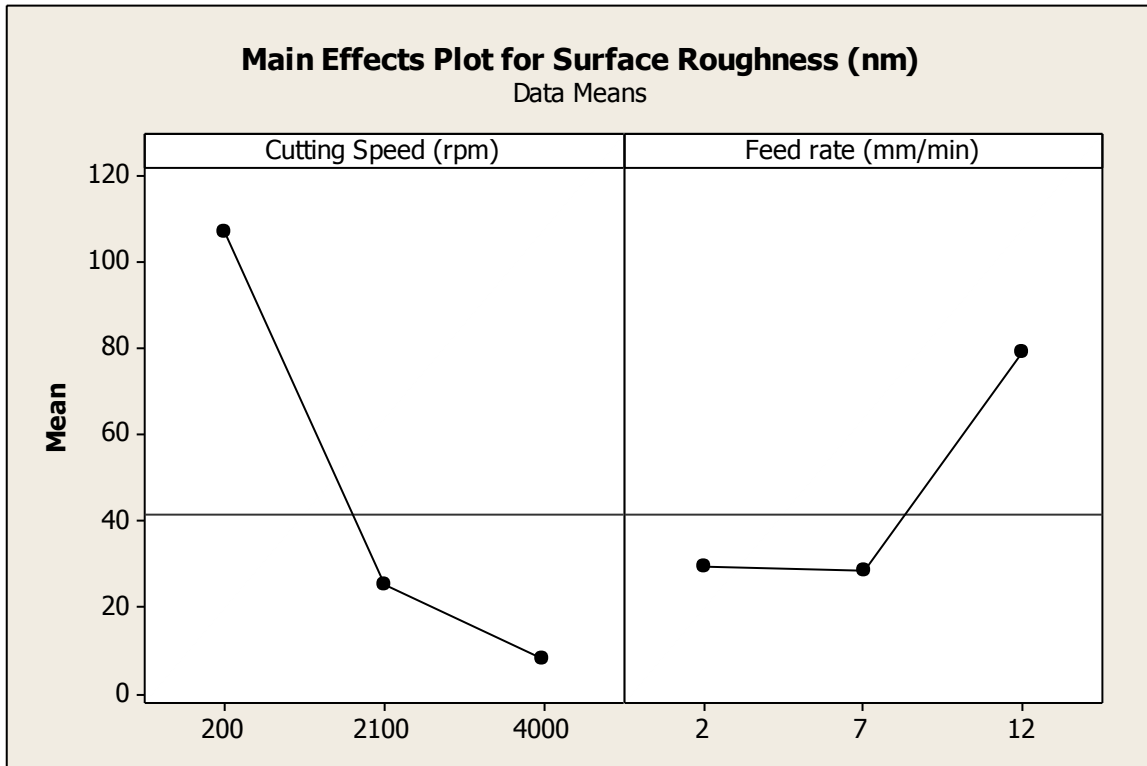
**Figure 53: Surface roughness main effects plot for PMMA optimised model.**

The main effects plot for the speed indicate a steep slope from 200 – 2100 rpm showing that there is a high correlation between the speed and the surface roughness. As the speed increases, the surface roughness decreases. When the speed further increases from 2100 – 4000 rpm, the surface roughness continues to decline. The slope of the feed rate between 2 – 7 mm/min shows a slight fall, almost parallel to the x – axis, indicating that surface roughness declines by a very small fraction in that range. When the feed rate increase from 7 – 12 mm/min, there is steep incline showing a strong correlation with the surface roughness. In that range, when the feed rate increases, the surface roughness sharply increases leading a poor surface quality. The depth of cut has no significant influence on the surface roughness, hence it is not in the main effect plot.

## 4.1.2.6 Interaction effects on the surface roughness

Figure 54 below indicates the interaction effects on the surface roughness. Cutting PMMA with a low speed of 200 rpm generates a surface roughness that is rough with the tool marks translating onto the surface of the material. When the speed is

kept constant and the feed rate is varied between 2 – 12 mm/min, there is a sharp incline in the surface roughness. The worst surface roughness to be obtained is when the feed rate increases from 7 – 12 mm/min. Material removal rate is high but the spindle speed is very low indenting the material with the cutting tool marks. Keeping the speed constant at 2100 rpm and varying the feed rate from 2 – 7 mm/min, there is very minimal decrease in the surface roughness, and increasing the feed rate from 7 – 12 mm/min shows minimal increase. Almost insignificant change in the surface roughness. Applying the maximum speed and keeping it constant; and varying the feed rate from 2 – 12 mm/min shows that the surface roughness is almost the same throughout the variation, and it is low.
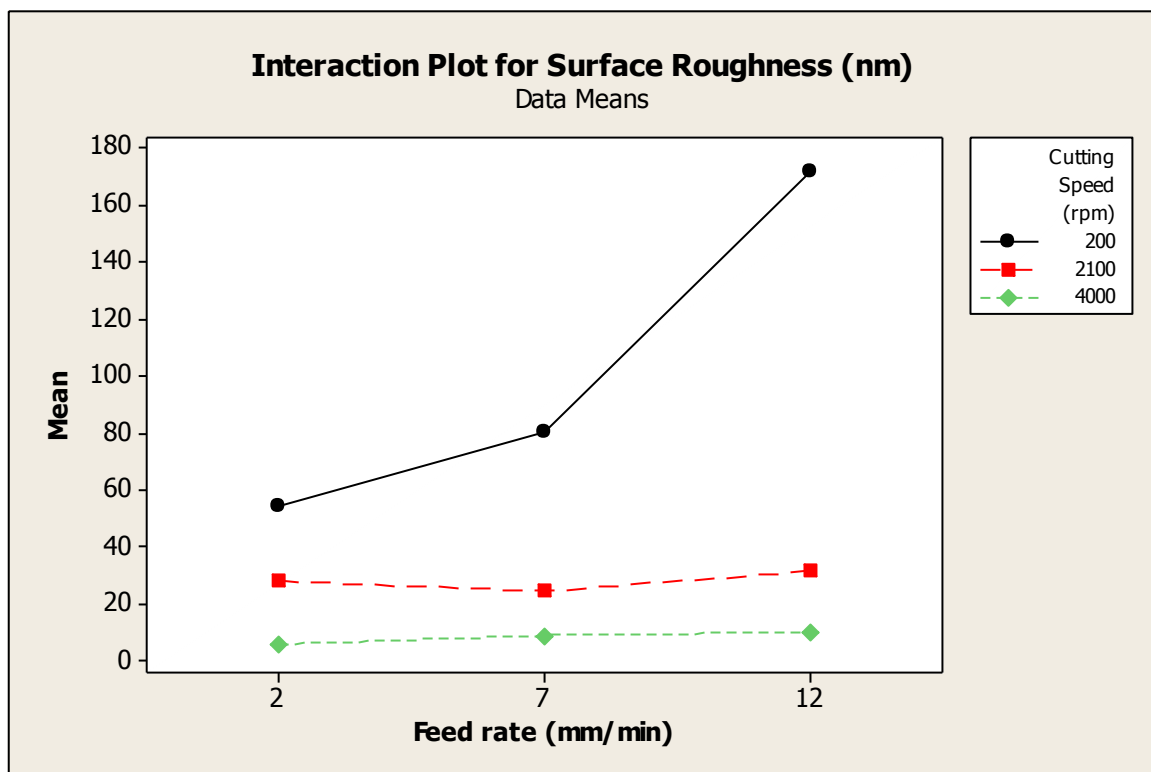


**Figure 54: Surface roughness interaction plot for PMMA optimised model.**

## 4.1.2.7 Contour and Surface plots

Figure 55 shows the contour plot for the surface roughness against the feed and speed.
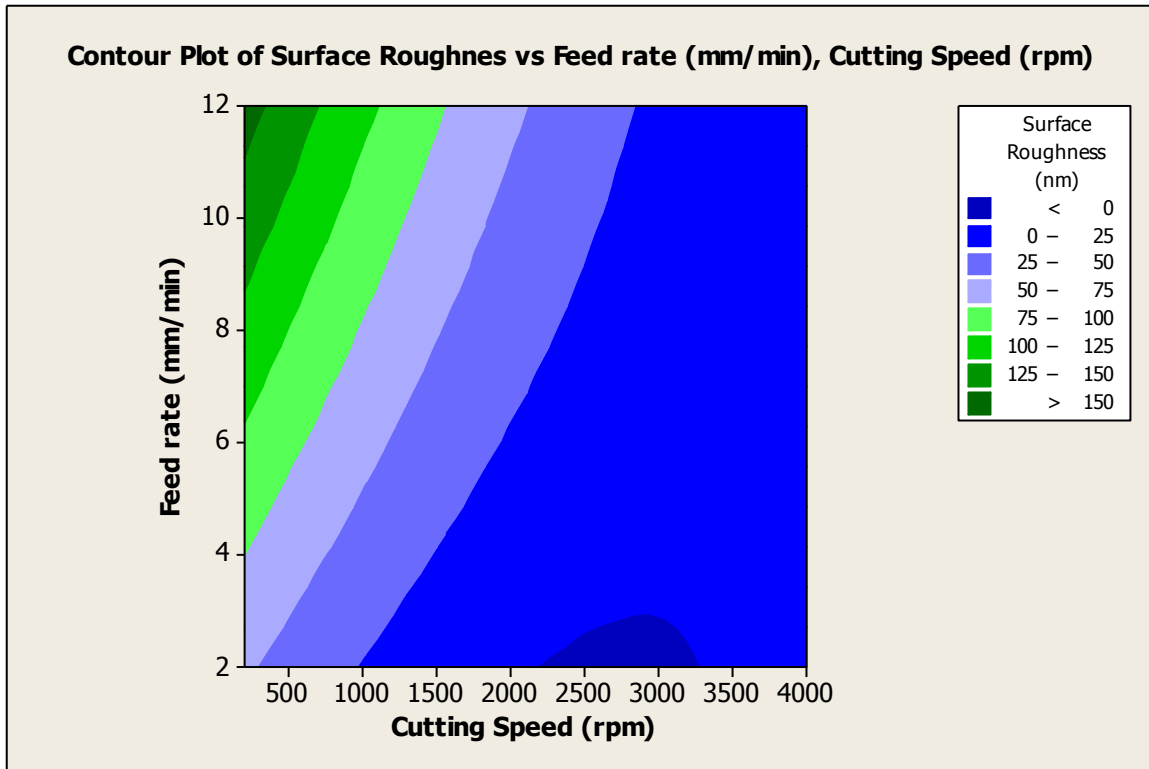
**Figure 55: Contour plot for PMMA optimised model.**

The contour plot of the surface roughness validates the inference that cutting speed and feed has an influence on the change of the surface roughness. Based on the results of the contour plot, the dark blue region would be ideal in optimising the surface roughness. The cutting conditions in that region give a surface roughness that is of optimal quality, which is the main requirement during precision machining. Utilising a feed rate between 2 – 4 mm/min and speed between the approximate range of 1750 – 3500 rpm would provide the best surface roughness.

Figure 56 shows the surface plot for the surface roughness against the speed and feed. The surface plot validates the conclusion that a low feed rate and high speed produces a minimum surface roughness. The sharp tip shown is a combination of low speed and high feed. The high speed and low combination has the best surface roughness results.
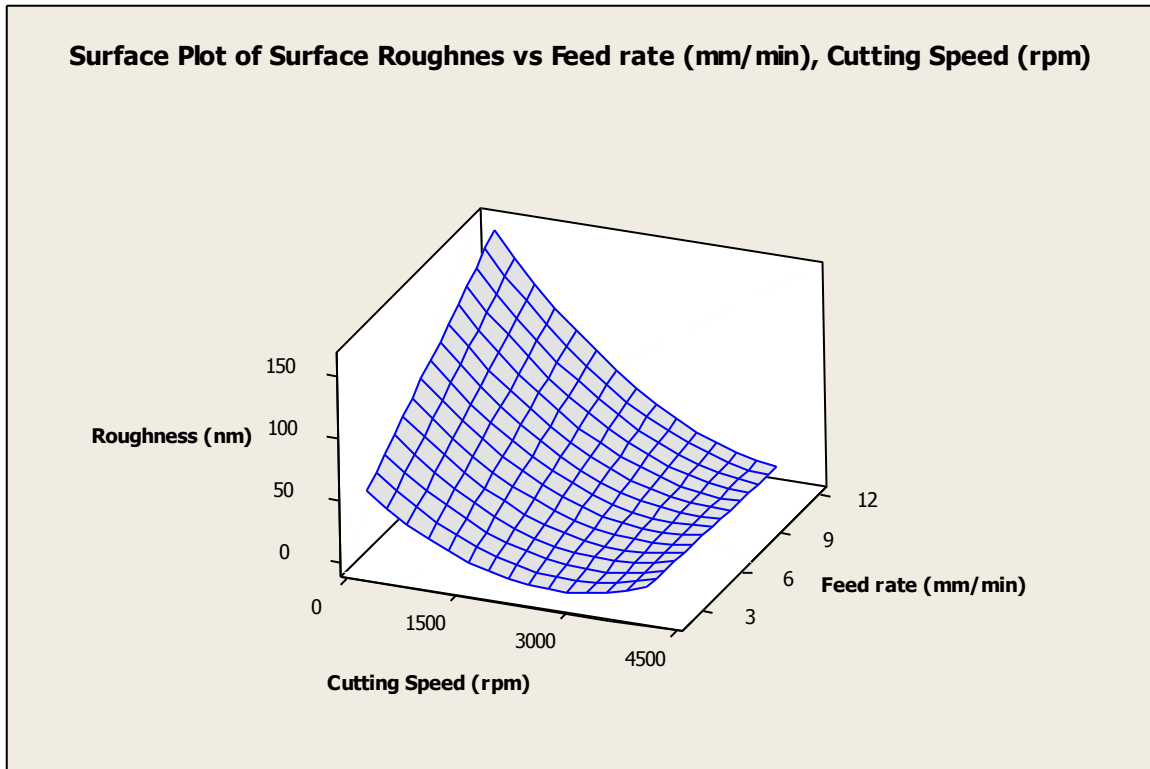
**Figure 56: Surface plot for PMMA optimised model.**

## 4.1.2.8 Model summary

Table 27 displays the model summary of regression with the error of regression 16.77, which slightly increased but is not too high. The $R^2$ = 90.87 % which has dropped from the previous 94.96 %, but is still high to predict the surface roughness for new observations.

**Table 27: Revised regression model summary for PMMA.**

| S | $R^2$ | Adjusted $R^2$ | Predicted $R^2$ |
|---|---|---|---|
| 16.77 | 90.87 % | 88.43 % | 78.15 % |

Taking into account the sample size and the number of β coefficients in the model, the adjusted $R^2$ shows that 88.43 % of the variation in the surface roughness can be attributed to the variation in the cutting speed and the feed rate. The predicted $R^2$ = 78.15 % which is not higher than $R^2$ showing that the model does not over fit and it can predict for new observations not included in the calculations. The predictive power of the optimised model has greatly improved from the previous 47.63 %. Table 28 displays the original surface roughness and the predicted surface

114

roughness. It can be concluded that modelling of single point diamond turning of PMMA is possible and that cutting speed and feed rate are the most influential parameters during machining. The model predictions are given in the table below based on Equation 20.

**Table 28: Predicted surface roughness for PMMA.**

| Run Order | Cutting Speed (rpm) | Feed rate (mm/min) | Depth of Cut (µm) | Surface Roughness (nm) | Predicted Surface Roughness (nm) |
|---|---|---|---|---|---|
| 1 | 200 | 12 | 10 | 141.3 | 159.9 |
| 2 | 2100 | 7 | 25 | 24.9 | 25.5 |
| 3 | 4000 | 2 | 10 | 4.8 | 11.7 |
| 4 | 200 | 2 | 40 | 57.3 | 53.4 |
| 5 | 4000 | 12 | 40 | 10.4 | 4.4 |
| 6 | 2100 | 7 | 25 | 27.1 | 25.5 |
| 7 | 200 | 7 | 25 | 80.6 | 106.8 |
| 8 | 2100 | 7 | 25 | 23.2 | 25.5 |
| 9 | 2100 | 2 | 25 | 27.9 | 0.7 |
| 10 | 2100 | 7 | 10 | 21.1 | 25.5 |
| 11 | 2100 | 7 | 25 | 26.1 | 25.4 |
| 12 | 4000 | 7 | 25 | 8.8 | 8.1 |
| 13 | 2100 | 12 | 25 | 31.4 | 50.2 |
| 14 | 2100 | 7 | 40 | 26.4 | 25.5 |
| 15 | 4000 | 12 | 10 | 9.6 | 4.4 |
| 16 | 4000 | 2 | 40 | 6.7 | 11.7 |
| 17 | 2100 | 7 | 25 | 24.0 | 25.5 |
| 18 | 200 | 2 | 10 | 51.8 | 53.4 |
| 19 | 200 | 12 | 40 | 203.2 | 159.9 |
| 20 | 2100 | 7 | 25 | 22.9 | 25.5 |

# 4.2 Electrostatic discharge modelling (ESD)

This section will provide a detailed analysis for the development of an electrostatic discharge (ESD) model during single point diamond turning of ONSI – 56 and PMMA respectively. Both these materials are used during contact lens making, one for producing rigid gas permeable and the other hard respectively.

## 4.2.1 Electrostatic discharge observations for ONSI – 56

The ESD measurements were obtained using data acquisition by means of a LabView software package as explained in the previous experimental chapter. The average ESD measurement was computed and utilised in developing the model. Table 29 shows the experimental observations for ONSI – 56 contact lens polymer.

Table 29: Electrostatic discharge measurements for ONSI-56.

| Run Order | Cutting Speed (rpm) | Feed rate (mm/min) | Depth of Cut (µm) | Electrostatic discharge (kV) |
|---|---|---|---|---|
| 1 | 200 | 12 | 10 | 1.3510 |
| 2 | 2100 | 7 | 25 | 0.2278 |
| 3 | 4000 | 2 | 10 | -0.2310 |
| 4 | 200 | 2 | 40 | 0.1534 |
| 5 | 4000 | 12 | 40 | -0.0405 |
| 6 | 2100 | 7 | 25 | 0.1279 |
| 7 | 200 | 7 | 25 | 0.1912 |
| 8 | 2100 | 7 | 25 | -0.1739 |
| 9 | 2100 | 2 | 25 | -0.2705 |
| 10 | 2100 | 7 | 10 | 0.1750 |
| 11 | 2100 | 7 | 25 | -0.0670 |
| 12 | 4000 | 7 | 25 | -0.1692 |
| 13 | 2100 | 12 | 25 | 0.2848 |
| 14 | 2100 | 7 | 40 | 0.1945 |
| 15 | 4000 | 12 | 10 | 0.2729 |

| 16 | 4000 | 2 | 40 | 0.0851 |
| 17 | 2100 | 7 | 25 | 0.2790 |
| 18 | 200 | 2 | 10 | 0.3133 |
| 19 | 200 | 12 | 40 | 1.1132 |
| 20 | 2100 | 7 | 25 | 0.2990 |

The ESD measurements varied between a minimum of – 0.2705 kV to a maximum of 1.3510 kV over the range of 1.6215 kV. The data points showed diversity over the machining parameter combinations with negative and positive charge accumulated during machining. Below is Figure 57 displaying a scatterplot of the experimental observations for the electrostatic discharge observations. All experiments were performed under dry conditions with no mist or air utilised and the humidity and temperature was not controlled.
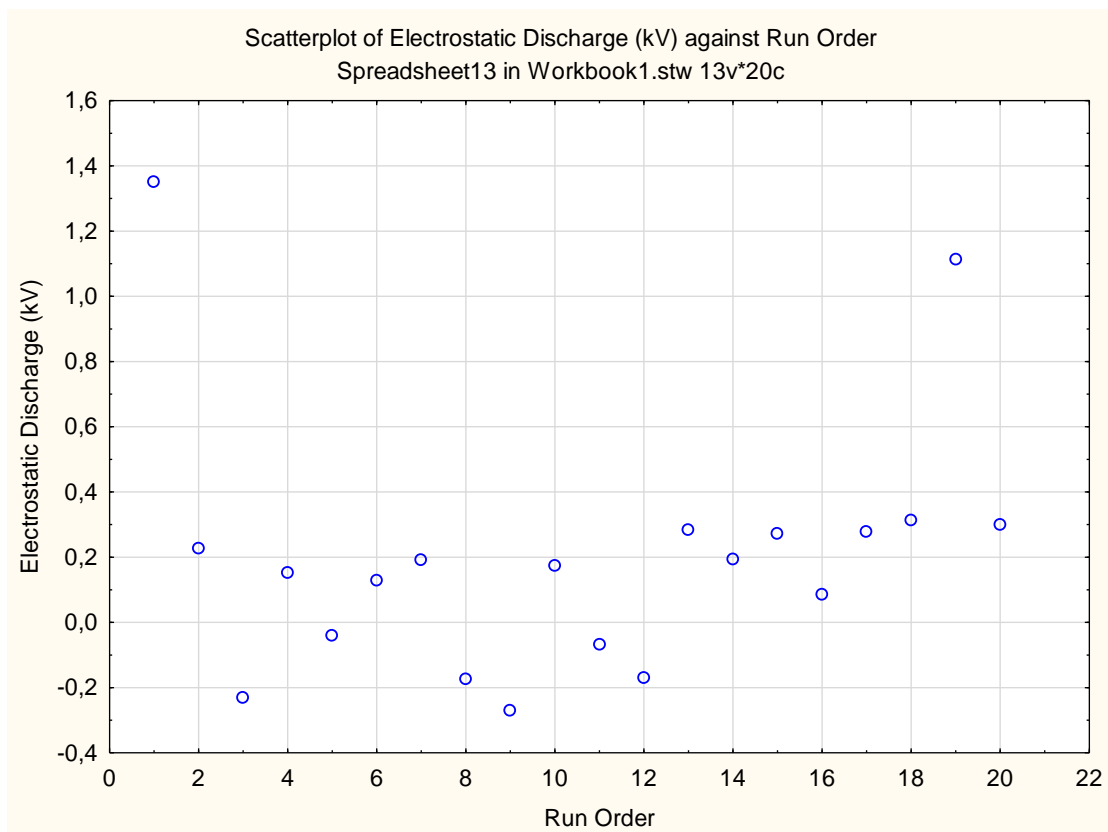


**Figure 57: Scatter diagram of the observations for electrostatic discharge for ONSI-56.**

The experimental observations indicate that the highest ESD occurred at observations 1 and 19. The minimum cutting speed was used and the maximum

feed rate was used. When the speed was increased to 2100 rpm and the medium feed rate was used, observations 2, 10, 13, 14, 17 and 19 showed a drop in the ESD generated, however, in the same range some observations indicated negative electrostatic potential. Making it unclear how the parameters where influencing the ESD.

The different behaviours of the ESD were accompanied by different types of chip formations between the cutting tool and the workpiece for the different experiments. During experiment 3, the ESD was acquired at – 0.2310 kV, generated at a cutting speed of 4000 rpm, feed rate of 2 mm/min, a depth of cut of 10 μm and a surface roughness of 7.3 nm. Figure 58 shows the chip formation around the workpiece.
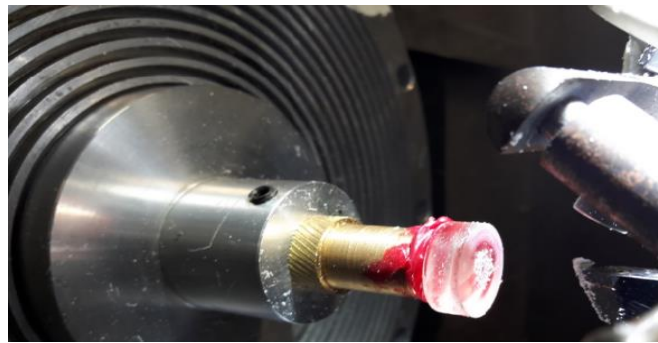

**Figure 58: Observation 3 chip build up.**

The chips were flying away from the surface, there was no chip build-up. The cutting tool was removing little material at a very high speed, even the surface roughness of this observation was optical quality. The ESD generated was substantially low creating the assumption that maybe the high speed and low feed and depth lead to low ESD, Figure 59 shows an image of the acquired data.
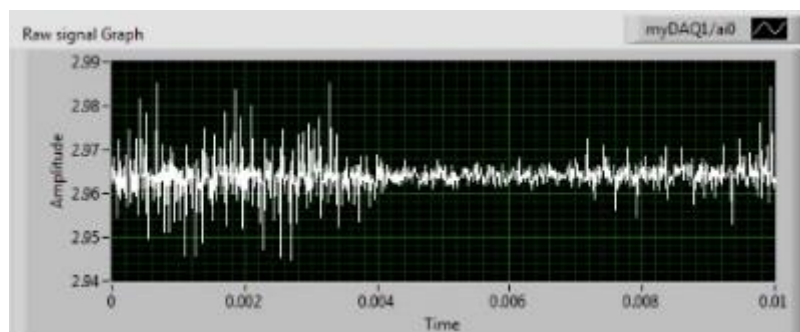

**Figure 59: Observation 3 acquisition data.**

118

The raw signal indicates that the voltage generated was below 3 V, and is negative. The 3 V acts as a zero point for the signal, anything below 3 V is negative and anything above 3 V is positive, as per the experimental chapter. The spikes indicate the possibility of noise interfering with the signal. The minimum values acquired shows that no discharge could have taken place.

In experiment 5, the ESD acquired was – 0.0405 kV, generated by 4000 rpm cutting speed, a feed of 12 mm/min, a 40 µm depth of cut and 11.9 nm surface roughness. Figure 60 shows the chip build-up which displayed long and fragmented chips around the workpiece.



**Figure 60: Observation 5 chip build up.**

In this experiment all the machining parameters were at maximum. The chips appeared thicker due to the high depth of cut, and they seemed attached towards the edge of the workpiece, as if to fall off, due to the high cutting speed. The chips' saw-like edges indicated that the material included other molecular materials within it, indicating that it was not one pure molecular material. Figure 61 shows the signal generated with LabVIEW.
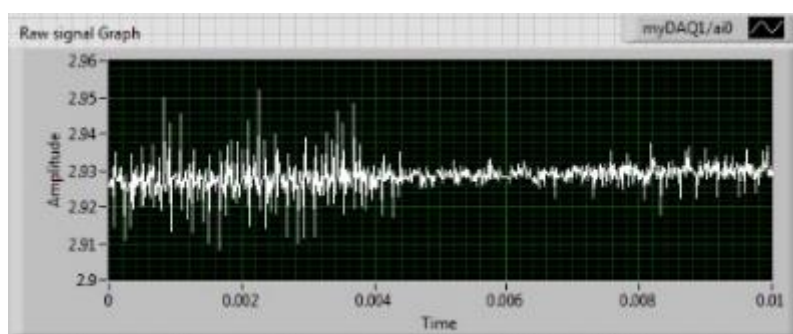


**Figure 61: Observation 5 acquisition data.**

The raw signal indicates that the voltage generated was below 3 V, and is negative. Common to both experiments 3 and 5 was the high speed leading to a negative electrostatic potential, which suggests that no discharge could have taken place.

In experiment 13, the ESD generated was 0.2848 kV, created with a cutting speed of 2100 rpm, a feed rate of 12 mm/min, a depth of cut of 25 μm, giving a surface roughness of 21 nm. Figure 62 depicts the chips formation, which showed big, long and tangled chips.
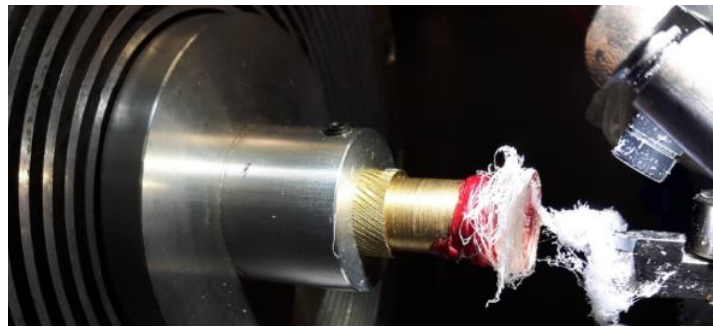


**Figure 62: Observation 13 chip build up.**

During cutting, when the tool separated from the workpiece the chips did not fall off, instead they were attached to the workpiece surface, which could have been due to the amount of chip formation. During tool separation, there was adhesion of the chips on the surface of the workpiece. The high speed may have caused the chips to follow the similar pattern of moving towards the edge of the surface. Compared to experiments 3 and 5, the surface roughness had increased slightly together with the increase in ESD measurements. However, that does not mean that a direct relationship exists between the ESD measurements and the surface roughness. Figure 63 shows the raw signal acquired with LabVIEW.
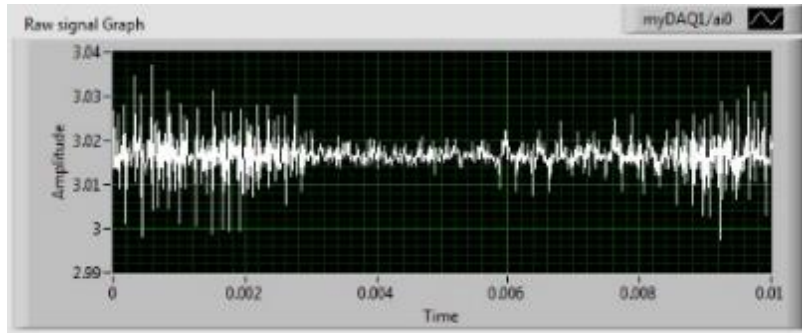
**Figure 63: Observation 13 acquisition data.**

The raw signal is above 3 V and is positive. The signal indicates that ESD may have occurred due to the sporadic spikes recorded. The voltage reading seems to be stable with the high concentration areas indicating the discharges.

In experiment 14, the ESD measured was 0.1945 kV, slightly below observation 13, obtained from 2100 rpm speed, 7 mm/min feed, 40 μm depth of cut, and a surface roughness of 20.2 nm. Figure 64 shows the chips created during machining.


**Figure 64: Observation 14 chip build up.**

The chips appeared lose around the edge of the workpiece. When the cutting tool separated from the workpiece the chips formed a tunnelled connection between the different surfaces due to static charge build-up. Even though the chips appeared to be discontinuous around the edges the static charge kept them together at the point of separation. The surface roughness decreased as compared to experiment 13 due to the decrease in the feed rate, it was inferred during modelling that a low feed rate

generated a low surface roughness, maybe it also generated a low ESD as well. The modelling section will try to assimilate if that is true or not. Figure 65 shows the raw signal obtained from LabVIEW.
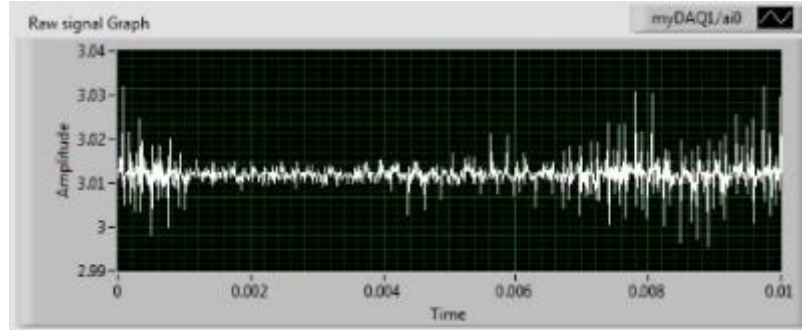


**Figure 65: Observation 14 acquisition data.**

The raw signal is above 3 V and is positive. The spikes are not as sporadic and high as experiment 13. However, the signal does indicate that a discharge may have taken place, and the signal is also stable, showing a good quality reading of the voltage.

## 4.2.1.1 Electrostatic Discharge Modelling of ONSI – 56

Having shown that there exists a relationship between the cutting parameters and the ESD, the probabilistic model is a follows:

$$V_{ONSI-56} = \beta_0 + \beta_1 s + \beta_2 s^2 + \beta_3 f + \beta_4 f^2 + \beta_5 d + \beta_6 d^2 + \beta_7 sf + \beta_8 sd + \beta_9 fd + \varepsilon \qquad (21)$$

Where:

$V_{ONSI-56}$ denotes the ESD of ONSI – 56, measured in kilovolts (kV)

s denotes the cutting speed in revolutions per minute (rpm)

f denotes the feed rate in millimetres per minute (mm/min)

d denotes the depth of cut in micrometres (µm)

$s^2$, $f^2$, $d^2$ denote the non-linear component of the cutting parameters

sf, sd, fd denote the interaction effects of the cutting parameters on the ESD

$\beta_0$ denotes the expected value of the ESD when s = f = d = 0

122

$\beta_1$, $\beta_3$, $\beta_5$ denote the contribution of the cutting parameters on the ESD to be estimated

$\beta_2$, $\beta_4$, $\beta_6$ denote the contribution of the non-linear component of the cutting parameters on the ESD to be estimated

$\beta_7$, $\beta_8$, $\beta_9$ denote the contribution of the interaction effect component on the ESD to be estimated

$\epsilon$ denotes the error in the system

## 4.2.1.2: Normality Test

Table 30 provides the ANOVA summary table, which will be used to check if the data is normally distributed. The data will be used to validate the existence of a relationship between the cutting parameters and the ESD generated during machining.

**Table 30: ESD ANOVA summary for ONSI-56.**

| Source | Degrees of freedom (DF) | Sum of Squares (SS) | Adjusted Mean Squares (MS) | F – value | P – value |
|---|---|---|---|---|---|
| Model | 9 | 2.6786 | 0.2976 | 8.38 | 0.001 |
| Lack of fit | 5 | 0.1651 | 0.0330 | 0.87 | 0.560 |
| Pure error | 5 | 0.1902 | 0.0381 | | |
| Total | 19 | 3.0339 | | | |

To check the normality of the data the global F – test needs to be performed under the assumption that:

$H_o$: $\beta_1 = 0$     $H_1$: $\beta_1 \neq 0$, where $H_o$ is the null hypothesis and $H_1$ is the alternative hypothesis.

The decision rule for the global F – test is to reject $H_o$ if the p – value < 0.05 or fail to reject $H_o$ if the p – value ≥ 0.05. What that means is that a p – value that is less than 0.05 indicates that the data is normally distributed.

The ANOVA table indicates that the model p – value is 0.001 < 0.05, which makes it significant for prediction purposes. The lack of fit has a p – value = 0.56 > 0.05, making it insignificant indicating that the model would be suitable to predict for new observations of the ESD. However, the global F – test needs to be performed on the model coefficients as well. Table 31 below provides the estimated regression un-coded coefficients for the empirical or prediction model. Model parameters are obtained with the method of least squares.

**Table 31: Regression coefficients for the ESD generated.**

| Term | Coefficient | Contribution | F – value | P – value | T – value |
|------|-------------|--------------|-----------|-----------|-----------|
| Constant | 0.0565 | | | | |
| s | -0.3205 | 38.34 % | 28.91 | 0.000 | -5.377 |
| f | 0.2931 | 32.07 % | 24.18 | 0.001 | 4.917 |
| d | -0.0376 | 0.53 % | 0.40 | 0.543 | -0.630 |
| s*s | 0.0429 | 7.19 % | 0.14 | 0.714 | 0.377 |
| f*f | 0.0390 | 1.73 % | 0.12 | 0.738 | 0.343 |
| d*d | 0.2166 | 4.82 % | 3.63 | 0.086 | 1.906 |
| s*f | -0.2024 | 12.24 % | 9.22 | 0.013 | -3.037 |
| s*d | 0.0501 | 0.75 % | 0.56 | 0.470 | 0.751 |
| f*d | -0.0884 | 2.34 % | 1.76 | 0.214 | -1.327 |

From the coefficients on the above table, the empirical model can be represented as follows:

$$\widehat{V_{ONSI-56}} = 0.0565 - 0.3205s + 0.2931f - 0.0376d + 0.0429s^2 + 0.0390f^2 + 0.2166d^2 - 0.2024sf + 0.0501sd - 0.0884fd \qquad (22)$$

The global F – test needs to be performed on the machining parameters to determine which terms are more suitable for prediction purposes. From the main cutting parameters, Table 31 shows that the cutting speed and feed rate are highly significant with p – values < 0.05. the depth of cut is not significant since the p – value = 0.543 > 0.05. None of the squared non-linear terms of the cutting parameters are significant for predicting the ESD because all their p – values > 0.05. However, the speed squared non-linear term has more than 7% contribution towards the

model, which is a significant contribution and it should be included in the model even though its p – value is not significant. From the interaction terms between the parameters, the cutting speed and feed are significant with p – value = 0.013 < 0.05, and the others are not significant. The cutting speed contributes more than 38% towards the variation of the ESD, followed by the feed rate with more than 32% influence. The interaction term between the speed and feed contributes more than 12% towards the change in the ESD.

 The negative sign on the T – value of the coefficient indicates that when the parameter increases the ESD decreases, and a positive sign indicates that when the coefficient increases the ESD also increases. Cutting speed and its interaction term with the feed, have a negative influence on the ESD. The feed rate has a positive influence on the ESD. However, still more investigations will have to be done to validate that.

## 4.2.1.3 Assumptions testing

Figure 66 below shows the residuals plot with all terms included in the model.
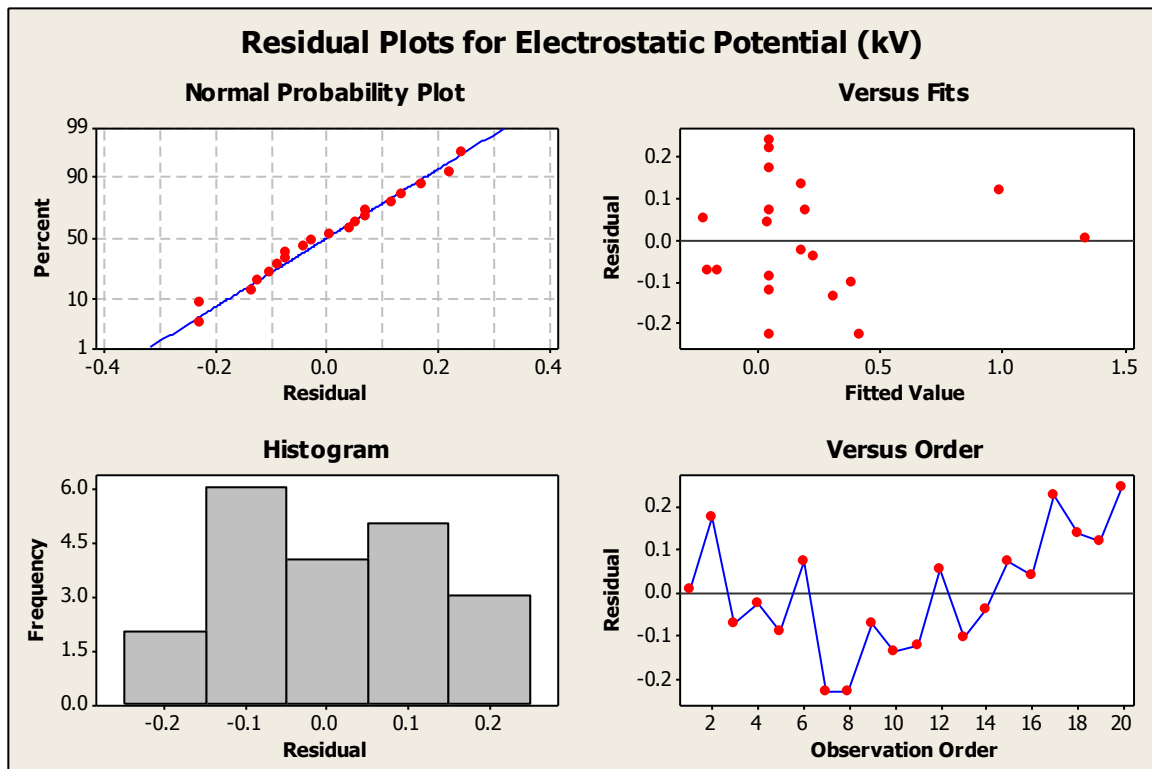


**Figure 66: Electrostatic discharge residual plots for ONSI-56.**

The residual plots for the electrostatic potential or ESD assist in checking the goodness of fit of the model. The normal probability plot shows that the data is normal almost lying completely on the least square line. The versus fits and versus order plots do not follow a set pattern, showing that the observations are independent and are variable. The histogram shows that the data is normally distributed. Table 32 shows the model summary of regression.

**Table 32: Regression model summary for ESD generated.**

| S | $R^2$ | Adjusted $R^2$ | Predicted $R^2$ |
|---|---|---|---|
| 0.1885 kV | 88.29 % | 77.75 % | 38.60 % |

Table 32 shows the error of regression (S) at 0.1885, which represents the average distance that the observed values deviate from the least squares line. The error of regression assumes the units of the electrostatic potential (kV) and in this case it is not too far from the average values measured. The $R^2$ = 88.29 %, is reasonably high and indicates that the model could predict the ESD response. The adjusted $R^2$ = 77.75 % indicates more than 70 % of the variation in the surface roughness can be accounted to the variation in the cutting parameters. The predicted $R^2$ is used to determine how well the model would predict the surface roughness for new observations and in this model it is 38.60 %. Even though the $R^2$ and adjusted $R^2$ are above 70 %, a predicted $R^2$ that is below 50% infers that this model does not have great predictive capability and needs further analysis to improve it.

## 4.2.1.3 Optimised Electrostatic Discharge Model

Table 33 provides the ANOVA summary table only for the un-coded significant terms in the model and will be used to check the normal distribution of the data.

**Table 33: Revised ESD ANOVA summary for ONSI-56.**

| Source | Degrees of freedom (DF) | Sum of Squares (SS) | Adjusted Mean Squares (MS) | F – value | P – value |
|---|---|---|---|---|---|
| Model | 4 | 2.4066 | 0.6016 | 14.39 | 0.000 |
| Lack of fit | 4 | 0.2896 | 0.0724 | 2.36 | 0.117 |
| Pure error | 11 | 0.3377 | 0.0307 | | |
| Total | 19 | 3.0339 | | | |

Table 33 above shows that the model is significant with p – value < 0.05, and the lack of fit insignificant with a p – value > 0.05. Table 34 below shows the un-coded significant model coefficients.

**Table 34: Revised model coefficients for the ESD generated.**

| Term | Coefficient | Contribution | F – value | P – value | T – value |
|---|---|---|---|---|---|
| Constant | -0.0219 | | | | |
| s | -2.479E-04 | 42.68 % | 24.56 | 0.000 | -4.956 |
| f | 0.1034 | 35.70 % | 20.54 | 0.000 | 4.532 |
| s*s | 5.437E-08 | 8.00 % | 4.61 | 0.049 | 2.146 |
| s*f | -2.1305E-05 | 13.62 % | 7.84 | 0.013 | -2.799 |

The global F – test shows that all the terms in Table 34 are significant since their p – values < 0.05. The cutting speed has the most effect on the change on the ESD with more than 40 %, followed by the feed rate with more than 35 % influence. The T – values signs and the coefficient sign indicate that the cutting speed and the interaction term between the speed and feed have a negative influence on the ESD. Meaning that whenever they increase, the ESD decreases. The feed rate and the squared non-linear speed term have a positive effect on the ESD, when they increase the ESD also increases.  The constant term represents $\beta_0$ coefficient, which represents the ESD should s = f = d = 0.

The revised prediction model can be represented as follows:

$$\widehat{V_{ONSI-56}} = -0.0219 - 2.479e^{-4}s + 0.1034f + 5.437e^{-8}s^2 - 2.1305e^{-5}sf \qquad (23)$$

## 4.2.1.4 Assumptions testing for the optimised model

Figure 67 shows the residual plots only for the significant terms.
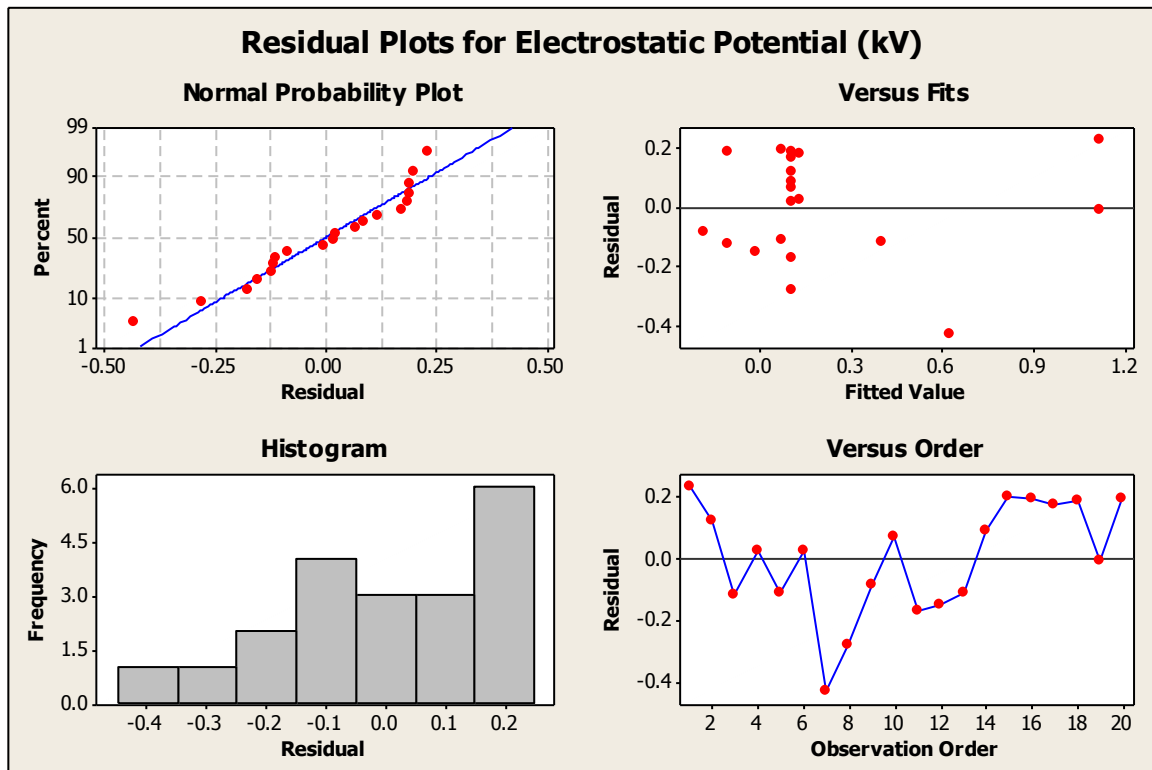


**Figure 67: ESD residual plots for ONSI-56 optimised model.**

The normal probability plot shows that the data follows the probability line even though there are some observations that seem to be pulling the data making it skew. The versus fits and versus order plots do not follow a set pattern, even though on the versus fits plot there are observations that are far from the rest of the cluster indicating that there could be outliers. The histogram is normally distributed and skewed to the left indicating also an indication that there could be unusual data points.

## 4.2.1.5 Further Investigations on Main effects on the Electrostatic Discharge

Figure 68 below displays the main effects plot showing the effect of the speed and feed on the ESD. The main effects plot for the cutting speed has a steep slope in the range from 200 – 2100 rpm which shows high correlation between speed and the ESD. As the speed increases in that range, the electrostatic potential gradually

decreases. Increasing the speed from 2100 – 4000 rpm causes a further decline in the ESD generation, validating a negative relationship between the speed and the ESD.

The feed rate between 2 – 7 mm/min displays a steep incline, indicating that when the feed increases, the ESD also increases. There is a direct positive relationship between the feed and the ESD. Increasing the feed from 7 – 12 mm/min causes an even steeper incline, showing the significant effect the feed rate has on the ESD generated.
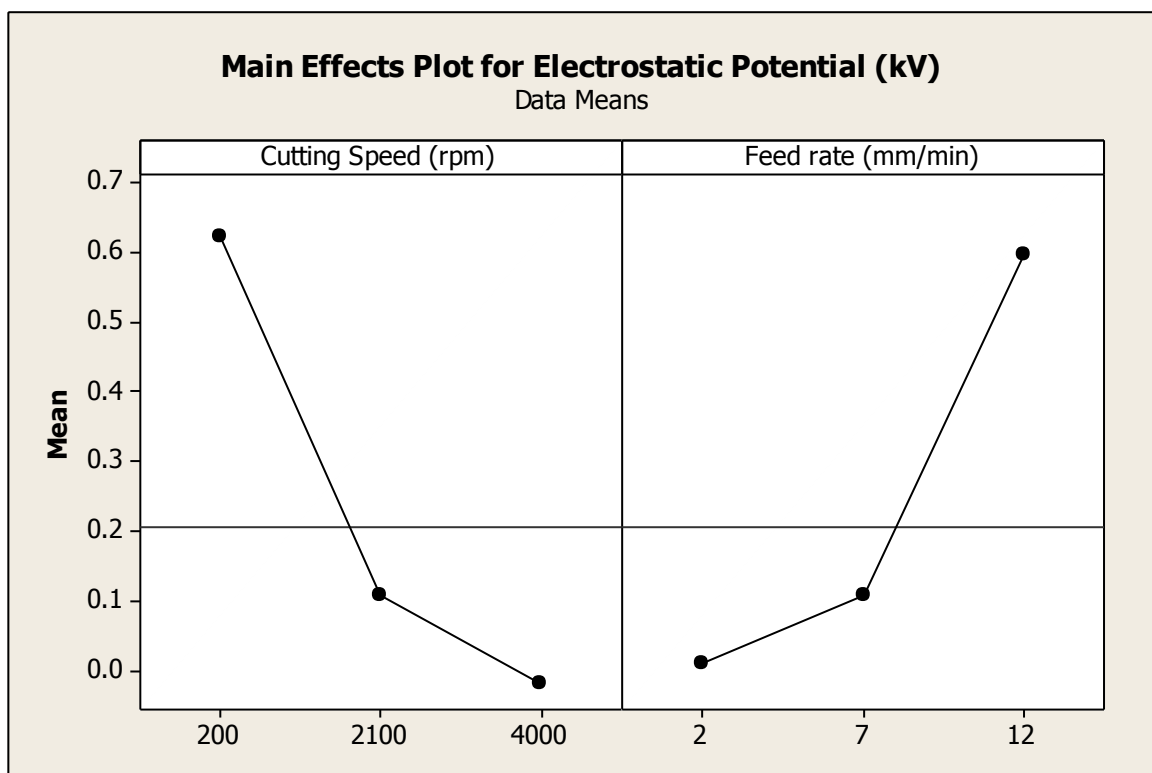


**Figure 68: ESD main effects plot for ONSI-56 optimised model.**

## 4.2.1.6 Interaction effects on the Electrostatic Discharge

Figure 69 below shows the interaction plot for ESD against cutting speed and feed rate. Keeping the cutting speed constant at 200 rpm and varying the feed rate at 2 – 7 mm/min shows a slight decline in the ESD generated. The decrease is gradual but minimal. Increasing the feed rate from 7 – 12 mm/min shows a sharp incline in the ESD generated. So the condition of low speed and high feed creates the most static charges between the different cutting tool and workpiece.

129

Keeping the cutting speed constant at 2100 rpm and varying the feed rate from 2 – 7 mm/min increases the ESD generated. A further increase in the feed rate from 7 – 12 mm/min also increases the ESD, however the increase is not at high as that generated when the speed is 200 rpm. Constantly keeping the speed at 4000 rpm and varying the feed between 2 – 7 mm/min shows a decline in the static generated. However, increasing the feed from 7 – 12 mm/min shows an increase in the ESD generated. A common observation in all the different scenarios is that when the feed rate is high, between 7 – 12 mm/min, the ESD generated increases regardless of the level of the cutting speed.
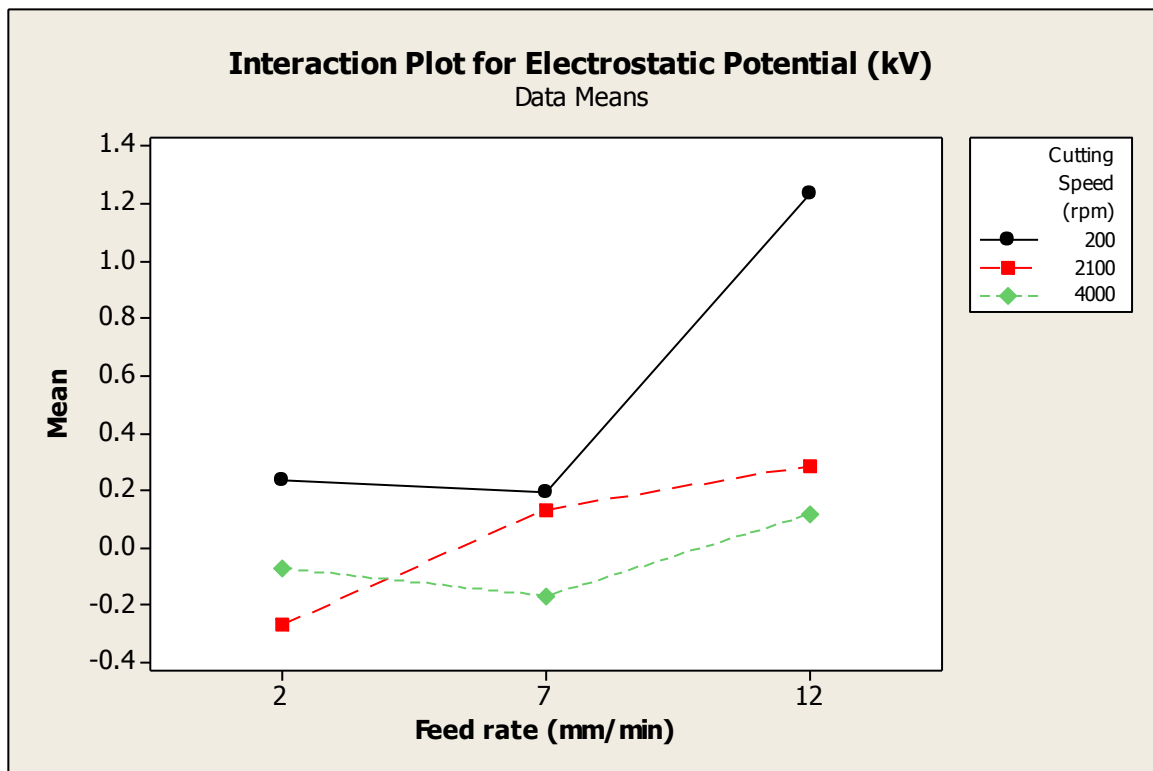


**Figure 69: ESD interaction plot for ONSI-56 optimised model.**

## 4.2.1.7 Contour plot of the Electrostatic Discharge

Figure 70 shows the contour plot for the electrostatic potential against the feed and speed.
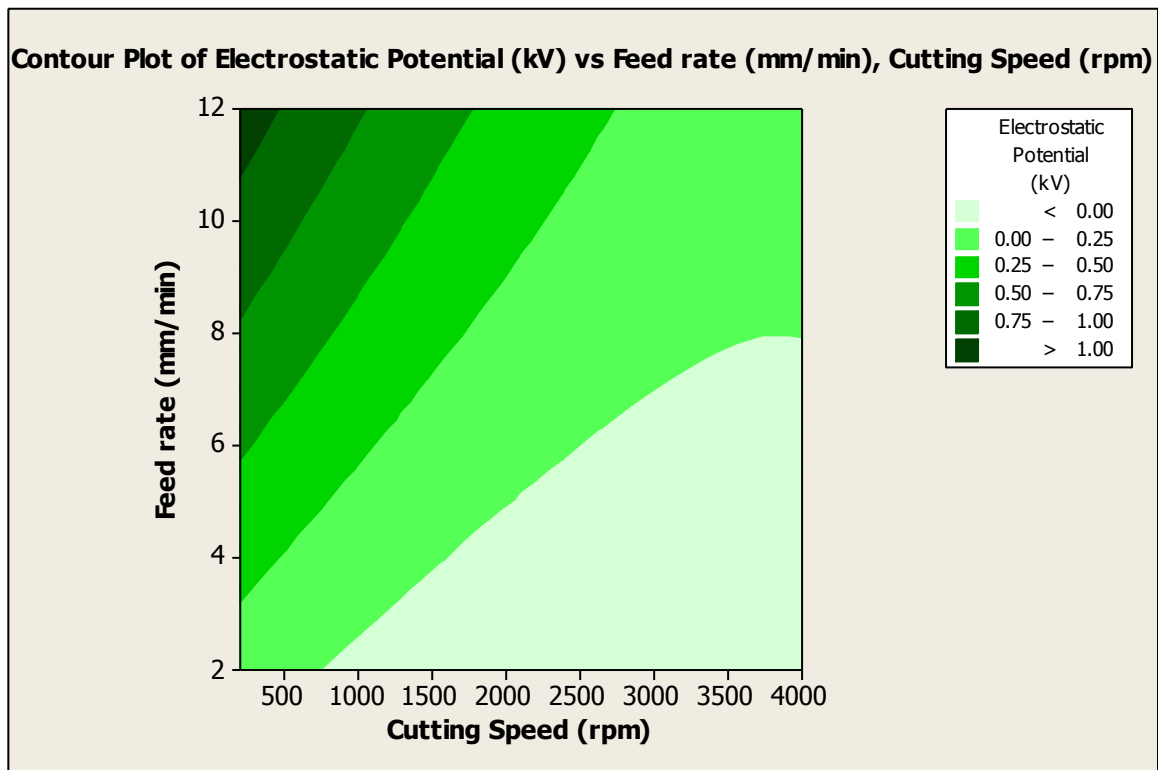
**Figure 70: ESD contour plot for ONSI-56.**

The ultimate goal during machining of contact lens polymers is to have minimum ESD generated to prevent bacterial adhesion on the contact lens material surface and to also reduce the rate of tool failure for a cost effective process. The contour plot shows that the best cutting conditions would be with a cutting speed between approximately 1000 – 4000 rpm and the feed rate between 2 – 7 mm/min, the ESD generated is less than 0.25 kV in that region (light green shade). However, the feed should not be increased if the cutting speed used is low. Keeping the speed at 1000 rpm and varying the feed rate between 2 – 7 mm/min would increase the ESD gradually exiting the optimum region. Instead using a high speed and varying the feed will keep the ESD within the optimum low region.

### 4.2.1.8 Model summary

Table 35 displays the model summary of regression with the error of regression 0.2045, which slightly increased but is not too high. The $R^2$ = 79.32 % which has dropped from the previous 88.29 %, but is still high to predict for new observations.

| S | $R^2$ | Adjusted $R^2$ | Predicted $R^2$ |
|---|---|---|---|
| 0.2045 kV | 79.32 % | 73.81 % | 60.58 % |

Taking into account the sample size and the number of β coefficients in the model, the adjusted $R^2$ shows that 73.81 % of the variation in the ESD can be attributed to the variation in the cutting speed and the feed rate. The predicted $R^2$ = 60.58 % which is not higher than $R^2$ showing that the model does not over fit and it can predict for new observations not included in the calculations. The predictive power of the optimised model has greatly improved from the previous 38.60 %.

Table 36 below displays the original ESD measurements and the predicted ones from the obtained model. It can be concluded that modelling of ESD during single point diamond turning of ONSI – 56 is possible and has been done and analysed in this section. The cutting speed and the feed rate where found to be the most influential parameters. The charge generated varied between a minimum negative and a maximum positive in the same material due to different combinations of the cutting speed and feed. High speed and low feed generates the least ESD which is what is required during diamond turning to reduce tool failure.

**Table 36: Predicted ESD for ONSI-56.**

| Run Order | Cutting Speed (rpm) | Feed rate (mm/min) | Depth of Cut (µm) | Electrostatic discharge (kV) | Predicted Electrostatic discharge (kV) |
|---|---|---|---|---|---|
| 1 | 200 | 12 | 10 | 1.3510 | 1.1199 |
| 2 | 2100 | 7 | 25 | 0.2278 | 0.1077 |
| 3 | 4000 | 2 | 10 | -0.2310 | -0.1073 |
| 4 | 200 | 2 | 40 | 0.1534 | 0.1289 |
| 5 | 4000 | 12 | 40 | -0.0405 | 0.0742 |
| 6 | 2100 | 7 | 25 | 0.1279 | 0.1077 |

| 7 | 200 | 7 | 25 | 0.1912 | 0.6244 |
|---|---|---|---|---|---|
| 8 | 2100 | 7 | 25 | -0.1739 | 0.1077 |
| 9 | 2100 | 2 | 25 | -0.2705 | -0.1855 |
| 10 | 2100 | 7 | 10 | 0.1750 | 0.1077 |
| 11 | 2100 | 7 | 25 | -0.0670 | 0.1077 |
| 12 | 4000 | 7 | 25 | -0.1692 | -0.0165 |
| 13 | 2100 | 12 | 25 | 0.2848 | 0.4008 |
| 14 | 2100 | 7 | 40 | 0.1945 | 0.1077 |
| 15 | 4000 | 12 | 10 | 0.2729 | 0.0742 |
| 16 | 4000 | 2 | 40 | 0.0851 | -0.1073 |
| 17 | 2100 | 7 | 25 | 0.2790 | 0.1077 |
| 18 | 200 | 2 | 10 | 0.3133 | 0.1289 |
| 19 | 200 | 12 | 40 | 1.1132 | 1.1199 |
| 20 | 2100 | 7 | 25 | 0.2990 | 0.1077 |

## 4.2.2 Electrostatic Discharge Modelling of PMMA

The electrostatic potential was acquired with LabView as explained in the experimental chapter. The average ESD measurements were used in the development of the model. Table 37 below shows the experimental observations for PMMA hard contact lens polymer.

**Table 37: ESD generated for PMMA.**

| Run Order | Cutting Speed (rpm) | Feed rate (mm/min) | Depth of Cut (µm) | Electrostatic discharge (kV) |
|---|---|---|---|---|
| 1 | 200 | 12 | 10 | 0.4133 |
| 2 | 2100 | 7 | 25 | 0.2895 |
| 3 | 4000 | 2 | 10 | 0.1575 |
| 4 | 200 | 2 | 40 | 0.7075 |
| 5 | 4000 | 12 | 40 | 0.5268 |
| 6 | 2100 | 7 | 25 | 0.3537 |
| 7 | 200 | 7 | 25 | 0.4393 |
| 8 | 2100 | 7 | 25 | 0.3062 |

| 9 | 2100 | 2 | 25 | 0.3109 |
| 10 | 2100 | 7 | 10 | 0.0780 |
| 11 | 2100 | 7 | 25 | 0.2064 |
| 12 | 4000 | 7 | 25 | 0.1921 |
| 13 | 2100 | 12 | 25 | 0.5391 |
| 14 | 2100 | 7 | 40 | 0.2658 |
| 15 | 4000 | 12 | 10 | 0.4172 |
| 16 | 4000 | 2 | 40 | 0.2872 |
| 17 | 2100 | 7 | 25 | 0.2371 |
| 18 | 200 | 2 | 10 | 0.4290 |
| 19 | 200 | 12 | 40 | 0.4919 |
| 20 | 2100 | 7 | 25 | 0.3014 |

The electrostatic discharge measurements varied between a minimum of 0.0780 kV to a maximum of 0.7075 kV over the range of 0.6295 kV. That showed the diversity of the data with positive charge potential accumulated during machining. Figure 71 shows the scatterplot of the experimental observations. All experiments were performed under dry cutting and all atmospheric conditions were not controlled (temperature/humidity).
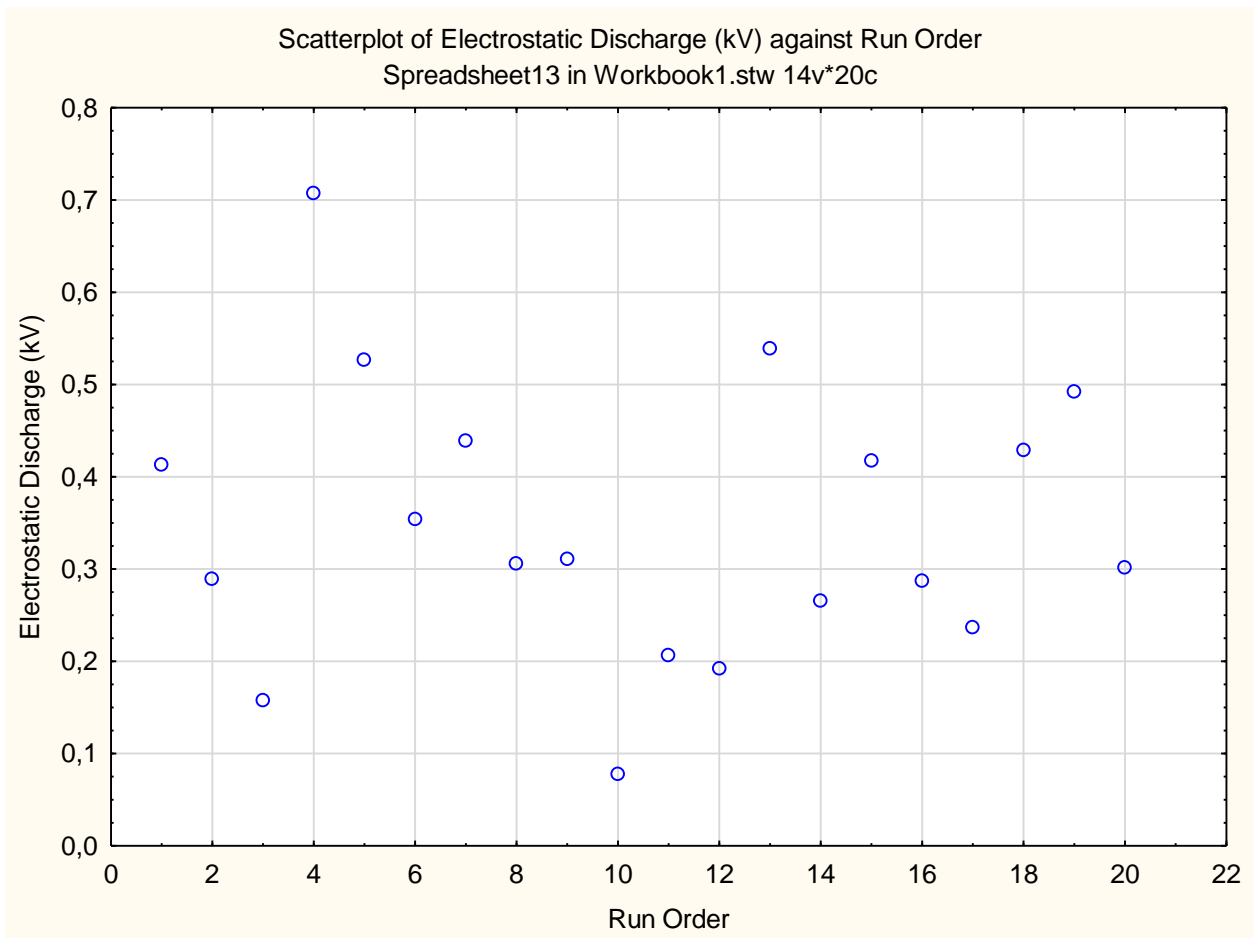
**Figure 71: ESD observations for PMMA.**

The experimental observations for ESD indicate that the highest ESD occurred at experiment 4 with the minimum speed and feed and maximum depth of cut. Followed by experiment 5, with the ESD obtained with the maximum speed, feed and depth of cut, making it unclear to assume how the speed and feed influence the ESD generated. Interestingly, in experiment 15, the ESD generated is high and acquired with a maximum speed and feed, and minimum depth of cut, also making it unclear to assume how the depth of cut influences the ESD. In experiment 16, a maximum speed and depth, and a minimum feed rate generate an ESD almost half the size of that generated in observation 15. The majority of high ESD's produced are acquired at a speed of 200 rpm. However, all the results are dynamic and make it difficult to draw assumptions as to how the parameters affect the ESD.

The ESD generated with the different cutting parameters was accompanied with different types of chip formations between the cutting tool and the workpiece. During experiment 4, the average ESD was acquired as 0.7075 kV, generated at a cutting speed of 200 rpm, feed rate of 2 mm/min and depth of cut of 40 μm, and a surface roughness of 57.3 nm. Figure 72 shows the chip formation around the workpiece.



**Figure 72: Observation 4 chip build up.**

There was a continuous chip build-up due to the low speed and feed. The high depth of cut and low feed created longer contact time between the cutting tool and polymer, generating more charge to build. When the tool separated from the polymer, that charge on the chips created the tunnel preventing the chips from falling off. The high ESD and high surface roughness under the cutting parameters could indicate that there exists some correlation between them. Figure 73 shows a screenshot of the signal acquired from the front panel of LabView, the signal is raw data obtained.
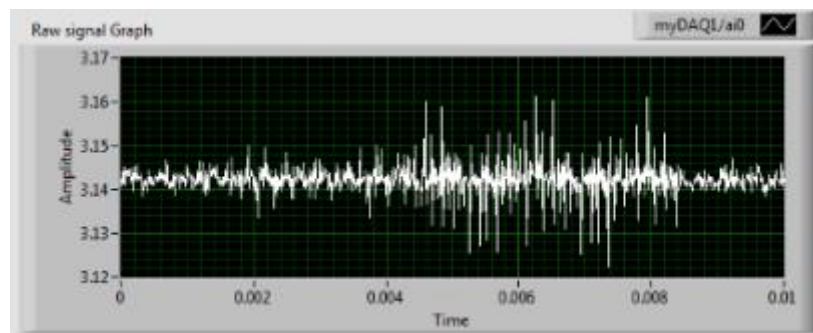


**Figure 73: Observation 4 data acquisition.**

The raw signal indicates that the voltage generated is above 3 V, and is positive as per Table 37 above. The spikes indicate the possibility of two things, that there is

discharge taking place between the cutting tool and the polymer material, or that there is interference in the voltage cable distorting the signal.

Figure 74 shows the chip formation obtained in experiment 5, with the ESD generated as 0.5268 kV, with the cutting speed of 4000 rpm, a feed of 12 mm/min, a depth of cut of 40 μm, and a surface roughness of 10.4 nm.
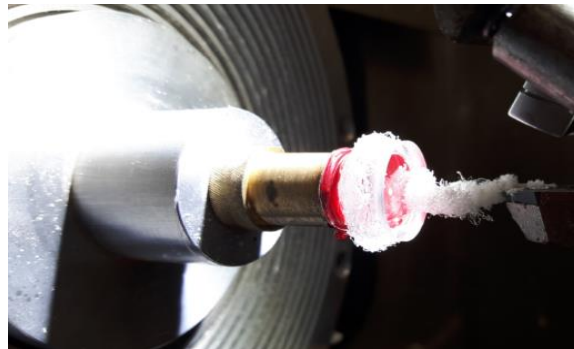


**Figure 74: Observation 5 chip build up.**

The chips appeared fine, segmented and held together around the edges of the workpiece. The cutting tool appeared to have a chip build-up on its cutting edge. All the cutting parameters during the experiment were high, however, the ESD and surface roughness, were both less than what was obtained in experiment 4. The chips, however, also did not fall off when the tool separated from the workpiece but created a tunnelling effect. If there was no charge generated, the chips would fall off and not be held together by some invisible field. Figure 75 shows the screenshot generated on the front panel of LabView, for the raw signal captured.
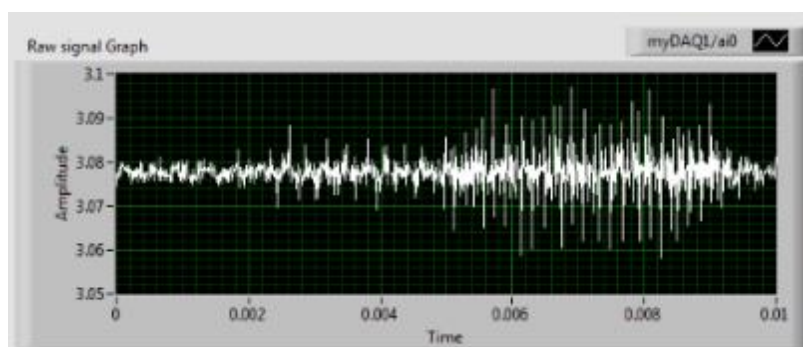


**Figure 75: Observation 5 data acquisition.**

A positive voltage was captured, and it was less than what was obtained from experiment 4. The level of the voltage coming in seems to be stable with some minor

distortions due to noise affecting the quality of the signal, but then the signal changes and increases indicating activity during machining. The signal indicates discharge that may have taken place potentially affecting the cutting tool at a microscopic level.

In Figure 76 for experiment 14, the ESD measured was 0.2658 kV, with speed at 2100 rpm, feed 7 mm/min, depth 40 μm, and a surface roughness of 26.4 nm. The ESD was lower than in experiment 5, but the surface roughness was higher and obtained with a lower speed and feed, but the same depth of cut.



**Figure 76: Observation 14 chip build up.**

The chips generated appeared thick, and clustered around the edges of the workpiece. The chips appeared to be held together by an invisible field because they did not fall off but the lump was hanging at the bottom/lower section of the workpiece. During tool separation they did not tunnel but remained clustered around the workpiece. Figure 77 shows a screenshot of the raw signal obtained from LabView.



**Figure 77: Observation 14 data acquisition.**

138

The voltage coming in is lower than experiment 4 and 5 because the average ESD generated is lower as well. The static discharge is lower and more sporadic. That could be due to the electrostatic sensor picking up the amount of charge accumulated on the clustered chips around the edge of the workpiece.

Figure 78 shows experiment 19 with a measured ESD of 0.4919 kV. The cutting parameters are a speed of 200 rpm, feed of 12 mm/min, a depth of cut 40 µm, and a measured surface roughness of 203.2 nm.
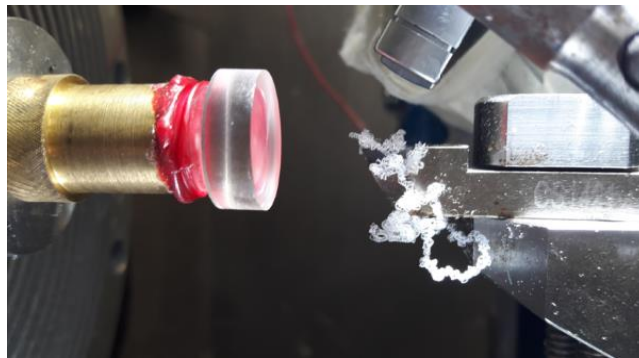

**Figure 78: Observation 19 chip build up.**

The chips appeared thick and formed a string like configuration around the cutting tool, held securely by an invisible field. The surface roughness in the entire experiment was the worst surface roughness, however, it has not been proven that there exists a direct relationship between the chip formed, the ESD generated and the measured surface roughness. The ESD is not as high at that generated from experiments 4 and 5 but is it substantially higher than in experiment 14. Common to all the experiments mentioned is the maximum depth of cut, and the positive charge generated in all the experiments performed, creating the impression that PMMA loses electrons. Figure 79 displays a screenshot of the raw signal acquired from LabVIEW.
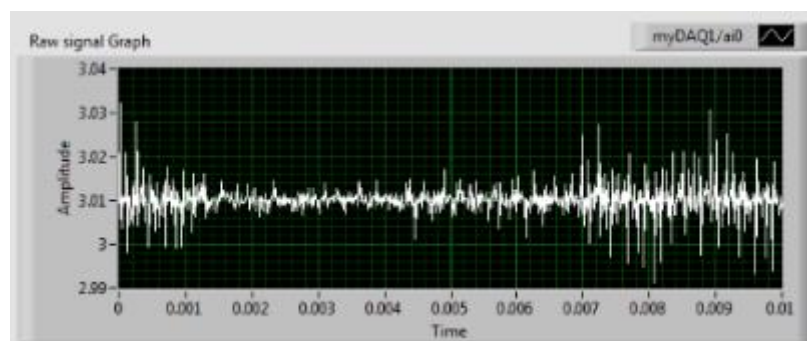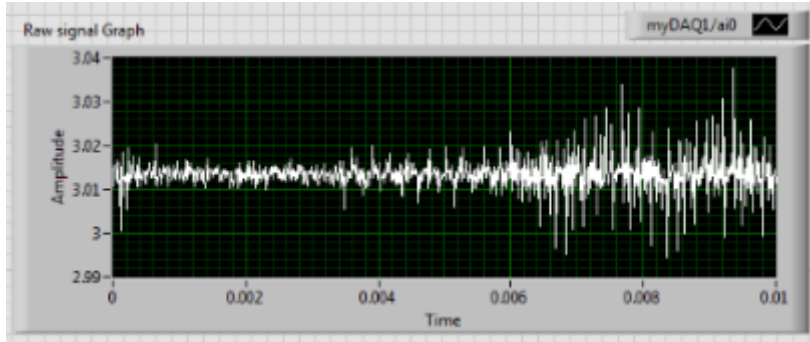
**Figure 79: Observation 19 data acquisition.**

The voltage coming in is lower than experiments 4 and 5 because the average ESD generated is lower as well. The charge build-up appears constant with minor disturbances. The static discharge appears to take place and appears to be concentrated and that could be due to the electrostatic sensor picking up the charge built-up around the string-like polymer on the edge of the cutting tool.

## 4.2.2.1 Electrostatic Discharge Modelling of PMMA

Having shown that there exists a relationship between the cutting parameters and the ESD generated during single point diamond turning of PMMA for contact lens making, the probabilistic model is a follows:

$$V_{PMMA} = \beta_0 + \beta_1 s + \beta_2 s^2 + \beta_3 f + \beta_4 f^2 + \beta_5 d + \beta_6 d^2 + \beta_7 sf + \beta_8 sd + \beta_9 fd + \varepsilon \qquad (24)$$

Where:

$V_{PMMA}$ denotes the ESD of PMMA, measured in kilovolts (kV)

s denotes the cutting speed in revolutions per minute (rpm)

f denotes the feed rate in millimetres per minute (mm/min)

d denotes the depth of cut in micrometres (µm)

$s^2$, $f^2$, $d^2$ denote the non-linear component of the cutting parameters

sf, sd, fd denote the interaction effects of the cutting parameters on the ESD

$\beta_0$ denotes the expected value of the ESD when s = f = d = 0

$\beta_1$, $\beta_3$, $\beta_5$ denote the contribution of the cutting parameters on the ESD to be estimated

140

$\beta_2, \beta_4, \beta_6$ denote the contribution of the non-linear component of the cutting parameters on the ESD to be estimated

$\beta_7, \beta_8, \beta_9$ denote the contribution of the interaction effect component on the ESD to be estimated

$\epsilon$ denotes the error in the system

## 4.2.2.2 Normality Test

Table 38 provides the ANOVA summary table, which will be used to check if the data is normally distributed. The data will be used to validate the existence of a relationship between the cutting parameters and the ESD generated during machining.

**Table 38: ESD ANOVA summary for PMMA.**

| Source | Degrees of freedom (DF) | Sum of Squares (SS) | Adjusted Mean Squares (MS) | F – value | P – value |
|--------|------------------------|---------------------|----------------------------|-----------|-----------|
| Model | 9 | 0.3928 | 0.0436 | 12.61 | 0.000 |
| Lack of fit | 5 | 0.0207 | 0.0041 | 1.49 | 0.336 |
| Pure error | 5 | 0.0139 | 0.0028 | | |
| Total | 19 | 0.4274 | | | |

To check the normality of the data the global F – test needs to be performed under the assumption that:

$H_o: \beta_1 = 0$     $H_1: \beta_1 \neq 0$, where $H_o$ is the null hypothesis and $H_1$ is the alternative hypothesis.

The decision rule for the global F – test is to reject $H_o$ if the p – value < 0.05 or fail to reject $H_o$ if the p – value ≥ 0.05. What that means is that a p – value that is less than 0.05 indicates that the data is normally distributed.

The ANOVA table indicates that the model p – value is 0.000 < 0.05, which makes it significant for prediction purposes. The lack of fit has a p – value = 0.336 > 0.05, making it insignificant and making the model suitable for prediction of new observations of the ESD. The global F – test needs to be performed on the model coefficients as well. Table 39 below provides the estimated regression un-coded coefficients for the empirical or prediction model. Model parameters are obtained with the method of least squares.

**Table 39: ESD model coefficients for PMMA.**

| Term | Coefficient | Contribution | F – value | P – value | T – value |
|------|-------------|--------------|-----------|-----------|-----------|
| Constant | 0.4087 | | | | |
| s | -1.75E-04 | 20.62 % | 23.42 | 0.005 | -3.592 |
| f | -0.0975 | 6.26 % | 7.12 | 0.001 | -4.459 |
| d | 0.0269 | 15.66 % | 17.77 | 0.009 | 3.219 |
| s*s | 1.74E-08 | 17.54 % | 3.13 | 0.107 | 1.769 |
| f*f | 0.0069 | 16.34 % | 23.53 | 0.001 | 4.850 |
| d*d | -3.60E-04 | 4.61 % | 5.22 | 0.045 | -2.285 |
| s*f | 9.61E-06 | 16.98 % | 19.28 | 0.001 | 4.391 |
| s*d | -5.17E-07 | 0.43 % | 0.50 | 0.495 | -0.708 |
| f*d | -3.67E-04 | 1.55 % | 1.75 | 0.216 | -1.322 |

From the coefficients on the above table, the empirical model can be represented as follows:

$$\widehat{V_{PMMA}} = 0.4087 - 1.75e^{-4}s - 0.0975f + 0.0269d + 1.74e^{-8}s^2 + 0.0069f^2 - 3.60e^{-4}d^2 + 9.61e^{-6}sf - 5.17e^{-7}sd - 3.67e^{-4}fd \qquad (25)$$

The above Table 39 shows that all the main cutting parameters are significant because their p – values < 0.05. Whenever the cutting speed and feed rate increase, the ESD decreases, so there is a negative relationship with those cutting parameters as indicated by the negative T – values. The depth of cut, however, has a positive relationship with the ESD, such that when it increases the ESD also increases. The speed, feed and depth have a combined contribution of more than 42 % towards the

change in the ESD. The squared non-linear terms for the feed and depth of cut are significant but that of the speed is not. However, the squared non-linear term for speed has the most contribution of all the squared non-linear terms, and even though it has a p – value that is not significant. The interaction term between the speed and feed is the only one significant with a contribution of more than 17 % towards a positive effect on the ESD.

### 4.2.2.3 Assumptions testing

Figure 80 below shows the residual plots with all terms included in the predictive model.
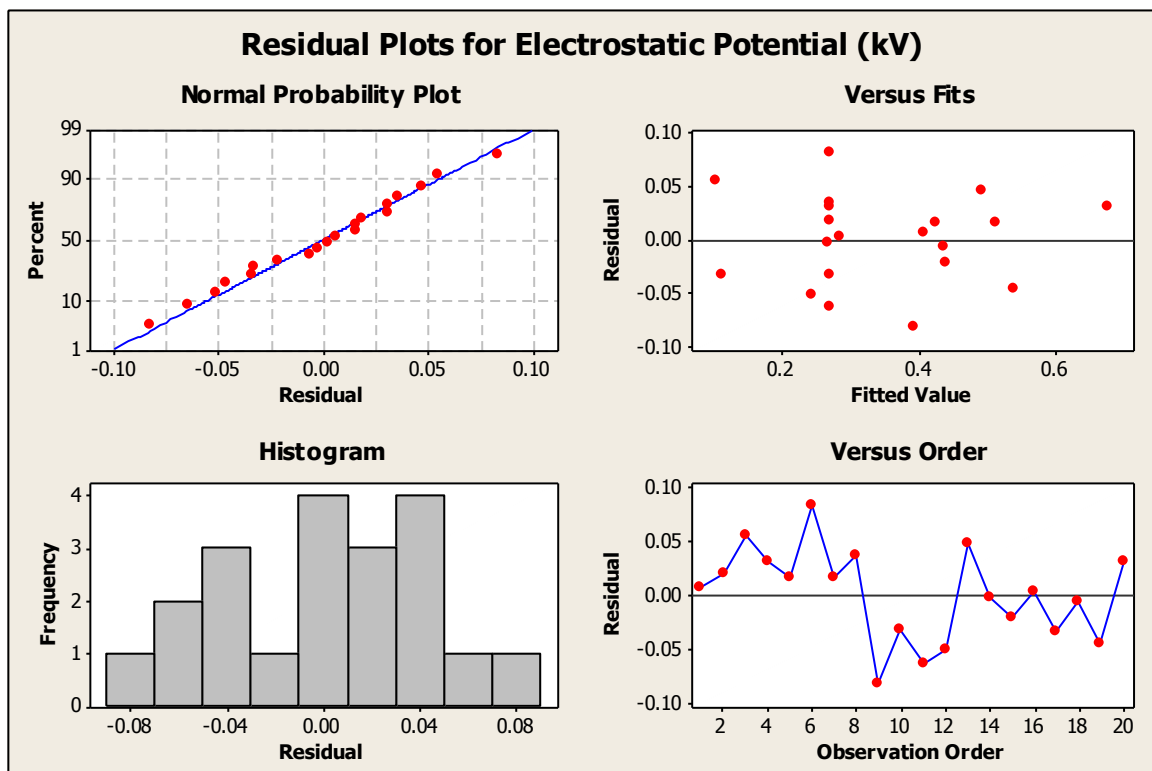


**Figure 80: ESD residual plots for PMMA.**

The normal probability plot for the residuals shows that the data is normally distributed along the least squares line. The versus fits and versus order plots do not follow any set patterns, showing that the observations are variable and independent from each other. The histogram is normally distributed but slightly stretched towards the right, an indication that there are data points that are slightly unusual or concentrated at a certain frequency region.

143

Table 40 shows the model summary of regression.

**Table 40: ESD regression model summary.**

| S | $R^2$ | Adjusted $R^2$ | Predicted $R^2$ |
|---|---|---|---|
| 0.0588 kV | 91.90 % | 84.62 % | 45.84 % |

Table 40 shows the error of regression (S) at 0.0588, which represents the average distance that the observed values deviate from the least squares line. The error of regression assumes the units of the electrostatic potential (kV) and in this case it is a fairly small gap because it is less than the minimum observation value of 0.0780 kV. The $R^2$ = 91.90 %, is reasonably high and indicates that the model could predict the ESD response. The adjusted $R^2$ = 84.62 % indicates more than 80 % of the variation in the surface roughness can be accounted to the variation in the cutting parameters. The predicted $R^2$ is used to determine how well the model would predict the surface roughness for new observations and in this model it is 45.84 %. Even though the $R^2$ and adjusted $R^2$ are above 80 %, a predicted $R^2$ that is below 50% infers that this model does not have great predictive capability and needs further optimisation to improve it.

## 4.2.2.3 Optimised Electrostatic Discharge Model

Table 41 below provides the ANOVA summary table only for the un-coded significant terms in the model and will be used to check the normal distribution of the data.

**Table 41: Revised ESD ANOVA summary.**

| Source | Degrees of freedom (DF) | Sum of Squares (SS) | Adjusted Mean Squares (MS) | F – value | P – value |
|---|---|---|---|---|---|
| Model | 5 | 0.3636 | 0.0727 | 15.96 | 0.000 |
| Lack of fit | 9 | 0.0499 | 0.0055 | 2.00 | 0.231 |
| Pure error | 5 | 0.0139 | 0.0028 | | |
| Total | 19 | 0.4274 | | | |

Table 41 above shows that the model is significant with p – value < 0.05, and the lack of fit is insignificant with a p – value = 0.231 > 0.05. Table 42 below shows the un-coded significant model coefficients.

**Table 42: Revised ESD regression model coefficients.**

| Term | Coefficient | Contribution | F – value | P – value | T – value |
|---|---|---|---|---|---|
| Constant | 0.6233 | | | | |
| s | -1.15E-04 | 22.28 % | 30.19 | 0.000 | -5.495 |
| f | -0.1005 | 6.77 % | 30.42 | 0.000 | -5.515 |
| d | 0.0052 | 16.91 % | 13.49 | 0.003 | 3.673 |
| f*f | 0.0064 | 35.68 % | 28.47 | 0.000 | 5.336 |
| s*f | 9.61E-06 | 18.35 % | 14.64 | 0.002 | 3.826 |

The global F – test shows that all the terms in Table 42 are significant since their p – values < 0.05. The speed and feed both have a negative effect on the ESD generated during diamond machining of PMMA, as shown by the negative T – value. The squared non-linear term of the feed rate has the greatest contribution towards to variability of the ESD (up to 35 %), that means that even though the feed rate displays about a 6 % contribution towards the ESD, once raised to a higher order increasing it increases the ESD generated. The depth of cut has a positive influence on the ESD with more than 16 % contribution towards its changes. The speed and feed interaction term has a positive relationship with the ESD with a contribution of up to 18 % towards its variation. The constant term represents $\beta_0$ coefficient, which represents the ESD should s = f = d = 0, it cuts the y – intercept.

The revised prediction model can be represented as follows:

$$\widehat{V_{PMMA}} = 0.6233 - 1.15e^{-4}s - 0.1005f + 0.0052d + 0.0064f^2 + 9.61e^{-6}sf \qquad (26)$$

## 4.2.2.4 Assumptions testing for the optimised model

Figure 81 shows the residual plots for the significant terms only. The normal probability plot shows that some of the data is under-estimated and some over-estimated, but it follows the least squares line, showing it to be normally distributed. The versus fits and versus order plots do not follow a set pattern, indicating that the

means of the observations are independent from each other and the data is variable. The histogram is normally distributed with a slight concentration of data towards the right.
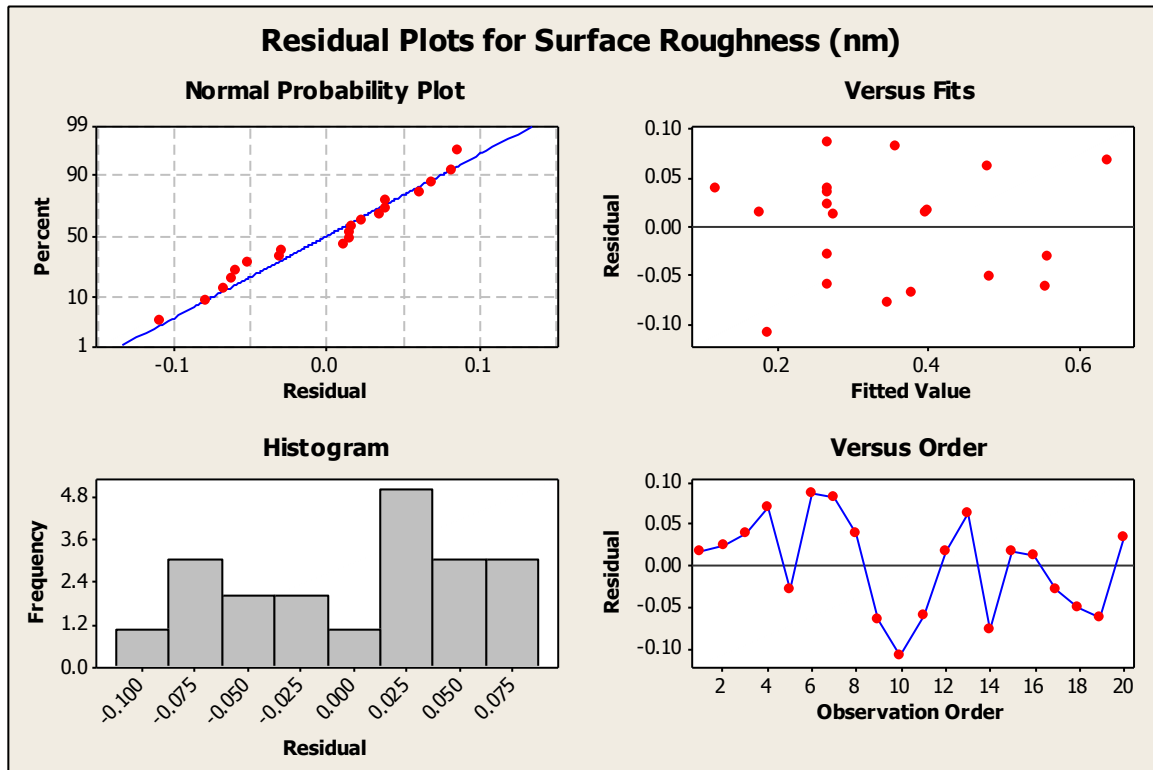


**Figure 81: Revised ESD residual plots for PMMA.**

## 4.2.2.5 Further Investigations on Main effects on the Electrostatic Discharge

Figure 82 below shows the main effects plot showing the effect of the speed, feed and depth of cut on the ESD generated.
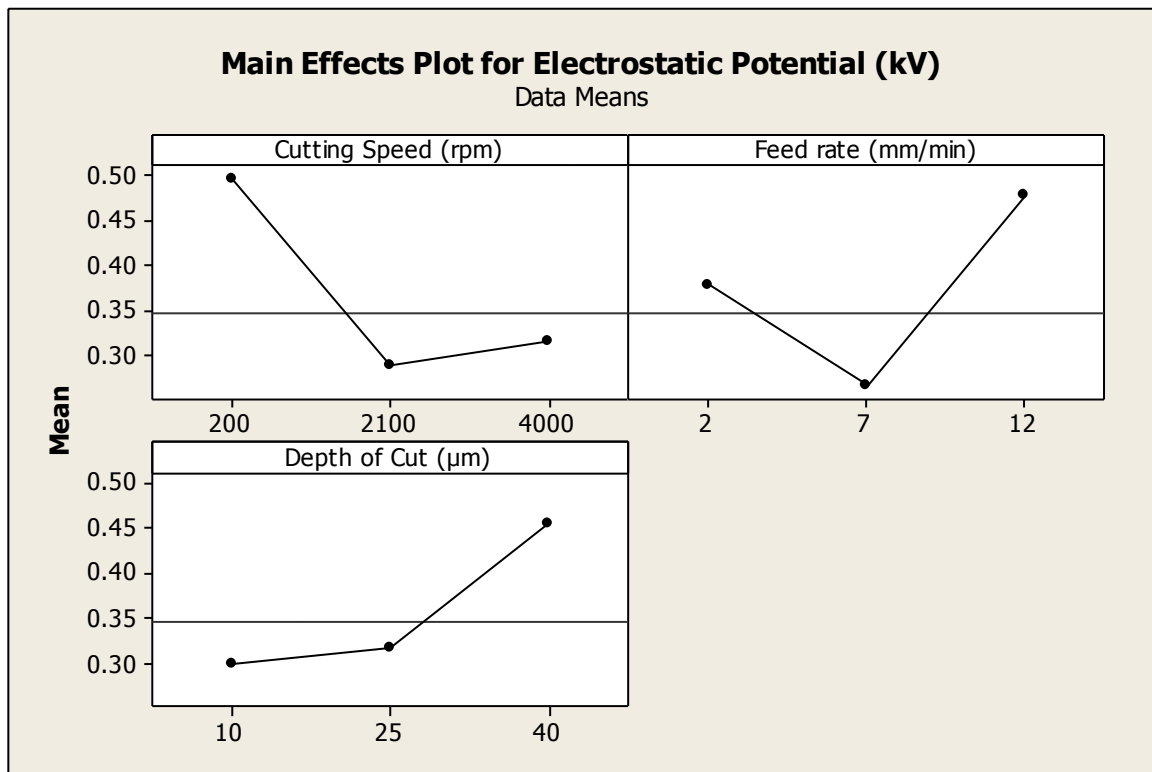
**Figure 82: ESD main effects plot for PMMA.**

The main effects plot for the cutting speed has a steep slope in the range from 200 – 2100 rpm, which shows a high correlation between speed and ESD. As the speed increases, the ESD decreases, indicating a negative relationship between the factors in that range. However, when the speed increases from 2100 – 4000 rpm, the ESD slightly increases, transitioning to a positive relationship.

When the feed rate increases from 2 – 7 mm/min, the ESD decreases sharply, showing a negative the feeds negative influence in that region on the ESD. When the feed increases from 7 – 12 mm/min, the ESD shoots up, as displayed by the steep incline. Indicating that the higher the feed rate, the higher the ESD generated. When the depth of cut increases from 10 – 25 $\mu$m, the ESD increases marginally, showing direct proportionality between the factors. When the depth increases from 25 – 40 $\mu$m the ESD increases greatly, showing that the depth of cut positively influences the ESD regardless of the range selected.

## 4.2.2.6 Interaction effects on the surface roughness

Figure 83 shows the interaction plot for the ESD generated. Analysing the cutting speed against the feed rate, as per the box 1, shows that keeping the speed constant at 200 rpm and varying the feed rate between 2 – 7 mm/min, shows a decline in the ESD generated. Increasing the feed rate from 7 – 12 mm/min shows a slight increase almost parallel to the x – axis, indicating that the ESD along the varying feed is almost the same.

Keeping the speed constant at 2100 rpm and varying the feed between 2 – 7 mm/min displays a decrease in the ESD, however, as soon as the feed is increased to reach 12 mm/min, the ESD greatly increases, as shown by the steep slope increase.

Keeping the speed constant at 4000 rpm and varying the feed between 2 – 7 mm/min shows a slight decrease in the ESD, almost as if the values are within the same level, but increasing the feed rate from 7 – 12 mm/min, drastically increases the ESD generated. Between the speed and feed, a low ESD is generated when the feed is between 2 – 7 mm/min, when it increases beyond 7 mm/min, for any cutting speed used, the ESD generated increases.
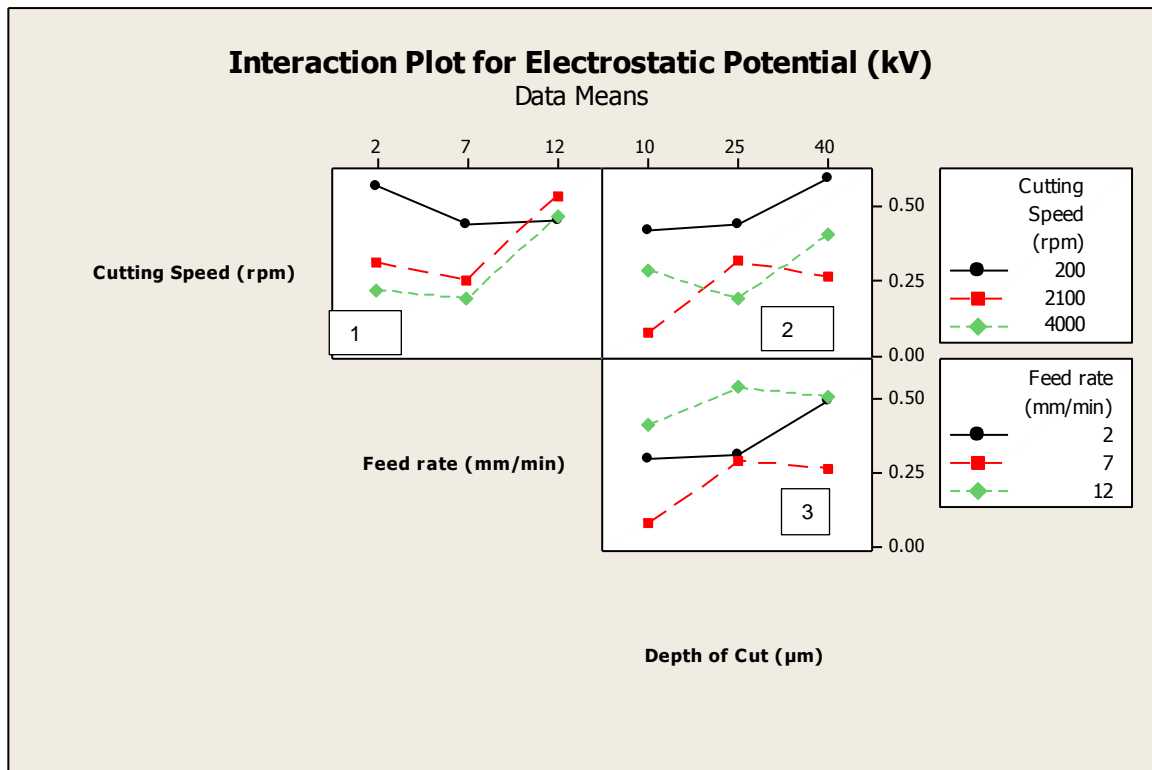
**Figure 83: ESD interaction plot for PMMA.**

Analysing the cutting speed versus the depth of cut, as per box 2, shows that keeping the speed constant at 200 rpm and varying the depth of cut between 10 – 25 μm, shows a slight increase in the ESD, however, very marginal because the line is almost parallel to the x – axis, indicating that values are within the same level. Increasing the depth of cut from 25 – 40 μm, shows a greater increase in the ESD, as displayed by the increased slope.

Keeping the speed constant at 2100 rpm and varying the depth between 10 – 25 μm shows an increase in the ESD indicated by the steep incline. A further increase in the depth of cut, however, creates a decrease in the ESD. Keeping the speed constant at 4000 rpm and varying the depth between 10 – 40 μm, shows an initial decrease in the ESD up to 25 μm, then an immediate increase in the ESD beyond increased 25 μm. Between the cutting speed and depth of cut, a low cutting speed of 200 rpm and any depth of cut generates ESD which gradually increases, however, at 2100 rpm the depth needs to be between 25 – 40 μm to generate low ESD, and when the speed is 4000 rpm, the depth must be between 10 – 25 μm for low ESD.

149

Analysing the relationship between the feed rate and the depth of cut, as per box 3, shows that keeping the feed rate constant at 2 mm/min and varying the depth between 10 -25 μm creates an increase in the ESD, which is followed by an immediate decrease when the depth increases further to reach 40 μm.

Keeping the feed rate constant at 7 mm/min and varying the depth between 10 – 40 μm, shows a slight increase in the ESD up to 25 μm, and a jump in the ESD increase beyond 25 μm. Overall, the ESD increases at that feed rate and whichever variable is used for the depth of cut. Keeping the feed rate constant at 12 mm/min, and varying the depth of cut between 10 – 25 μm shows a steep slope which indicates an increase in the ESD generated, increasing further the depth of cut from 25 – 40 μm shows a slight decrease in the ESD. Between the feed rate and the depth of cut, when the feed rate is 7 or 12 mm/min the depth of cut needs to be between 25 – 40 μm to generate low ESD. When the feed rate is 2 mm/min, the depth of cut needs to be between 10 – 25 μm to generate low ESD.

## 4.2.2.7 Contour plot

Figure 84 shows the contour plot for the electrostatic potential against the speed, feed and a depth of cut held at 25 μm.
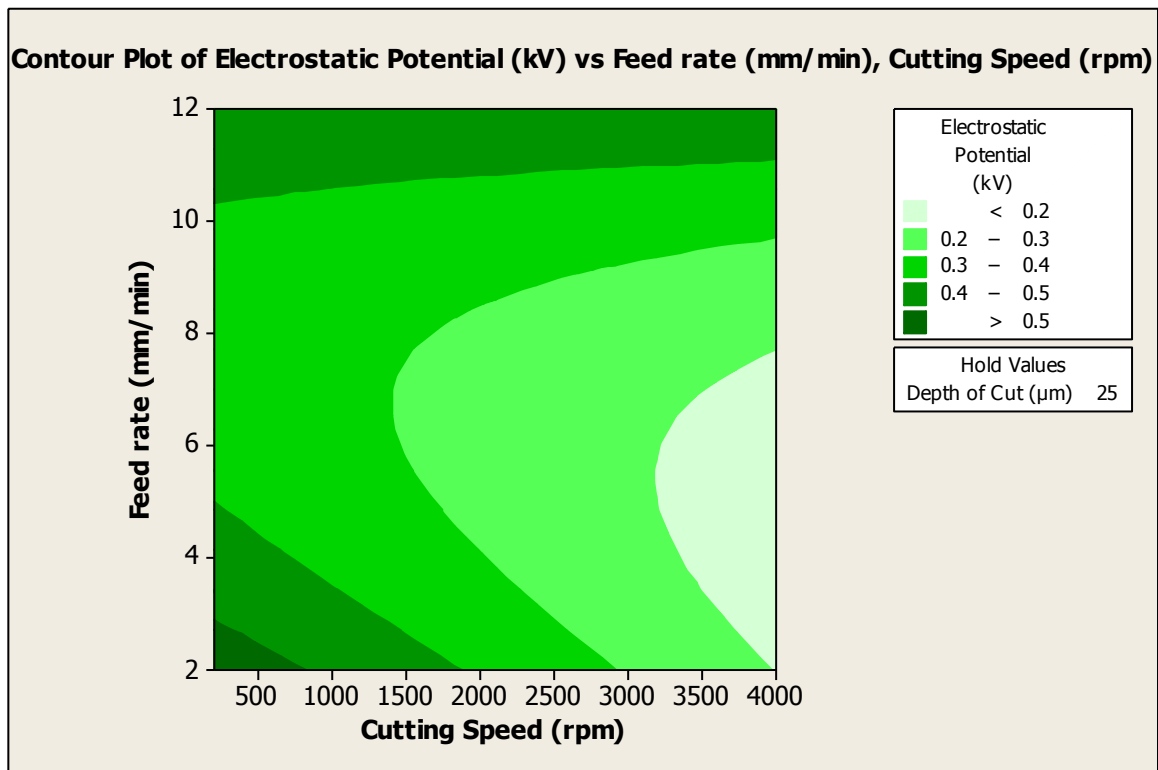
**Figure 84: ESD contour plot for PMMA.**

The contour plot shows that to reduce the ESD generated during single point diamond turning of PMMA (light green area), the cutting speed needs to be kept substantially high, at the maximum of 4000 rpm, with the feed rate variable between 2 – 7 mm/min. Keeping the cutting speed constant at 4000rpm and increasing the feed rate to 12 mm/min would greatly increase the ESD (dark green area), and that would be detrimental to the cutting operation. The contour plot also shows that the feed rate has a greater influence on the ESD and its effect is not linear.

## 4.2.2.8 Model summary

Table 43 below displays the model summary of regression with the error of regression 0.068, which slightly increased but is not too high of a gap between the least squares line and the observed values. The $R^2$ = 85.07 % which has dropped from the previous 91.90 %, but is still high to predict for new observations.

| S | $R^2$ | Adjusted $R^2$ | Predicted $R^2$ |
|---|---|---|---|
| 0.068 kV | 85.07 % | 79.74 % | 68.05 % |

Taking into account the sample size and the number of β coefficients in the model, the adjusted $R^2$ shows that 79.74 % of the variation in the ESD can be attributed to the variation in the cutting speed, feed rate and depth of cut during diamond machining of PMMA. The predicted $R^2$ = 68.05 % which is not higher than $R^2$ showing that the model does not over fit and it can predict for new observations not included in the calculations. The predictive power of the optimised model has greatly improved from the previous 45.84 %.

Table 44 below displays the original ESD measurements and the predicted ones from the obtained model. It can be concluded that modelling of ESD during single point diamond turning of PMMA is possible and has been done and analysed in this section. All the cutting parameters were found to influence the ESD generated. The charge generated varied between a minimum and a maximum positive in the same material based on the different cutting parameter combinations. High speed, low feed and medium depth generated the least ESD which is what is required during diamond turning to reduce tool failure as a subsequent of static discharge. The positive charge on the material indicates that PMMA gives off electrons leaving it positively charged.

Table 44: Predicted ESD for PMMA.

| Run Order | Cutting Speed (rpm) | Feed rate (mm/min) | Depth of Cut (µm) | Electrostatic discharge (kV) | Predicted Electrostatic discharge (kV) |
|---|---|---|---|---|---|
| 1 | 200 | 12 | 10 | 0.4133 | 0.3979 |
| 2 | 2100 | 7 | 25 | 0.2895 | 0.2670 |
| 3 | 4000 | 2 | 10 | 0.1575 | 0.1187 |
| 4 | 200 | 2 | 40 | 0.7075 | 0.6382 |

| 5 | 4000 | 12 | 40 | 0.5268 | 0.5574 |
| 6 | 2100 | 7 | 25 | 0.3537 | 0.2670 |
| 7 | 200 | 7 | 25 | 0.4393 | 0.3570 |
| 8 | 2100 | 7 | 25 | 0.3062 | 0.2670 |
| 9 | 2100 | 2 | 25 | 0.3109 | 0.3784 |
| 10 | 2100 | 7 | 10 | 0.0780 | 0.1885 |
| 11 | 2100 | 7 | 25 | 0.2064 | 0.2670 |
| 12 | 4000 | 7 | 25 | 0.1921 | 0.1769 |
| 13 | 2100 | 12 | 25 | 0.5391 | 0.4777 |
| 14 | 2100 | 7 | 40 | 0.2658 | 0.3454 |
| 15 | 4000 | 12 | 10 | 0.4172 | 0.4005 |
| 16 | 4000 | 2 | 40 | 0.2872 | 0.2755 |
| 17 | 2100 | 7 | 25 | 0.2371 | 0.2670 |
| 18 | 200 | 2 | 10 | 0.4290 | 0.4813 |
| 19 | 200 | 12 | 40 | 0.4919 | 0.5548 |
| 20 | 2100 | 7 | 25 | 0.3014 | 0.2670 |

## 4.3 Conclusion

Cutting speed, feed rate and depth of cut were selected during SPDT of ONSI-56 and PMMA. Various combinations were chosen to study their effects on the surface roughness and electrostatic discharge generated. Chapter 5 will conclude the results.

# CHAPTER 5: CONCLUSION AND RECOMMENDATION

**Table 45: Summary table between ONSI-56 and PMMA.**

| SURFACE ROUGHNESS RESULTS | |
|---|---|
| ONSI-56 | PMMA |
| $\widehat{SR_{ONSI-56}} = -23.5031 - 0.1713s$ $+ 63.9199f + 4.7795e^{-5}s^2$ $- 0.01746sf$ | $\widehat{SR_{PMMA}} = 38.05 - 0.0411s + 11.43f$ $+ 0.00001s^2 - 0.003sf$ |
| S = -23.5031 nm | S = 16.77 nm |
| $R^2$ = 94.94 % | $R^2$ = 90.87 % |
| Adjusted $R^2$ = 93.60 % Model does not over fit because this is not greater than $R^2$ | Adjusted $R^2$ = 88-43 % Model does not over fit because this is not greater than $R^2$ |
| Predicted $R^2$ = 90.59 % Higher predictive power. | Predicted $R^2$ = 78.15 % High predictive power. |
| Between 200 – 2100 rpm, there is a decline in the surface roughness from high to low. Between 2100 – 4000 rpm, the surface roughness is even lower. There is a negative relationship between the cutting speed and the surface roughness. Keeping the cutting speed constant at 200 rpm and varying the feed rate increases the surface roughness gradually. Keeping the cutting speed constant at 2100/4000 rpm and varying the feed rate produces a low surface roughness but there is no variability. | Between 200 – 2100 rpm, there is a decline in the surface roughness from high to low. Between 2100 – 4000 rpm, the surface roughness is even lower. There is a negative relationship between the cutting speed and the surface roughness. Keeping the cutting speed constant at 200 rpm and varying the feed rate increases the surface roughness gradually. Keeping the cutting speed constant at 2100 rpm and varying the feed rate increases and decreases the surface roughness. Keeping the cutting speed constant at |

| | 4000 rpm and varying the feed rate produces a low surface roughness but no variability. |
|---|---|
| Between 2 -12 mm/min, there is an increase in the surface roughness, from low to high.<br>There is a positive relationship between the feed rate and the surface roughness. | Between 2 -12 mm/min, there is an increase in the surface roughness, from low to high.<br>There is a positive relationship between the feed rate and the surface roughness. |
| Depth of cut has no influence. | Depth of cut has no influence. |
| The optimum operating parameters would be:<br>s: (600 – 3700) rpm<br>f: (2 – 7) mm/min | The optimum operating parameters would be:<br>s: (2300 – 3200) rpm<br>f: (2 – 7) mm/min |

The cutting speed and feed rate affects both materials.

They both showed that a minimum cutting speed with a high feed rate would produce poor surface finish.

To obtain optimal quality the cutting speed needs to be high and the feed rate needs to be low.

The models developed both have high predictive capabilities.

The nature of the contact lens material combined with the cutting conditions affects the surface roughness.

The model developed for PMMA could predict for surface roughness.

The model developed for ONSI-56 needs revision and better cutting parameters need to be selected, to cater for the negative surface roughness obtained during prediction.

| ELECTROSTATIC DISCHARGE | |
|---|---|
| $\widehat{V_{ONSI-56}} = -0.0219 - 2.479e^{-4}s$<br>$+ 0.1034f + 5.437e^{-8}s^2$<br>$- 2.1305e^{-5}sf$ | $\widehat{V_{PMMA}} = 0.6233 - 1.15e^{-4}s - 0.1005f$<br>$+ 0.0052d + 0.0064f^2$<br>$+ 9.61e^{-6}sf$ |
| S = 0.2045 kV | S = 0.068 kV |
| $R^2$ = 79.32 % | $R^2$ = 85.07 % |
| Adjusted $R^2$ = 73.81 %<br>Model does not over fit because this is | Adjusted $R^2$ = 79.74 %<br>Model does not over fit because this is |

| | |
|---|---|
| not greater than $R^2$ | not greater than $R^2$ |
| Predicted $R^2$ = 60.58 %<br><br>Predictive power is not too high. | Predicted $R^2$ = 68.05 %<br><br>Predictive power is higher than ONSI-56. |
| Between 200 – 4000 rpm, there is a decline in the ESD generated from high to low.<br><br>There is a negative relationship between the cutting speed and the ESD.<br><br>Keeping the cutting speed constant at 200 rpm and varying the feed rate decreases and increases the ESD generated.<br><br>Keeping the cutting speed constant at 2100 rpm and varying the feed rate increases the ESD.<br><br>Keeping the cutting speed constant at 4000 rpm and varying the feed rate decreases and increases the ESD. | Between 200 – 2100 rpm, there is a decline in the ESD generated from high to low.<br><br>Between 2100 – 4000 rpm, the ESD increases slightly.<br><br>Keeping the cutting speed constant at 200 or 2100 or 4000 rpm, and varying the feed rate decreases and increases the ESD generated.<br><br>Keeping the cutting speed constant at 200 rpm, and varying the depth of cut between 10 - 40µm, increases the ESD generated.<br><br>Keeping the cutting speed constant at 2100 rpm, and varying the depth of cut increases and decreases the ESD generated.<br><br>Keeping the cutting speed constant at 4000 rpm, and varying the depth of cut decreases and increases the ESD generated. |
| Between 2 -12 mm/min, there is an increase in the ESD, from low to high.<br><br>There is a positive relationship between the feed rate and the ESD generated. | Between 2 -7 mm/min, there is a decrease in the ESD, from high to low.<br><br>Between 7 – 12 mm/min, there is an increase in the ESD generated.<br><br>Keeping the feed rate constant at 2 mm/min, and varying the depth of cut between 10 - 40µm, increases and decreases the ESD generated.<br><br>Keeping the feed rate constant at 7 |

| | mm/min, and varying the depth of cut increases the ESD generated. Keeping the feed rate constant at 12 mm/min, and varying the depth of cut increases and decreases the ESD generated. |
|---|---|
| Depth of cut has no influence. | Between 10 -40 µm, there is an increase in the ESD, from low to high. There is a positive relationship between the depth of cut and the ESD generated. |
| The optimum operating parameters would be: s: (800 – 4000) rpm f: (2 – 7) mm/min | The optimum operating parameters would be: s: (3300 – 4000) rpm f: (2 – 7) mm/min d: 25 µm |

The cutting speed and feed rate affects both materials, and the depth of cut affected PMMA.

To obtain a minimum ESD during machining of PMMA, a high cutting speed, low feed and medium depth of cut needs to be utilised.

To obtain a minimum ESD during machining of ONSI-56, a high cutting speed and a low feed rate needs to be utilised.

The models developed both have good predictive capabilities.

The hydrophobic-based nature of ONSI-56 affected the generation of the ESD because the water content (however low) diminished the potentials generated.

The models developed for both materials could predict the ESD.

Recommendation

Further research is required on the impact of the material characteristics (chain structure and molecular weight), environmental conditions and the microscopic measurement of the cutting tool, during SPDT of contact lens polymers.

# BIBLIOGRAPHY

AMBROSIO, L. 1998. Polymers for Biomedical Applications. *Polymer International,* 46**,** 161 - 162.

AMERICAN CHEMISTRY COUNCIL, I. 2015. *The Basics: Polymer Definition and Properties* [Online]. Available: https://plastics.americanchemistry.com/EducationResources/Plastics101/TheBasicsPolymer DefinitionandProperties.html [Accessed 31, 03 2016].

AMETEK ULTRA PRECISION TECHNOLOGIES A versatile Automated System for Precision Optics Measurement.

BANGS LABORATORIES, I. 2015. Material Properties of Polystyrene and Poly(methyl methacrylate) (PMMA) Microspheres. Fishers, Indiana.

BAYTEKIN, H. T., BAYTEKIN, B., SOH, S. & GRZYBOWSKI, B. A. 2011. Is Water Necessary for Contact Electrification? *Angewandte Chemie International Edition,* 50**,** 6766-6770.

BENNETT, E. S., PERRIGIN, J. M., WATANABE, R. K. & BEGLEY, C. G. 2015. Preliminary Evaluation. *In:* BENNETT, E. S. & HENRY, V. A. (eds.) *Clinical Manual of Contact Lenses.* 4th ed. Philadelphia, Pennsylvania Wolters Kluwer: Lippincott Williams & Wilkins.

BERGIN, J. 2000. Contact Lens Polymers: A technical overview of the development, manufacturing, and future of contact lenses Buffalo, New York: Department of Chemical Engineering.

BHOGAL, G. K. 2012. *Requirement for and optimisation of premium intraocular lenses.* PhD, Aston University.

BLOCK, H. M. 1961. History and Development of Contact Lenses. *International Ophthalmology Clinics,* 1**,** 299 - 309.

BORAD, M. B. & SHRIKRISHNA, N. J. 2015. Integrated finite element method and response surface methodology-based modelling and simulation of single point diamond turning of silicon. *International Journal of Machining and Machinability of Materials,* 17**,** 330- 354.

BOX, G. E. P. & HUNTER, J. S. 1957. Multi-Factor Experimental Designs for Exploring Response Surfaces. *Ann. Math. Statist.,* 28**,** 45.

BOX, G. E. P. & WILSON, K. B. 1992. On the Experimental Attainment of Optimum Conditions. *In:* KOTZ, S. & JOHNSON, N. L. (eds.) *Breakthroughs in Statistics: Methodology and Distribution.* New York, NY: Springer New York.

BURGO, T. A. L., DUCATI, T. R. D., FRANCISCO, K. R., CLINCKSPOOR, K. J., GALEMBECK, F. & GALEMBECK, S. E. 2012. Triboelectricity: Macroscopic Charge Patterns Formed by Self-Arraying Ions on Polymer Surfaces. *Langmuir,* 28**,** 7407-7416.

CASSTEVENS, J. M. 1983. Diamond turning of steel in carbon-saturated atmospheres. *Precision Engineering* 5**,** 7.

CHAO, C. L., CHEN, C. C., CHANG, C. J., DONG, H., MA, K. J., HSU, W. Y., HUANG, K. C. & CHAO, C. W. 2008. Single-Point Diamond Turning of Plasma-Nitrided Stainless Steel. *Key Engineering Materials,* 364-366**,** 7.

CHON, K. S. & NAMBA, Y. 2010. Single-point diamond turning of electroless nickel for flat X-ray mirror. *Journal of Mechanical Science and Technology,* 24**,** 1603-1609.

CHON, K. S., NAMBA, Y. & YOON, K. H. 2008. Single-Point Diamond Turning of Aspheric Mirror with Inner Reflecting Surfaces. *Key Engineering Materials,* 364-366**,** 39-42.

CHONG, F. F., TO, S. & CHAN, K. C. 2012. Cutting Characteristics of Lanthanum Base Metallic Glass in Single Point Diamond Turning. *Key Engineering Materials,* 516**,** 651-655.

CHOUDHURY, I. A. & EL-BARADIE, M. A. 1997. Surface roughness prediction in the turning of high-strength steel by factorial design of experiments. *Journal of Materials Processing Technology* 67**,** 7.

CHRISTIE, C. & RAO, N. 2013. *Adhesion and Biofilms on Contact Lenses* [Online]. Microbe Wiki. Available:

https://microbewiki.kenyon.edu/index.php/Adhesion_and_Biofilms_on_Contact_Lenses [Accessed 31, 03 2016].

CLEMITSON, I. R. 2015. Introduction to Polyurethanes. *Castable Polyurethane Polymers.* 2 ed. Boca Raton, Florida: CRC Press Taylor and Francis Group.

CORP., B. H. F. A. E. 2016 *Arri Replacement Lens for 1K Fresnel* [Online]. Available: https://www.bhphotovideo.com/c/product/459778-REG/Arri_L4_79572_E_Replacement_Lens_for_Arri.html [Accessed 31, 03 2016].

DABNUN, M. A., M.S.J. HASHMI & EL-BARADIE, M. A. 2005. Surface roughness prediction model by design of experiments for turning machinable glass–ceramic (Macor). *Journal of Materials Processing Technology,* 164-165**,** 5.

DAVIES, M. A., EVANS, C. J., PATTERSON, S. R., VOHRA, R. & BERGNER, B. C. 2003. Application of precision diamond machining to the manufacture of micro-photonics components. *Proc. of SPIE,* 5183**,** 15.

EFRON, C. M.-C. N. 2003. Hydrogel Lenses – Materials and Manufacture: A Review. *Optometry in Practice,* 4**,** 16.

ENGDAHL, N. C. 2006. CVD Diamond Coated Rotating Tools for Composite Machining. SAE International.

EVANS, C. J. 2012. Precision engineering: an evolutionary perspective. *Phil. Trans. R. Soc. A,* 370 17.

FELIPE ZARAGOZI OPTICA. 2016. *Ophthalmic lenses* [Online]. Available: http://opticaenaltea.es/en/ophthalmic-lenses/ [Accessed 31, 03 2016].

FICKER, T., KAPIČKA, V., MACUR, J., SLAVÍČEK, P. & BENEŠOVSKÝ, P. 2005. Fractality of Electrostatic Microdischarges on the Surface of Polymers. *J. Phys. D: Appl. Phys.,* 44**,** 5.

FOLLOWS, G. W., LOWELL, J. & WILSON, M. P. W. 1991. Contact electrification of polyamides. *Journal of Electrostatics,* 26**,** 13.

FRIEDLE, S. & THOMAS, S. W. 2010. Controlling Contact Electrification with Photochromic Polymers. *Angewandte Chemie International Edition,* 49**,** 7968-7971.

GIRALDEZ, M. J. & PIMENTEL, E. Y. 2012. Hydrogel Contact Lenses Surface Roughness and Bacterial Adhesion. *Intech* 1**,** 26.

GOEL, B., SINGH, S. & SAREPAKA, R. V. 2016. Precision Deterministic Machining of Polymethyl Methacrylate by Single Point Diamond Turning. *Materials and Manufacturing Processes*.

GOEL, S., LUO, X. C., REUBEN, R. L., BIN RASHID, W. & SUN, J. N. 2011. Single Point Diamond Turning of Single Crystal Silicon Carbide: Molecular Dynamic Simulation Study. *Key Engineering Materials,* 496**,** 150-155.

GOODLAW, E. 2002. A Personal Perspective on the History of Contact Lenses. *Elsevier Science Inc.,* 27**,** 139 - 145.

GUBBELS, G. P. H. 2006. *Diamond turning of glassy polymers.* PhD, Eindhoven: Technische Universiteit Eindhoven.

GUBBELS, G. P. H., BEEK, G. J. F. T. V. D., HOEP, A. L., DELBRESSINE, F. L. M. & C, H. V. H. 2004. Diamond Tool Wear when Cutting Amorphous Polymers. *CIRP Annals - Manufacturing Technology* 53**,** 4.

HAN, S., ZHAO, J., CUI, Q., WANG, P., XING, T., LI, Y. & CUI, Z. Scatter analysis of diffractive surface manufactured by single point diamond turning. *In:* HAN, S., XING, T., LI, Y. & CUI, Z., eds. 3rd International Symposium on Advanced Optical Manufacturing and Testing Technologies: Design, Manufacturing, and Testing of Micro- and Nano-Optical Devices and Systems,, 8 July 2007 2007 Chengdu, China. Proc. of SPIE Vol. 6724, 67241N1 - 67241N5.

HEIMKE, G. 1989. Materials for Biomedical Applications—Bone and Joint Replacements. *Angewandte Chemie,* 28**,** 3.

HOCHENG, H. & HSIEH, M. L. 2004. Signal analysis of surface roughness in diamond turning of lens molds. *International Journal of Machine Tools & Manufacture,* 44**,** 12.

JAGTAP, K. & PAWADE, R. 2014. Experimental Investigation on the Influence of Cutting Parameters on Surface Quality obtained in SPDT of PMMA. *Int. J. Advanced Design and Manufacturing Technology,* 7**,** 6.

JAGTAP, K. A., PAWADE, R. S. & BALASUBRAMANIAM, R. 2012. Some Investigations on Surface characteristics in Precision Turning of Nylon and Polypropylene. *1st International Conference on Recent Trends in Engineering & Technology.* Tamilnadu, India: International Journal of electronics, Communication & Soft Computing Science & Engineering.

JI, S., YU, H., ZHAO, J., LIU, X. & HU, M. 2016. Analysis and comparison of two different ultra-precision manufacturing methods for off-axis parabolic mirror with single point diamond turning. *Proceedings of the Institution of Mechanical Engineers, Part B: Journal of Engineering Manufacture,* 230**,** 10.

KADERNANI, M. M. 2014. *Electrical-Static Discharge in Single Point Diamond Turning Machining of Contact Lns Polymers.* Masters, Nelson Mandela Metropolitan University.

KADIRGAMA, K., NOOR, M. M., RAHMAN, M. M., REJAB, M. R. M., HARON, C. H. C. & ABOU-EL-HOSSEIN, K. A. 2009. Surface Roughness Prediction Model of 6061-T6 Aluminium Alloy Machining Using Statistical Method. *European Journal of Scientific Research,* 25**,** 7.

KAILAS, S. V. 2013. Applications and Processing of Polymers. *Material Science.* India: Dept. of Mechanical Engineering, Indian Institute of Science.

KOBAYASHI, A. & HIRAKAWA, K. 1984. Ultraprecision  Machining of Plastics. Part 1. Polymethyl Methacrylate. *Polymer -Plastics Technology and Enginerering,* 22**,** 11.

LACE, R. 2013. *Intraocular Lenses and Their Potential to Prohibit Posterior Capsule Opacification.* PhD, University of Liverpool.

LAGADO CORPORATION. 2014. *Premium GP Materials* [Online]. Menicon America Inc. Available: https://www.lagadocorp.co/products/premium-gp-materials [Accessed 29, 07 2016].

LAI, Y. C. & FRIENDS, G. D. 1997. Surface wettability enhancement of silicone hydrogel lenses by processing with polar plastic molds. *J. Biomed. Mater. Res.,* 35**,** 8.

LASER COMPONENTS. 2016. *Optical Gratings* [Online]. Available: http://www.lasercomponents.com/uk/product/diffraction-grating/ [Accessed 31, 03 2016].

LEE, B. 2009. Triboelectric Table. AlphaLab, Inc.

LEVENE, J. R. 1967. Sources of Confusion in Descartes's Illustrations, with Reference to the History of Contact Lenses. *History of Science,* 6**,** 7.

LI, C. J., LI, Y., GAO, X. & DUONG, C. V. 2015. Ultra-precision machining of Fresnel lens mould by single-point diamond turning based on axis B rotation. *Int J Adv Manuf Technol,* 77**,** 6.

LI, S. & ZHANG, Y. 2016. Application of Single Point Diamond Turning in Infrared Optics. *International Symposium on Advances in Electrical, Electronics and Computer Engineering,* 1**,** 8.

LIU, L., OXENHAM, W. & SEYAM, A. M. 2013a. Contact electrification of polymeric surfaces. *Indian Journal Of Fibre and Textile Research,* 38**,** 5.

LIU, L., SEYAM, A. M. & OXENHAM, W. 2013b. Frictional Electrification on Polymeric Flat Surfaces. *Journal of Engineered Fibers and Fabrics,* 8**,** 11.

LUTTRELL, D. E. 2010. Innovations in Ultra-Precision Machine Tools: Design and Applications. Precision Engineering

MAST. *Scientific Principles: Polymers* [Online]. Available: http://matse1.matse.illinois.edu/polymers/prin.html [Accessed 14, 04 2016].

MASTERTECH DIAMOND PRODUCTS COMPANY. 2016. *PCD (Polycrystalline Diamond) Cutting Tools* [Online]. Available: http://www.mastertechdiamond.com/pcd-cutting-tools.html [Accessed 31, 03 2016].

MAZUMDERA, M. K., SIMSA, R. A., BIRISA, A. S., SRIRAMAA, P. K., SAINIA, D., YURTERIB, C. U., TRIGWELLC, S., DEA, S. & SHARMAA, R. 2006. Twenty-first century research needs in electrostatic processes applied to industry and medicine. *Chemical Engineering Science,* 61**,** 20.

MCCARTY, L. S. & WHITESIDES, G. M. 2008. Electrostatic Charging Due to Separation of Ions at Interfaces: Contact Electrification of Ionic Electrets. *Angewandte Chemie International Edition,* 47**,** 2188-2207.

MCKEEN, L. W. 2013. Plastics used in Medical Devices. *In:* MODJARRAD, K. & EBNESAJJAD, S. (eds.) *Handbook of Polymer Applications in Medicine and Medical Devices.* 1st ed. San Diego, Carlifonia: Elsevier.

MICKLES, C. V. & BENJAMIN, W. J. 2015. Optical Considerations in Contact Lens Practice. *In:* BENNETT, E. S. & HENRY, V. A. (eds.) *Clinical Manual of Contact Lenses.* 4th ed. Philadelphia, Pennsylvania Wolters Kluwer: Lippincott Williams & Wilkins.

MOHAMMADI, H., POYRAZ, H. B., RAVINDRA, D. & PATTEN, J. A. 2014. Single Point Diamond Turning of Silicon by Using Micro-Laser Assisted Machining Technique. *ASME 2014 International Manufacturing Science and Engineering Conference* 2**,** 1 - 8.

MOLINA, G. J. 2000. *Triboemission from Ceramics: Charge Intensity and Energy Distribution Characterisation.* PhD, Faculty of Virginia Polytechnic Institute and State University.

MONTGOMERY, D. C. 2013. *Design and Analysis of Experiments*, John Wiley & Sons, Inc.

MYSHKIN, N. K., PETROKOVETS, M. I. & KOVALEV, A. V. 2005. Tribology of polymers: Adhesion, friction, wear, and mass-transfer. *Tribology International,* 38**,** 12.

NAMBA, Y., SAEKI, M. & IKAWA, N. 2003. Optical Surface Generation of Organic Nonlinear Crystals by Single-Point Diamond Turning. *CIRP Annals - Manufacturing Technology,* 52**,** 475-478.

NAVE, C. R. 2006. *Common Vision Defects* [Online]. Georgia State University: HyperPhysics. Available: http://hydrogen.physik.uni-wuppertal.de/hyperphysics/hyperphysics/hbase/vision/eyedef.html [Accessed 05 July 2016].

NOVIN, A. 2015. *Surface Roughness* [Online]. Available: http://www.arknovin.com/en/qualitycontrol/surfacequality/surfaceroughness.html [Accessed 24, 05 2016].

OAKLAND DIAMOND TOOLS LLC. 2016. *Square Shaped Inserts* [Online]. Available: http://www.oaklanddiamondtools.com/inserts_square.php [Accessed 31, 03 2016].

OLUFAYO, O. A. & ABOU-EL-HOSSEIN, K. 2013. Preliminary investigation of surface finish of a contact lens polymer in ultra-high precision diamond turning. *2013 6th Robotics and Mechatronics Conference (RobMech).* Durban, South Africa: IEEE.

OLUFAYO, O. A., ABOU-EL-HOSSEIN, K. & KADERNANI, M. M. 2014. Tribo-electric Charging in the Ultra-high Precision Machining of Contact Lens Polymers. *Procedia Materials Science* 6**,** 8.

OOMEN, J. M. & EISSES, J. 1992. Wear of monocrystalline diamond tools during ultraprecision machining of nonferrous metals. *Precision Engineering* 14**,** 13.

ÖZEL, T. & KARPAT, Y. 2005. Predictive modeling of surface roughness and tool wear in hard turning using regression and neural networks. *International Journal of Machine Tools and Manufacture,* 45**,** 13.

PARAKKA, J., IYER, A., CHALASANI, D. & LI, L. 2013. Silicone-containing monomer. Google Patents.

PERSICO, J. 2016. Review of Cornea & Contact Lenses. Newtown Square, Pennsylvania: Professional Publications Division of Jobson Medical Information LLC (JMI).

POON, C. Y. & BHUSHAN, B. 1995. Comparison of surface roughness measurements by stylus profiler, AFM and non-contact optical profiler. *Wear,* 190**,** 13.

QUINN, M. H. & BASSETT, W. 2007. Beauty from Contact Lenses beyond Vision Correction. *American Chemical Society,* 1**,** 11.

RAVEENDRAN, P. & MARIMUTHU, P. 2016. Optimization of Machining Parameters for Minimizing Surface Roughness in Turning Operations of GFRP Rob Based on Response Surface Methodology. *International Journal of Advanced Engineering Technology,* 7**,** 4.

RHORER, R. L. & EVANS, C. J. 2010. Fabrication of Optics by Diamond Turning. *Handbook of Optics Handbook of Optics.* 3rd ed. Columbus, Ohio McGraw-Hill.

RIEMER, O. 2011. Advances in ultra precision manufacturing. *Proc. Jpn. Soc. Precis. Eng***,** 6.

RMILI, W., SERRA, R., OUAHABI, A., C.GONTIER & M.KIOUS 2006. Tool wear monitoring in turning process using vibration measurement. *13th International Congress on Sound and Vibration.* Vienna, Austria: Research Gate.

ROBINS, E. S., LOWELL, J. & ROSE-INNES, A. C. 1980. The role of surface ions in the contact electrification of insulators. *Journal of Electrostatics,* 8**,** 8.

ROGERS, K. & ROBLEE, J. Freeform Machining with Precitech Servo Tool Options. Precitech Ultra Precision Technology.

SAKAGUCHIA, M., M. MAKINOA, T. OHURAB & IWATAC, T. 2014. Contact electrification of polymers due to electron transfer among mechano anions, mechano cations and mechano radicals. *Journal of Electrostatics,* 72**,** 5.

SÁNCHEZ, F. A. V. & MUÑOZ, B. L. 2012. Evolución histórica de las lentes de contacto. *Archivos de la Sociedad Española de Oftalmología (English Edition),* 87**,** 265-266.

SCHIFRIN, L. G. & RICH, W. J. 1984. The Contact Lens Industry Structure, Competition, and Public Policy (Health Technology Case Study 31). Washington: DC: U.S. Congress, Office of Technology Assessment,.

SCHMITZ, A. 2012. *Polymers* [Online]. Available: http://2012books.lardbucket.org/books/beginning-chemistry/s20-06-polymers.html [Accessed 31, 03 2016].

SELINGER, R. L. B. 1997. History of Vision Correction- Contact and Intraocular Lenses *MRS Bulletin* 22**,** 65.

SIGMA-ALDRICH. 2016. *Polytetrafluoroethylene preparation* [Online]. Available: http://www.sigmaaldrich.com/catalog/product/aldrich/445096?lang=en&region=ZA [Accessed 31, 03 2016].

SINGH, K., VAISHYA, R. O., SINGH, H., MISHRA, V. & SAREPAKA, R. V. 2013. Investigation of Tool Life & Surface Roughness During Single Point Diamond Turning of Silicon. *IJSR - International Journal Of Scientific Research,* 2**,** 3.

SIVIGLIA, N. 2010. *A History of Contact Lenses* [Online]. Lancaster, Pennsylvania Edward Hand Medical Heritage Foundation. Available: http://edwardhandmedicalheritage.org/history_of_contact_lenses.html [Accessed 31,03 2016].

SMC CORPORATION Electrostatic Sensor Monitor.

SOH, S., KWOK, S. W., LIU, H. & WHITESIDES, G. M. 2012. Contact De-electrification of Electrostatically Charged Polymers. *Journal of the American Chemical Society,* 134**,** 20151-20159.

TANAKA, H., SHIMADA, S., HIGUCHI, M., YAMAGUCHI, T., KANEEDA, T. & OBATA, K. 2005. Mechanism of Cutting Edge Chipping and Its Suppression in Diamond Turning of Copper. *CIRP Annals - Manufacturing Technology,* 54**,** 51-54.

THE LAGADO CORPORATION 2004. ONSI-56 (onsifocon A) Rigid Gas Permeable Spherical, Aspheric, Toric and Bifocal Contact Lens for Daily Wear.

THE LAGADO CORPORATION. 2014. *Hard Lens Materials* [Online]. Menicon America Inc. Available: https://www.lagadocorp.co/products/hard-lens-materials [Accessed 29, 07 2016].

THOMAS, S. W., VELLA, S. J., KAUFMAN, G. K. & WHITESIDES, G. M. 2008. Patterns of Electrostatic Charge and Discharge in Contact Electrification. *Angewandte Chemie International Edition,* 47**,** 6654-6656.

THORNTON, A. G. & WILKS, J. 1980. The wear of diamond tools turning mild steel. *Wear,* 65**,** 67 - 74.

UNSW AUSTRALIA. 2013. *Polymerisation* [Online]. Faculty of Science, School of Materials Science and Engineering. Available: http://www.materials.unsw.edu.au/tutorials/online-tutorials/1-polymerisation [Accessed 31, 03 2016].

VENKATESH, V. C. & IZMAN, S. 2007. *Precision Engineering,* New Delhi, Tata McGraw-Hill Publishing Company Limited.

WIKIPEDIA. 2016. *Polymer* [Online]. Wikipedia. Available: https://en.wikipedia.org/wiki/Polymer [Accessed 31, 03 2016].

WILES, J. A., GRZYBOWSKI, B. A., WINKLEMAN, A. & WHITESIDES, G. M. 2003. A Tool for Studying Contact Electrification in Systems Comprising Metals and Insulating Polymers. *Analytical Chemistry,* 75**,** 9.

WINTERMANTEL, M., MAYER, E. & REICHERT, P. 2013. Low-viscosity reactive polyurethane compounds. Espacenet.

WS HAMPSHIRE INC. 2016. Polyethylene.

WYANT, J. C., KOLIOPOULOS, C. L., BHUSHAN, B. & BASILA, D. 1986. Development of a Three-Dimensional Noncontact Digital Optical Profiler. *Journal of Tribology,* 108**,** 8.

XU, H., ZHANG, X., XU, M. & LI, X. Study on the control of surface roughness in single point diamond turning. 2012. 84161D1-84161D7.

YANG, L., XU, H., ZHANG, X., XU, M., LI, X., RUCH, E. & LI, S. Study on the control of surface roughness in single point diamond turning. *In:* YANG, L., RUCH, E. & LI, S., eds. 6th International Symposium on Advanced Optical Manufacturing and Testing Technologies: Advanced Optical

Manufacturing Technologies, 26 April 2012 2012 Xiamen, China. Proceedings of SPIE, 84161D1 - 84161D7.

YINGFEI, G., JIUHUA, X. & HUI, Y. 2010. Diamond tools wear and their applicability when ultra-precision turning of SiCp/2009Al matrix composite. *Wear,* 269**,** 699-708.

ZHANG, S. J., TO, S. & ZHANG, G. Q. 2016. Diamond tool wear in ultra-precision machining. *Int J Adv Manuf Technol***,** 29.

ZHANG, Y. & SHAO, T. 2013a. Contact electrification between polymers and steel. *Journal of Electrostatics,* 71**,** 5.

ZHANG, Y. & SHAO, T. 2013b. A method of charge measurement for contact electrification. *Journal of Electrostatics,* 71**,** 5.

ZHANGA, S. J., TOB, S., WANGC, S. J. & ZHUB, Z. W. 2015. A review of surface roughness generation in ultra-precision machining. *International Journal of Machine Tools and Manufacture,* 91**,** 20.

ZHAO, Q., CHEN, J. & LUO, J. 2011. Analysis of the Swelling Effect in Single-Point Diamond Turning. *Advanced Materials Research,* 314-316**,** 984-987.

ZONG, W. J., LI, Z., SUN, T. & DONG, S. 2010. The basic issues in design and fabrication of diamond-cutting tools for ultra-precision and nanometric machining. *International Journal of Machine Tools and Manufacture* 50**,** 9.

# APPENDIX A: Triboelectric Table

| Column 1 (this col.): Insulator name. Col.2: Charge affinity in nC/J (nano ampsec/wattsec of friction). Col.3: Charge acquired if rubbed with metal (W=weak, N=normal, or consistent with the affinity). Col.4: Notes. | Affinity nC/J | Metal effect | **Triboelectric Table** Tests were performed by Bill Lee (Ph.D., physics). ©2009 by AlphaLab, Inc. (TriField.com), which also manufactured the test equipment used. This table may be reproduced only if reproduced in whole. |
|---|---|---|---|
| Polyurethane foam | +60 | +N | All materials are good insulators (>1000 T ohm cm) unless noted. |
| Sorbothane | +58 | -W | Slightly conductive. (120 G ohm cm). |
| Box sealing tape (BOPP) | +55 | +W | Non-sticky side. Becomes more negative if sanded down to the BOPP film. |
| Hair, oily skin | +45 | +N | Skin is conductive. Cannot be charged by metal rubbing. |
| Solid polyurethane, filled | +40 | +N | Slightly conductive. (8 T ohm cm). |
| Magnesium fluoride (MgF2) | +35 | +N | Anti-reflective optical coating. |
| Nylon, dry skin | +30 | +N | Skin is conductive. Cannot be charged by metal rubbing. |
| Machine oil | +29 | +N | |
| Nylatron (nylon filled with $MoS_2$) | +28 | +N | |
| Glass (soda) | +25 | +N | Slightly conductive. (Depends on humidity). |
| Paper (uncoated copy) | +10 | -W | Most papers & cardboard have similar affinity. Slightly conductive. |
| Wood (pine) | +7 | -W | |
| GE brand Silicone II (hardens in air) | +6 | +N | More positive than the other silicone chemistry (see below). |
| Cotton | +5 | +N | Slightly conductive. (Depends on humidity). |
| Nitrile rubber | +3 | -W | |
| Wool | 0 | -W | |
| Polycarbonate | -5 | -W | |
| ABS | -5 | -N | |
| Acrylic (polymethyl methacrylate) and adhesive side of clear carton-sealing and office tape | -10 | -N | Several clear tape adhesives are have an affinity almost identical to acrylic, even though various compositions are listed. |
| Epoxy (circuit board) | -32 | -N | |
| Styrene-butadiene rubber (SBR, Buna S) | -35 | -N | Sometimes inaccurately called "neoprene" (see below). |
| Solvent-based spray paints | -38 | -N | May vary. |
| PET (mylar) cloth | -40 | -W | |
| PET (mylar) solid | -40 | +W | |
| EVA rubber for gaskets, filled | -55 | -N | Slightly conductive. (10 T ohm cm). Filled rubber will usually conduct. |
| Gum rubber | -60 | -N | Barely conductive. (500 T ohm cm). |
| Hot melt glue | -62 | -N | |
| Polystyrene | -70 | -N | |
| Polyimide | -70 | -N | |
| Silicones (air harden & thermoset, but *not* GE) | -72 | -N | |
| Vinyl: flexible (clear tubing) | -75 | -N | |
| Carton-sealing tape (BOPP), sanded down | -85 | -N | Raw surface is very + (see above), but close to PP when sanded. |
| Olefins (alkenes): LDPE, HDPE, PP | -90 | -N | UHMWPE is below. Against metals, PP is more neg than PE. |

| | | | |
|---|---|---|---|
| Cellulose nitrate | -93 | -N | |
| Office tape backing (vinyl copolymer?) | -95 | -N | |
| UHMWPE | -95 | -N | |
| Neoprene (polychloroprene, *not* SBR) | -98 | -N | Slightly conductive if filled (1.5 T ohm cm). |
| PVC (rigid vinyl) | -100 | -N | |
| Latex (natural) rubber | -105 | -N | |
| Viton, filled | -117 | -N | Slightly conductive. (40 T ohm cm). |
| Epichlorohydrin rubber, filled | -118 | -N | Slightly conductive. (250 G ohm cm). |
| Santoprene rubber | -120 | -N | |
| Hypalon rubber, filled | -130 | -N | Slightly conductive. (30 T ohm cm). |
| Butyl rubber, filled | -135 | -N | Conductive. (900 M ohm cm). Test was done fast. |
| EDPM rubber, filled | -140 | -N | Slightly conductive. (40 T ohm cm). |
| Teflon | -190 | -N | Surface is fluorine atoms-- very electronegative. |

# APPENDIX B: Electrostatic Sensor Calibration

■Function selection mode

In measurement mode, press the [SET] button for 2 seconds or longer to display [F 0].
Show the display of function setting to be changed, [F□□].
Press the [SET] button for 2 seconds or longer in function selection mode to return to measurement mode.
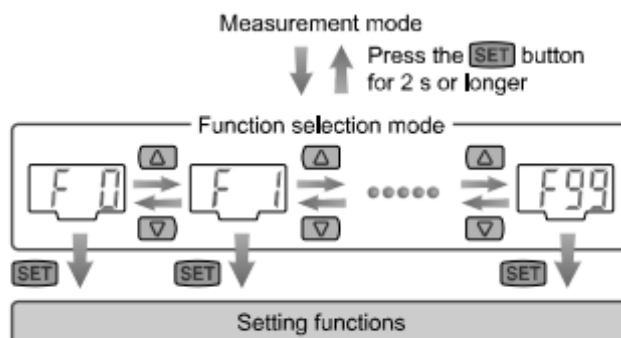


■Default setting

At the time of shipment, the following settings are provided.
If the setting is acceptable, keep it for use.

•NOTE
•When the default setting is changed, since the different setting item appears in order depending on how many times the [SET] button is pressed, confirm the item which needs to be set appears and prevent undesired setting.

Items below can be set at function selection mode.

| Item | | Default setting | Page |
|---|---|---|---|
| [F 0] Select connect sensor | | Sensor for 0.4 kV | See page 19 |
| [F 1] Operation of OUT1 [F 2] Operation of OUT2 | Output mode | Hysteresis mode | See page 20 |
| | Reversed output | Normal output | |
| | Charged potential setting | OUT1: +0.2 kV OUT2: -0.2 kV | |
| | Hysteresis | Hysteresis: 0.04 kV | |
| [F 1] Operation of OUT1 | Display color | ON: Green OFF: Red | See page 21 |
| [F 3] Measured distance setting | | 25 mm | See page 22 |
| [F 4] Setting of switch output response time | | 1 s | See page 23 |
| [F 5] Select analog output filter | | ON | See page 24 |
| [F 6] Setting of security code | | OFF | See page 25 |
| [F98] Setting of all functions | | OFF | See page 26 |
| [F99] Reset to the default setting | | OFF | See page 27 |

## ▪[F 0] Select connect sensor

Range of connected Electrostatic Sensor can be selected.
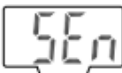
### <Operation>
Press the △ or ▽ button at function selection mode to display [F 0]

Press the SET button. ↓ Moves on to select connect sensor.

---

**Select connect sensor**

Press the △ or ▽ button to select sensor range.

Displays in turn

⌷5En⌷  ⟷  ⌷d0.4⌷

Sensor range            Set value

⌷d0.4⌷  △↗↘▽  ⌷d20⌷

±0.4 kV                ±20 kV

---

After selecting sensor range, press the △ and ▽ button together.

↓ Return to function selection mode.

( Setting of [F_0] connected sensor completed )

*: When connected Electrostatic Sensor range is changed, value corrected by switch output set value, peak value, bottom value and set distance zero adjust are returned to the state of shipment.

## ■[F 2] Operation of OUT2

Set output method of OUT2.
Display color depends on OUT1 output, and is not set with this function.

### <Operation>
Press the △ or ▽ button at function selection mode to display [F 2]

Press the SET button. ⬇ Moves on to select output mode.

Set based on [F 1] operation of OUT1 (page 20 to 21).

## ■[F 3] Measured distance setting

Input distance between charged object and the sensor.
Measurement distance or 0.4 kV sensor is settable within 10 to 50 mm, 20 kV sensor within 25 to 75 mm.
Distance can be changed by 1 mm.
∗: Upper/lower limit of measurement range depends on measured distance.
  Peak values and bottom values wire reset when measures distance is changed.



Charged potential [kV]
③ : 50 mm
② ─── : 25 mm
① - · - : 10 mm
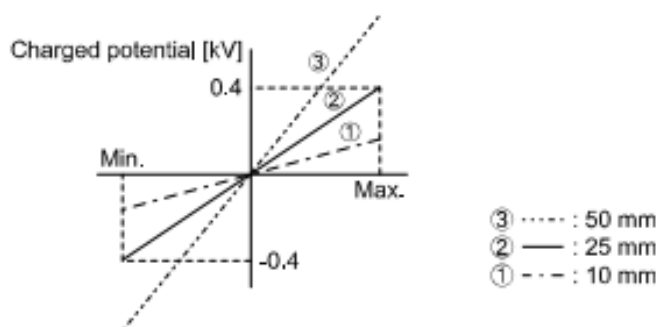
Drawing above shows 0.4 kV sensor.

### <Operation>
Press the △ or ▽ button at function selection mode to display [F 3]

Press the SET button. ⬇ Moves on to measured distance setting.

**Measured distance setting**

Press the △ or ▽ button to measured distance setting.
The △ button increases measured distance.
The ▽ button decreases measured distance.

Displays in turn
d i5 ⟷ 25
Distaqnce        Set value

Press the SET button to set. ⬇ Return to function selection mode.

Setting of [F 3] measured distance completed

168

## ■Operation of OUT1

Set output method of OUT1.
Output turns on when charged potential becomes larger the set value.
Display color depends on OUT1 output condition. When shipped out of factory, green lights when output is turned on. Red lights when output turned off.
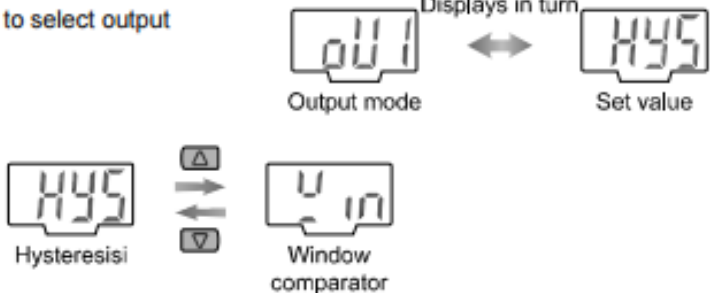
### <Operation>

Press the [△] or [▽] button at function selection mode to display [F 1]

Press the [SET] button. ⬇ Moves on to select output mode.

### Select output mode

Press the [△] or [▽] button to select output mode.

Displays in turn

[oU1] ⬌ [HYS]
Output mode          Set value

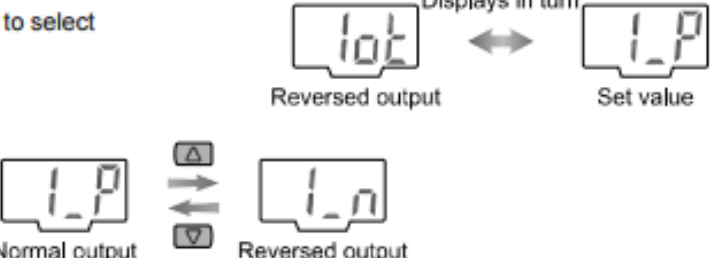[HYS] ⇄ [U in]
Hysteresisi          Window comparator

Press the [SET] button to set. ⬇ Moves on to select reversed output

### Select reversed output

Press the [△] or [▽] button to select reversed output.

Displays in turn

[Iot] ⬌ [I_P]
Reversed output          Set value

[I_P] ⇄ [I_n]
Normal output          Reversed output

Press the [SET] button to set. ⬇ Moves on to charged potential setting.

### Charged potential setting

Set charged potential based on setting procedure on page 14.
Hysteresis mode: [P_1]
Window comparator mode: [P1H]

Press the [SET] button to set. ⬇ Moves on to hysteresis change.

169